

Hybrid polymer solar cells

Citation for published version (APA):

Beek, W. J. E. (2005). *Hybrid polymer solar cells*. [Phd Thesis 1 (Research TU/e / Graduation TU/e), Chemical Engineering and Chemistry]. Technische Universiteit Eindhoven. <https://doi.org/10.6100/IR583197>

DOI:

[10.6100/IR583197](https://doi.org/10.6100/IR583197)

Document status and date:

Published: 01/01/2005

Document Version:

Publisher's PDF, also known as Version of Record (includes final page, issue and volume numbers)

Please check the document version of this publication:

- A submitted manuscript is the version of the article upon submission and before peer-review. There can be important differences between the submitted version and the official published version of record. People interested in the research are advised to contact the author for the final version of the publication, or visit the DOI to the publisher's website.
- The final author version and the galley proof are versions of the publication after peer review.
- The final published version features the final layout of the paper including the volume, issue and page numbers.

[Link to publication](#)

General rights

Copyright and moral rights for the publications made accessible in the public portal are retained by the authors and/or other copyright owners and it is a condition of accessing publications that users recognise and abide by the legal requirements associated with these rights.

- Users may download and print one copy of any publication from the public portal for the purpose of private study or research.
- You may not further distribute the material or use it for any profit-making activity or commercial gain
- You may freely distribute the URL identifying the publication in the public portal.

If the publication is distributed under the terms of Article 25fa of the Dutch Copyright Act, indicated by the "Taverne" license above, please follow below link for the End User Agreement:

www.tue.nl/taverne

Take down policy

If you believe that this document breaches copyright please contact us at:

openaccess@tue.nl

providing details and we will investigate your claim.

Hybrid Polymer Solar Cells

Hybrid Polymer Solar Cells

PROEFSCHRIFT

ter verkrijging van de graad van doctor aan de Technische Universiteit Eindhoven, op gezag van de Rector Magnificus, prof.dr. R.A. van Santen, voor een commissie aangewezen door het College voor Promoties in het openbaar te verdedigen op maandag 24 januari 2005 om 16.00 uur

door

Waldo Joseph Elisabeth Beek

geboren te Roermond

Dit proefschrift is goedgekeurd door de promotoren:

prof.dr.ir R.A.J. Janssen

en

prof.dr. M.D. McGehee

This research has been financially supported by the Council for the Chemical Sciences of the Netherlands Organization for Scientific Research (CW-NWO).

Omslagontwerp: Jan-Willem Luiten

Druk: universiteitsdrukkerij, TU/e

CIP-DATA LIBRARY TECHNISCHE UNIVERSITEIT EINDHOVEN

Beek, Waldo J.E.

Hybrid polymer solar cells / door Waldo J.E. Beek. – Eindhoven :

Technische Universiteit Eindhoven, 2005.

Proefschrift. - ISBN 90-386-2796-3

NUR 913

Subject headings: solar cells / conducting polymers / photoinduced electron transfer / polymer morphology; composites / hybrid organic-inorganic materials / nanoparticles; metal oxides / zinc oxide

Trefwoorden: zonnecellen / geleidende polymeren / fotogeïnduceerde elektronenoverdracht / composietpolymeren; morfologie / organische – anorganische hybride materialen / nanodeeltjes; metaaloxiden / zinkoxide

Table of Contents

Chapter 1 Introduction

1.1	Hybrid materials	2
1.2	Solar cells	3
1.2.1	Solar cell efficiencies	4
1.2.2	Silicon solar cells	4
1.2.3	Polymer solar cells	6
1.2.4	Dye-sensitized solar cells	8
1.2.5	Hybrid polymer solar cells	10
1.3	Objective and outline of this thesis	14
	References and notes	16

Chapter 2 Heterosupramolecular chemistry:

Heterosupramolecules from organic π -conjugated systems and TiO₂ nanoparticles as model compounds for electron transfer studies

2.1	Introduction to heterosupramolecular chemistry	22
2.2	TiO ₂ nanoparticle synthesis and characterization	23
2.2.1	TiO ₂ nanoparticle preparation	23
2.2.2	Compositional analysis	23
2.2.3	Size analysis	25
2.3	Electron transfer in heterosupramolecular assemblies	26
2.3.1	Formation of heterosupramolecular assemblies	26
2.3.2	Static photoluminescence quenching by photoinduced electron transfer	28
2.3.3	Structure of the oligomer used in a heterosupramolecule	30
2.4	Spacer length dependence of photoinduced electron transfer in heterosupramolecules	30
2.4.1	Distance dependence of charge transfer rate constants in the nonadiabatic weak-coupling regime	30
2.4.2	Heterosupramolecular assemblies with carboxylic acid linkers	31
2.4.3	Heterosupramolecular assemblies with phosphonic acid linkers	32
2.5	Conclusions	36
2.6	Experimental	36
	References and notes	41

Chapter 3 ZnO nanoparticles for application in bulk heterojunction solar cells

3.1	Introduction	44
3.2	Synthesis of soluble non-surfactant coated ZnO nanoparticles	47
3.3	Characterization of ZnO nanoparticles and rods	48
3.3.1	Size and composition analysis of ZnO nanoparticles	48
3.3.2	Photo-physical characterization of ZnO nanoparticles.....	51
3.3.3	Cyclic voltammetry and current-voltage measurements	53
3.4	Conclusions	55
3.5	Experimental	55
	References and notes.....	58

Chapter 4 Photovoltaic devices from zinc oxide nanoparticles and conjugated polymers

4.1	Introduction	62
4.2	Characterization of the solar cell performance.....	64
4.3	Observation of a photovoltaic effect in bulk heterojunction solar cells from ZnO nanoparticles and MDMO-PPV.....	66
4.4	Initial screening of relevant parameters.....	66
4.5	Effect of the layer thickness and vol.-% ZnO on the photovoltaic performance.....	68
4.6	Incident light power dependency measurements	70
4.7	Calculation of the AM1.5 performance of the optimized solar cell.....	72
4.8	Investigation of surfactant effects and application of ZnO nanorods	75
4.9	Degradation of the <i>nc</i> -ZnO:MDMO-PPV solar cell performance by UV illumination.....	77
4.10	Application of regio-regular poly(3-hexylthiophene) in hybrid solar cells.	78
4.11	Charge carrier transport in <i>nc</i> -ZnO:MDMO-PPV blends.....	80
4.12	Conclusions	82
4.13	Experimental	82
	References and notes.....	85

Chapter 5 Characterization of *nc*-ZnO:conjugated polymer bulk heterojunctions

5.1	Introduction	88
5.2	Photo-physical characterization of <i>nc</i> -ZnO:conjugated polymer composites	89
5.2.1	UV-vis absorption spectroscopy	89
5.2.2	Photoluminescence spectroscopy	90
5.2.3	Photoinduced absorption spectroscopy	93
5.2.4	Flash photolysis time-resolved microwave conductivity	95
5.3	Morphology studies on <i>nc</i> -ZnO:MDMO-PPV composites	97
5.3.1	Transmission electron microscopy	98
5.3.2	Tapping-mode atomic force microscopy	99
5.4	Conclusions	104
5.5	Experimental	106
	References and notes	108

Chapter 6 Hybrid ZnO:polymer bulk heterojunction solar cells from a ZnO precursor

6.1	Introduction	112
6.2	Sol-gel chemistry using ZnO precursors	112
6.3	Conversion of the precursor into crystalline ZnO	113
6.4	ZnO precursor:MDMO-PPV blends	114
6.4.1	Effect of annealing on the film thickness of <i>prec</i> -ZnO:MDMO-PPV blends	115
6.4.2	Effect of precursor condensation on the optical properties of <i>prec</i> -ZnO:MDMO-PPV blends	116
6.5	Photovoltaic effect in devices made from ZnO precursors and MDMO-PPV	119
6.5.1	Characterization of the photovoltaic effect	119
6.5.2	Effect of the processing parameters on the photovoltaic performance	120
6.6	Characterization of the morphology of <i>prec</i> -ZnO:MDMO-PPV blends	121
6.7	Conclusions	124
6.8	Experimental	125
	References and notes	127

Samenvatting**Summary****Curriculum Vitae****List of Publications****Dankwoord**

Chapter 1

Introduction

Abstract

This chapter introduces the concept and application of hybrid materials. Different strategies towards hybrid materials are reviewed and discussed with respect to application in solar energy conversion devices. Using present knowledge from polymer bulk heterojunction and dye-sensitized solar cells, the design of a simple, and in essence low cost, hybrid solar cell based on metal oxides and conjugated polymers is presented.

1.1 Hybrid materials

The words 'hybrid materials' stand for a combination of (a minimum of) two materials of a different nature into a new one having the combined properties of the starting materials together with some added value. The hybrid materials' properties are often superior to the sum of the intrinsic properties of the components and often have a functionality that is not present in either of the individual materials¹. In a historical perspective, the utilization of hybrid materials goes far back. A nice example is 'adobe', being a mixture of clay and straw, used in bricks and walls for buildings in rural areas. Its modern equivalent would be steel reinforced concrete, one of the building blocks of our modern society.

In recent years an increasing amount of scientific publications concerning hybrid organic – inorganic materials can be noticed (figure 1.1). The search for these materials is driven by the desire for combining the properties of inorganic materials and organic (polymeric) materials, to create new, enhanced, and appealing performance. Early applications of hybrid organic-inorganic systems can be found in paints, UV shields², and scratch resistant automotive coatings³. Hybrid material science has been used to improve optical^{4,5}, thermal, and mechanical⁶ properties of polymers. More recently the attention is drawn towards the electrical⁷ properties of hybrid organic-inorganic materials.

The discovery of conducting polymers by Alan MacDiarmid, Hideki Shirakawa, and Alan Heeger in 1977, and the ability to dope these polymers to cover the full range from insulator to metal⁸, has created a new field of research at the crossroads of chemistry and condensed matter physics. These newly discovered conjugated polymers with conducting and semiconducting properties provide exciting, promising opportunities for application in electronic devices. Semiconducting polymers offer the promise of achieving a new generation of materials, exhibiting the electrical and optical properties of metals or semiconductors and retaining the attractive mechanical properties and processing advantages of polymers. Many of the envisioned applications of conjugated polymers require transport of charges and therefore high charge carrier mobility. Hole mobilities in highly ordered regioregular polythiophenes⁹ and electron mobilities in ladder type polymers¹⁰ as high as 0.1

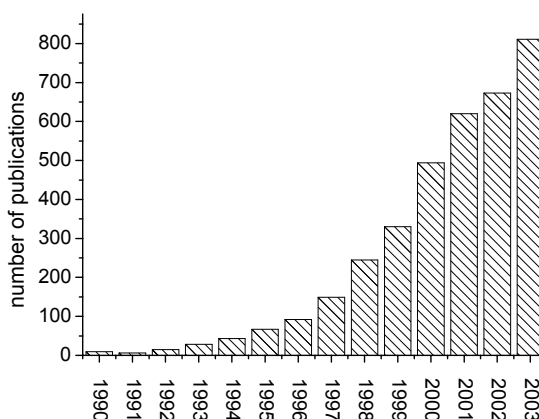


Figure 1.1 Histogram taken from the Chemical Abstracts displaying the number of publications using the term: 'Hybrid Organic Inorganic Materials'.

$\text{cm}^2 \text{V}^{-1} \text{s}^{-1}$ have been obtained. In general, the family of n-type conjugated polymers is much less developed than that of p-type conjugated polymers. In fact, the electron mobility of most conjugated polymers is still low compared to the hole mobility in p-type conjugated polymers and the electron mobility in inorganic systems. Increasing attention is given to hybrid conjugated polymer - inorganic materials, that represent a synergic approach to overcome the limitations of semiconducting polymer devices without losing their beneficial processability properties. New insights teach us that these materials might strengthen and enhance their intrinsic properties and will eventually lead to a yet newer class of exciting materials with a wide span of applications.

The combination of inorganic materials and conjugated polymers is now widely studied for various electronic applications^{1,7,11}, these studies confirm the high expectations risen. Some examples of the applications of polymers and inorganic materials include: photovoltaic devices^{12,13,14}, light-emitting diodes (LEDs)^{15,16,17,18}, solid state lasers¹⁹, sensors^{20,21}, memories²², batteries²³ and capacitors²⁴. In photovoltaic devices the inorganic material is added to overcome the limitations of the poor electron transport properties of the polymeric materials. In solar cells and LEDs the quantum confinement effect of semiconducting nanoparticles is used to tune the light absorption and electro-luminescence emission color of the hybrid material. LEDs based on inorganic nanoparticles as phosphors already find commercial application²⁵. In sensors, carbon black (CB) particles are used as filler in insulating²¹ or conducting²⁰ matrixes. An increased sensitivity is achieved when CB is combined with conducting polymers like polyaniline. In capacitors the problem related to the application of conducting polymers is a relatively low capacity to store charges. This is overcome by the addition of polyoxometalates²⁶ to conducting polymers like polyaniline or polypyrrole, showing an enhanced energy storage capability in the hybrid system.

1.2 Solar cells

This thesis covers the subject of hybrid polymer solar cells, and explores the use of inorganic-conjugated polymer hybrid materials. An attempt is made to bridge the gap between current silicon based fully inorganic solar cells and the polymeric/organic solar cells that are extensively studied. This chapter briefly introduces several types of solar cells covering silicon, polymer/organic based, and hybrid types like the dye-sensitized solar cell developed in the early 90ties. Current and promising strategies towards hybrid polymer solar cells are discussed and a strategy towards hybrid polymer solar cells as used in this thesis is outlined.

1.2.1 Solar cell efficiencies²⁷

Before discussing and comparing polymer solar cells it is important to briefly outline the various efficiencies that are used to characterize solar cells. Solar energy conversion efficiencies reported in literature are in general difficult to compare, because measurements are often performed using a variety of light sources that differ from the true solar emission spectrum. Besides this, there is a discrepancy between the absorption spectra of the material under investigation and that of the reference cell, mostly a silicon diode with a calibrated spectral response²⁸. The only pure and correct way is to measure the cells under a solar simulator that closely resembles the solar emission spectrum and intensity (the so-called standard AM1.5G emission), and to correct for the spectral mismatches between the reference cell, the device under observation, the emission spectrum of the simulator and the AM1.5 spectrum. When this is done, the efficiency can be referred to as a *measured* AM1.5 solar energy conversion efficiency.

A close approximation is measuring the J - V characteristic under a white-light source, with intensities close to the 100 mW cm^{-2} that is standardized for the AM1.5 emission. This allows an approximation of the open-circuit voltage²⁹ and fill factor³⁰ of the device under AM1.5 illumination. The current under the AM1.5 conditions is measured from the monochromatic incident photon to current efficiencies (IPCE), often referred to as external quantum efficiencies (EQE). Integration of the AM1.5 emission spectrum with the IPCE data gives the estimated short-circuit current density under AM1.5 illumination. Combined with the measured fill factor and open circuit voltage, this gives an *estimated* AM1.5 solar energy conversion efficiency. Efficiencies reported in literature for different solar cells have been collected in the next sections. The actual method used for determining the efficiencies is indicated, allowing a proper comparison. Where neither estimation nor measurements have been performed the maximum EQE has been used for comparison.

1.2.2 Silicon solar cells

Edmond Becquerel discovered the photovoltaic effect in 1838, when he observed a small voltage and current when two silver halide coated platinum plates immersed in an acidic solution were exposed to light. Only far in the next century a major improvement was achieved: Exactly 50 years ago, the first silicon solar cell was developed by Chapin, Fuller, and Pearson of Bell Telephone Laboratories³¹.

Silicon solar cells consist of p- and n-type silicon. In-between these two layers there is a transition layer, a p-n junction. The internal field over this junction separates the photogenerated charges, the holes are swept into the p-layer and the electrons are swept into the n-layer. Although these opposite charges attract each other, most of them can only recombine by passing through an external circuit outside the material because of the internal potential energy barrier. A scheme of a simple silicon solar cell is shown in figure 1.2

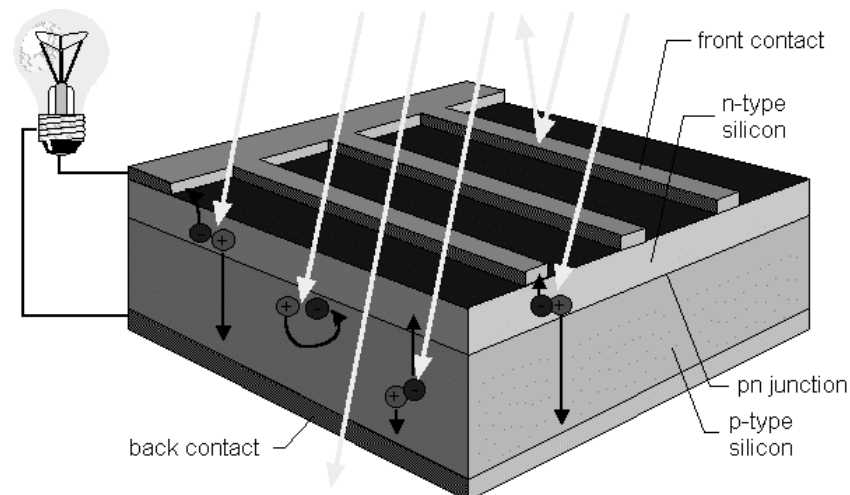


Figure 1.2 A simple scheme of a silicon solar cell, showing the basic elements: p- and n-type silicon and the junction in-between³².

Many different designs of this general p-i-n type silicon solar cell have been developed. Single crystalline and multi-crystalline cells nowadays reach 15-20% measured solar energy conversion efficiencies³³. In essence silicon is not the optimal material for solar cells, its bandgap of 1.1 eV (crystalline Si) is at the lower limit for optimal solar light harvesting. The requirements for an ideal solar cell³³ are:

1. Bandgap between 1.1 and 1.7 eV
2. Direct band structure
3. Non-toxic readily available materials
4. Easy reproducible deposition technique, suitable for large area
5. Good photovoltaic conversion efficiency
6. Long term stability

Silicon also suffers from its disadvantage of being an indirect semiconductor; as a result it is only a weakly absorbing material. For a silicon film to absorb 90% of the light, at least a 100 μm thick film is needed. Using direct semiconductors, like GaAs, a 1 μm thin film is sufficient. Because the photocarriers have to reach the p-n junction for separation, the silicon has to be of very high purity and crystalline perfection. For this reason the production of crystalline silicon is far from easy and cheap, and much attention is paid to the development of multi-crystalline and amorphous silicon solar cells, promising high efficiencies at lower costs. Nonetheless single crystalline silicon solar cells still have a market share of 43%, versus 48% for multi-crystalline silicon and only 8% for amorphous silicon³⁴, leaving 1% for non-silicon based solar devices.

1.2.3 Polymer solar cells

Semiconducting conjugated polymers^{35,36} offer an interesting alternative to silicon. In contrast to silicon, a 100-200 nm thin film of MDMO-PPV (poly[2-methoxy-5-(3',7'-dimethyloctyloxy)-1,4-phenylenevinylene], figure 1.4) absorbs almost 100% of light at its maximum absorption wavelength. One drawback of MDMO-PPV is its rather large bandgap of 2.5 eV³⁷ being far from optimal for solar energy conversion.

In contrast to inorganic semiconductors, photoexcitation of organic semiconductors generally results in a strongly bound electron-hole pair, called an exciton^{38,39}. In organic semiconductors these excitons are only effectively separated at an interface between a *p*-type (electron donating) and *n*-type (electron accepting) material. In general, the exciton lifetime and diffusion length in organic semiconductors are limited by radiative and non-radiative decay. As a consequence only excitons generated in close vicinity of a p-n interface will give rise to charges. For PPVs the exciton diffusion length ranges from 5-20 nm^{40,41,42}, this implies that for an effective charge separation the photogeneration of excitons should occur within approximately 10 nm from a p-n junction. For polythiophenes the exciton diffusion length is even less, approximately 5 nm⁴³. These short exciton diffusion lengths complicate the use of polymers in solar cells. Bilayer type polymer solar cells (see figure 1.3a) are limited by a small photogeneration of charges, because only a very thin layer near the junction is effective in charge carrier generation. In bulk heterojunction devices (figure 1.3b) the problem of the short exciton diffusion length in polymeric systems, is circumvented by intimately mixing the p- and n-type materials, creating junctions throughout the bulk of the material and ensuring quantitative charge generation from photogenerated excitons. In non-polymeric (small molecule) organic crystalline materials the exciton diffusion lengths can be quite large, e.g. ~70 nm in Cu-phthalocyanine (CuPc)⁴⁴, and up to a few micrometers in perylene bisimide films^{45,46}. Bilayer type photovoltaic devices made from CuPc and 3,4,9,10-perylenetetracarboxylic bisbenzimidazole (PTCBI) show a profound photovoltaic effect with a measured AM1.5 efficiency of 1%⁴⁷. The performance of these bilayer organic solar cells has further increased in recent years to 2%, for a PTCBI/C₆₀ bilayer device⁴⁸ and even to 4% for a device using layers of CuPc and C₆₀⁴⁹. Bulk heterojunction devices made from these small organic molecules using blends of CuPc:PTCBI⁵⁰, ZnPc:C₆₀⁴⁸, and CuPc:C₆₀⁵¹ respectively give measured AM1.5 efficiencies of 1.4%, 1.8% and 3.5%. One drawback of the use of small organic molecules in solar cells is their deposition, which requires high vacuum techniques at elevated temperatures. This makes this method not very suitable for large area production of photovoltaic devices. In contrast, simple spin casting of polymers from solution allows low-cost production on large areas.

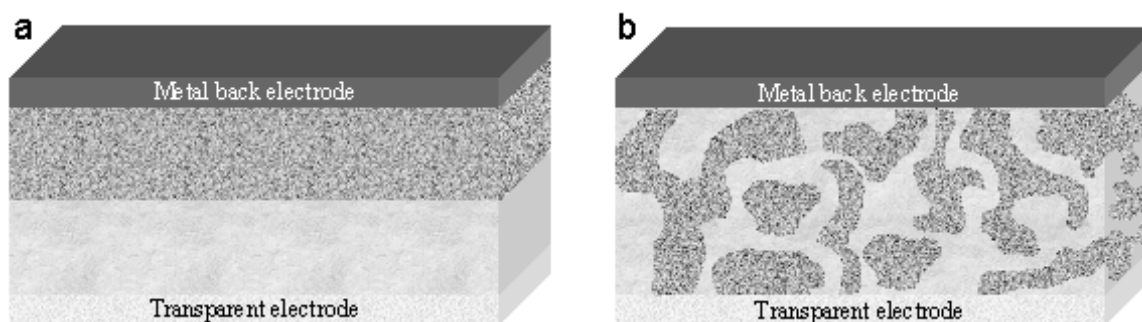


Figure 1.3 Schematic view of a) heterojunction (bilayer) device and b) a bulk heterojunction device.

Bulk heterojunction devices can be made from MDMO-PPV and 1-(3-methoxycarbonyl)propyl-1-phenyl-[6,6]-methanofullerene (PCBM)⁵². Blending of this fullerene derivative with the polymer should be precisely tailored to enable optimum conditions for effective charge separation and consecutive charge transport to opposite electrodes. Recent work on these MDMO-PPV:PCBM blends^{53,54}, shows the optimal morphology is as shown in figure 1.4, PCBM rich domains appear to be embedded in a polymer rich matrix. The blend is phase separated at a scale suitable for effective charge separation and the PCBM and MDMO-PPV rich phases allow an effective charge transport towards the electrodes with measured power-conversion efficiencies as high as 2.5%^{28,55}. Replacing the C₆₀ fullerene with a C₇₀ fullerene further improves device performance; measured AM1.5 efficiencies of 3% have been obtained⁵⁶.

Bulk heterojunction polymer solar cells have further been improved by the application of regioregular poly-alkylthiophenes in conjugated polymer/PCBM mixtures⁵⁷ and currently reach measured AM1.5 solar energy conversion efficiencies of 4%⁵⁸. These improvements are mainly due to higher hole mobilities in polythiophenes (FET mobilities up to 0.1 cm² V⁻¹ s⁻¹ have been observed)⁹ compared to MDMO-PPV (1

× 10⁻³ cm² V⁻¹ s⁻¹)⁵⁹. The mobility of the hole in MDMO-PPV however increases significantly in blends with PCBM⁶⁰. An additional advantage is an improved light harvesting by polythiophenes, these show a red-shifted absorption compared to MDMO-PPV, *i.e.* have a smaller effective bandgap. Konarka Technologies is currently exploring the market opportunities for these polymer bulk heterojunction solar cells^{58,61}. It is considered that with the promises of substantial cost reduction and

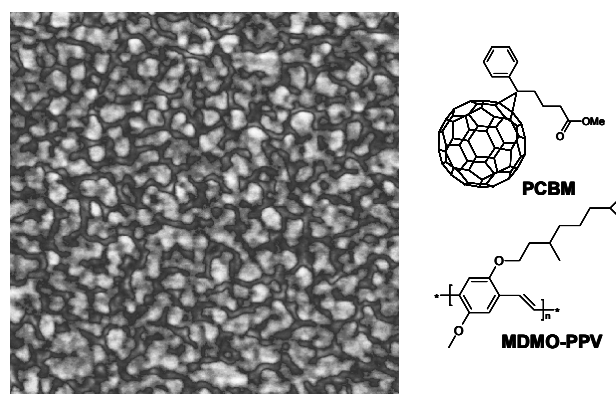


Figure 1.4 TM-AFM phase image of a PCBM:MDMO-PPV blend, image size is 2 by 2 micrometer.

a simple solution process suitable for large areas, even relatively low efficiencies of 5% will lead to market opportunities for organic polymer solar cells.

Other polymer solar cells so far only reach moderate efficiencies, polymer-only based solar cells consisting of MDMO-PPV as electron donor and PCNEPV⁶² as electron acceptor reach 0.75% measured under AM1.5 conditions⁶³. The combination of M3EH-PPV⁶⁴ as donor and PCNEPV as acceptor gives an estimated efficiency of 1%⁶⁵. These solar cells suffer from a low electron mobility in the n-type polymer.

1.2.4 Dye-sensitized solar cells

In 1991 Brian O'Regan and Michael Grätzel introduced the dye-sensitized solar cell (DSSC)⁶⁶. This type of solar cell is considered as a cost-effective alternative for silicon solar cells. The heart of the DSSC is a high surface area TiO₂ nanoparticulate electrode, covered with a monolayer of dye molecules. Upon photoexcitation of the dye an electron is injected into the conduction band of the TiO₂. A redox couple (I⁻/I₃⁻) in an electrolyte solution covering the whole TiO₂ electrode regenerates the dye, and is itself in return regenerated at the counter electrode. The layout of the DSSC is shown in figure 1.5. Often, transition metal complexes are used as dyes, e.g. RuL₂-(NCS)₂ (known as N3 dyes), where L is a π -conjugated ligand with TiO₂ anchoring groups⁶⁷. The best DSSCs reach efficiencies higher than 10% measured under AM1.5 solar irradiation⁶⁷.

The main drawback of the traditional DSSC, hampering wide use, is the application of a liquid electrolyte. This liquid electrolyte is often related to its poor thermo-stability, and responsible for the corrosion of the Pt covered counter electrode. For this reason alternatives for an electrolyte, are being developed, aiming at solid-state version of the DSSC. Current 'state of the art' quasi-solid-state dye-

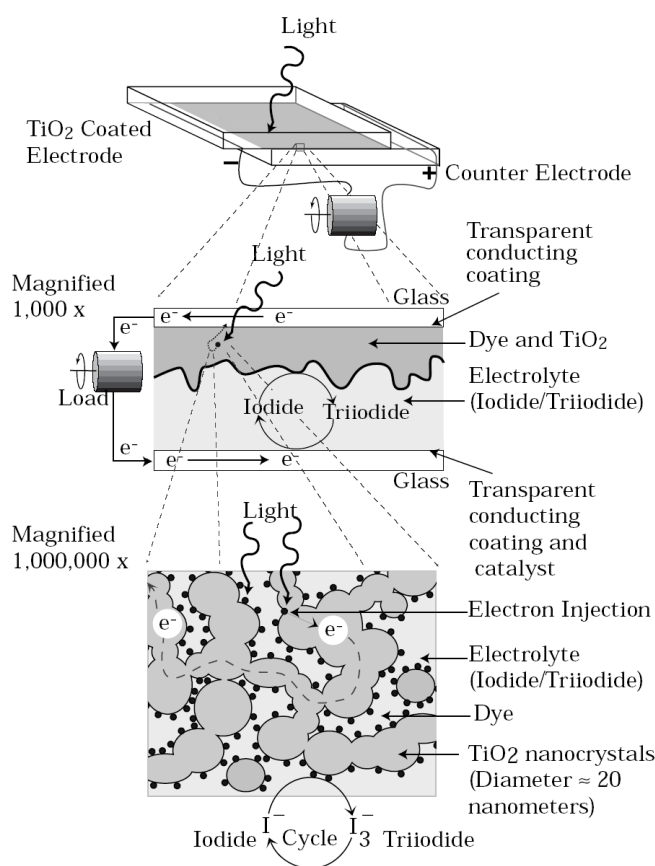


Figure 1.5 Schematic scheme of the traditional dye-sensitized solar cell.⁶⁸

sensitized solar cells based on the iodide/triiodide redox couple, reach stable and > 6% efficient solar cells⁶⁹. Commercial application of this type of solar cells in consumer products is currently explored by Hitachi-Maxell for application in a film-like lightweight solar battery⁷⁰. One recent result, also by the Grätzel group, is a solvent-free dye-sensitized solar cell based on an ionic liquid electrolyte and using $\text{SeCN}^-/(\text{SeCN})_3^-$ as the redox couple, replacing the iodide/triiodide redox couple. This solar cell reaches measured AM1.5 efficiencies of 8%⁷¹. Another elegant example of recent progress is the quasi solid-state tandem DSSC developed by Dürre and coworkers⁷². The device layout and working principle are shown in figure 1.6. Two separate dye-sensitized cells are connected in parallel and placed on top of each other. The cell first exposed to illumination contains a red dye, the other a so-called black dye. This assures an effective absorption of the solar emission, leading to a high power conversion efficiency of 10.5%, measured under AM1.5 conditions.

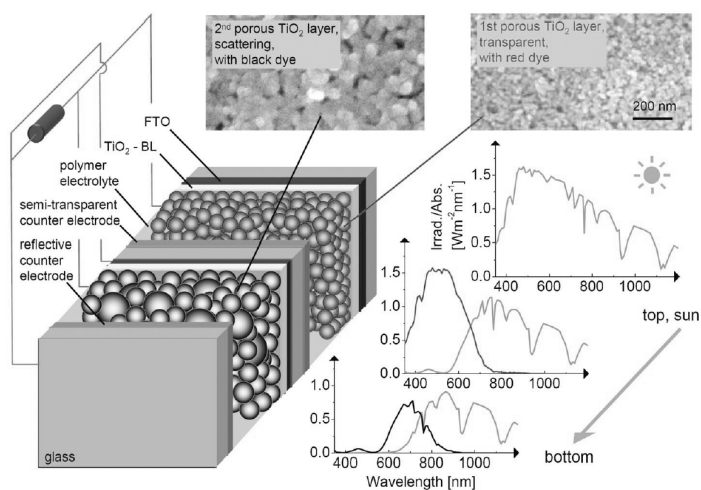


Figure 1.6 A quasi solid-state DSSC tandem cell.

Replacing the I^-/I_3^- redox couple and the electrolyte with a solid-state hole conducting species like inorganic CuSCN ⁷³ or the organic hole conductor spiro-OMeTAD⁷⁴ gave measured solar conversion efficiencies of 2 and 3.2% respectively. It seems more challenging to find a polymeric hole transport material, problems with filling the TiO_2 electrode and low hole mobility limit the efficiency of these devices. DSSCs where the electrolyte is replaced by a hole conducting polymer, were fabricated using poly(3-octylthiophene)⁷⁵, leading to a low estimated efficiency of 0.16%. In situ photoelectrochemically polymerized PEDOTs⁷⁶ have also been used in an attempt to overcome the filling problems of the TiO_2 electrode. This leads to devices with a moderate estimated efficiency of 0.53%.

The ultimate goal is to replace both the dye and electrolyte with a conjugated polymer, which will function as the light harvesting species and as hole transport material. This is the subject of the next section where hybrid polymer solar cells are discussed.

1.2.5 Hybrid polymer solar cells

The main disadvantage of a solid state DSSC utilizing Ru dyes as sensitizers is the weak absorption of visible light by these dyes. Because only a monolayer is adsorbed on the surface of the TiO₂ a strong absorbance requires a very high surface area and hence a very thick nanocrystalline TiO₂ film. However this also requires an effective hole transport over micrometer distances to the counter electrode. Combined with the filling problems of the nanoporous TiO₂, this limits the performance of solid-state dye-sensitized solar cells.

The high extinction coefficients ($> 10^7 \text{ m}^{-1}$) found in conjugated polymers like MDMO-PPV makes them viable candidates to replace both the dyes and the electrolyte. Therefore it is believed that the combination of n-type semiconducting inorganic materials and p-type conjugated polymers will lead to a simple and effective solar cell. There are various approaches to construct hybrid materials consisting of inorganic semiconductors and conjugated polymers that meet the requirements for application in solar cells. The ones that have been described so far are:

1. Filling (nano)-structured metal-oxide electrodes with conjugated polymers.
2. Blending pre-synthesized (nano)-particles with conjugated polymers.
3. In situ synthesis of n-type material: blending conjugated polymers with metal-oxide precursors, allowing a subsequent hydrolysis and condensation into the desired oxide.

The first approach is an extension of the solid state DSSC concept. The conjugated polymer takes care of the hole transport, replacing the electrolyte medium. Using a conjugated polymer that also absorbs light, leads to a solar cell where both functions are taken care of by a single component. As shown for the (semi) solid state DSSC, filling the TiO₂ electrode with polymers is far from simple. The nano-structured TiO₂ electrode should be made more accessible for polymers to penetrate fully in order to make well performing photovoltaic devices. Circumventing filling problems by in-situ polymerization of polythiophene in the pores of the TiO₂ layer, only leads to moderate photovoltaic effects⁷⁷, and this effect is dependent on the doping level of the polythiophene⁷⁸. Bi-layer devices consisting of flat TiO₂ are limited in efficiency due to a small contact interfacial area and limited charge carrier generation. The highest estimated AM1.5 efficiency of 0.3 % has been achieved for bilayer devices constructed from MDMO-PPV and flat TiO₂ layers⁷⁹. For bilayer devices constructed from MEH-PPV and flat layer TiO₂ only moderate external quantum efficiencies (EQE) of 2% have been reported. Replacing the flat layer with a nanocrystalline electrode increased the EQE up to 6%, and gives a moderate estimated power conversion efficiency of 0.18 %⁸⁰. Filling the pores of a nanocrystalline TiO₂ electrode with a better hole transporting fluorene-thiophene copolymer⁸¹ leads to external quantum efficiencies of 13%. When the MEH-PPV is replaced with the better hole transporting M3EH-PPV a bilayer device with an estimated efficiency of 0.4% has been obtained⁶⁵.

Spin casting a mixture of M3EH-PPV and PCNEPV on top of the TiO₂ layer, increases this efficiency to 0.75%⁶⁵.

The challenge remains to increase the contact area between the inorganic phase and the polymer. Pre-synthesizing the electrode allows for optimizing dimensions, small enough for all excitons to reach the junction, but still allowing a simple and effective filling of the electrodes. Coakley *et al.* have reported a very nice example^{82,83}: mesoporous titania films were synthesized using the structure directing properties of block copolymers. The TiO₂ films formed this way have a regular and open structure with pores of approximately 10 nm (see figure 1.7), which can be filled with regio-regular polyalkylthiophenes. Infiltration of the mesoporous TiO₂ has been performed by heat treatment of a spin-cast polymer film. External quantum efficiencies of 10%, and a measured AM1.5 power conversion efficiency of 0.45 % have been obtained.

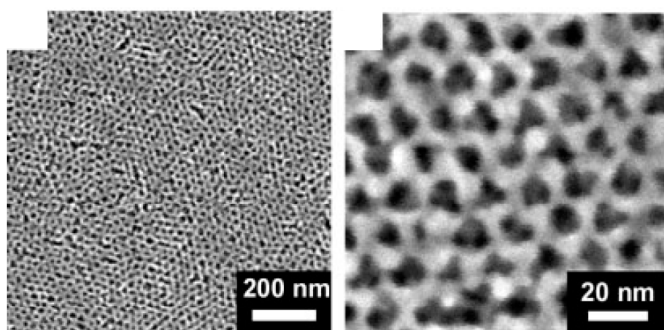


Figure 1.7 Mesoporous titania films made using the structure directing properties of block copolymers, after the TiO₂ network is formed the polymers are removed and the TiO₂ is crystallized by calcination at 400°C⁸³.

A Palo Alto, California-based startup Nanosolar⁸⁴, is exploring the latest technologies to self-assemble nanomaterials into highly ordered nanostructured materials. The pores in such material are filled with conducting polymers. The whole active layer is printed onto a metal foil, which speeds up processing of the solar cells. Their aim is to reach 10% efficiency at the end of 2005.

Another example, but not optimal for application in hybrid polymer solar cells, is the work of Vayssieres^{85,86}, on oriented ZnO morphologies (figure 1.8). The dimension of the voids between the ZnO pillars is much larger than the exciton diffusion length, therefore filling will be easier but charge generation not likely very effective.

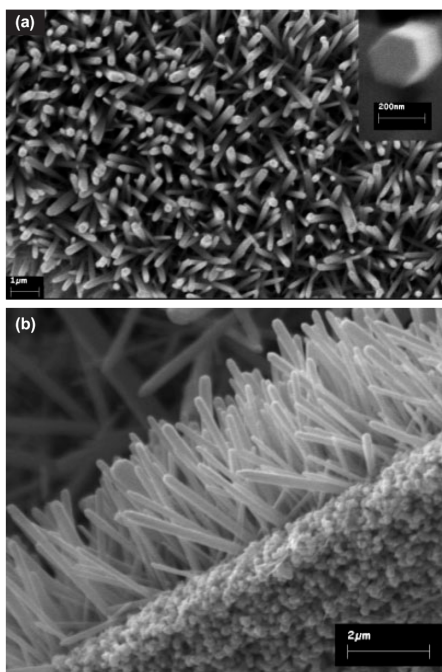


Figure 1.8 Structured ZnO electrodes made via a simple wet chemical procedure, showing well-aligned ZnO rods.

One other approach is the inverse of this first one. Instead of making a nanostructured inorganic material, the conjugated polymer is structured and filled afterwards with inorganic material. This approach is currently unexplored but interesting enough to mention its possibility. Highly crystalline, small nanoparticles can be prepared and have been used to fill porous membranes⁸⁷. However, it is a challenge to make porous polymer films. One approach might be a mixture of poly-(*p*-xylylene- α -tetrahydrothiophenium chloride) (a precursor for PPV) and a thermally degradable polycarbonate⁸⁸. Because conversion into PPV, and the degradation of the polycarbonate coincide at temperatures from 200-250 °C, this might lead to a porous PPV film. Another route might be by utilizing copolymers, having one conjugated block and one thermally degradable block. No examples of this route have appeared so far. It is likely that several difficulties have to be overcome.

The second approach circumvents filling problems by using the approach of the bulk heterojunction solar cell, nanoparticles of inorganic materials are mixed with conjugated polymers and blended in a film. This approach is in essence very simple and applicable for large areas. The challenge is to mix the inorganic and organic materials. First examples on blends from TiO₂ nanoparticles and PPV have shown only moderate external quantum efficiencies of a few percent and short circuit currents of tens of microamperes^{89,90}. Poor mixing of the polymer and the nanoparticles, and agglomerates of

nanoparticles in the blend limit their performance. The best example so far from blends of TiO_2 and a conjugated polymer has been shown for poly(3-hexylthiophene) (P3HT) by Kwong *et al.* in their recent paper¹⁴ showing external quantum efficiencies up to 16% and an AM1 power conversion efficiency of 0.42%.

Other semiconducting nanoparticles have also been used. CuInSe_2 , is a promising material to replace silicon in thin film solar cells. CuInSe_2 nanoparticles blended with P3HT indeed show a small photovoltaic effect with currents of 0.3 mA cm^{-2} and an open circuit voltage of 1.0 V ¹³. The best photovoltaic response so far has been realized using CdSe nanoparticles mixed with conjugated polymers. In contrast to TiO_2 , these particles also harvest solar light and the size of the nanoparticles can be tuned for optimal light absorption. First examples on CdSe nanoparticles in MEH-PPV⁹¹, show external quantum efficiencies up to 12%. The surface chemistry of the nanoparticles is important. After synthesis, these particles are capped with trioctylphosphineoxide (TOPO). For efficient electron transfer this surfactant has to be removed. A major improvement came with the introduction of CdSe rods combined with P3HT^{12,92}. CdSe rods allow for a more efficient electron transport through the film, and the P3HT is a better hole-transporting polymer. Figure 1.9 shows the device layout and TEM-pictures of CdSe rods and dots.

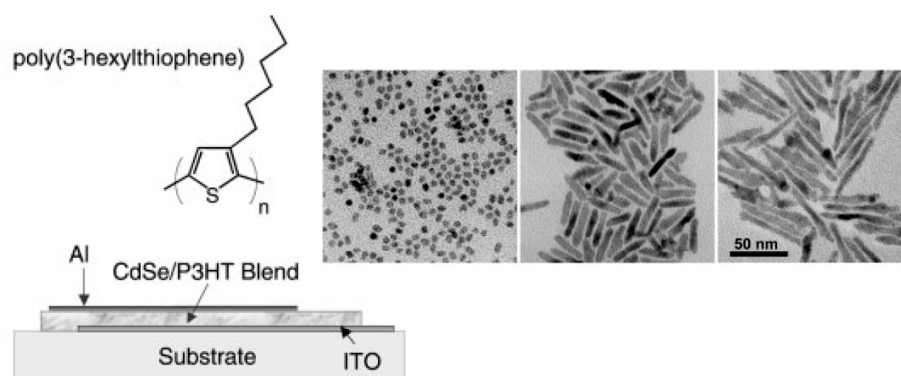


Figure 1.9 Schematic layout of a hybrid solar cell consisting of CdSe nanorods (90 wt%) in P3HT¹². TEM pictures of dots and rods, with the high aspect ratios are shown on the right⁹².

The challenge is to keep these rods soluble in organic solvents. This has been achieved by the replacement of the TOPO by pyridine, which makes these rods soluble in pyridine-chloroform mixtures. Photovoltaic devices prepared in this way are still the best hybrid polymer solar cells reported so far, giving external quantum efficiencies up to 60%, short circuit currents of 5.7 mA cm^{-2} , an open circuit voltage of 0.7 V and a fill factor of 0.4, under AM1.5 illumination with a power conversion efficiency of 1.7 %¹². One evident drawback of rods is that they only improve transport in the direction of their alignment, which in a thin film device is unlikely to be from one electrode to the other. CdSe tetrapods can be used to overcome this drawback, because these tetrahedrally branched structures cannot lie in a plane. It has recently been shown that compared to linear CdSe nanorods in

MDMO-PPV, branched CdSe tetrapods indeed give an improved electron transport leading to solar cells with a measured AM1.5 efficiency of 1.8%.⁹³ Solar cells based on CdSe and conjugated polymers are currently the best performing hybrid polymer solar conversion devices, Nanosys, a Palo Alto, California-based nanotechnology company is developing systems based on CdSe nanoparticles and rods for commercial application in lightweight high efficiency photovoltaics⁹⁴.

The third approach, making use of precursors for metal oxides (or any other semiconductor), and converting them in-situ into their semiconducting material, is an attractive one as it promises a very simple procedure for making hybrid bulk heterojunction solar cells. The challenge is to control morphology and crystallinity, as these affect the electron transport in the material. Mixing a precursor for TiO₂, such as Ti(*i*-PrO)₄ (titanium(IV) isopropoxide) that readily hydrolyses upon exposure to moisture, with MDMO-PPV, indeed leads to working photovoltaic devices⁹⁵ with estimated solar conversion efficiencies reaching 0.22%⁹⁶. Formation of crystalline TiO₂ is inhibited at low temperatures and limits the electron mobility in this device. Replacing the TiO₂ with ZnO, which readily forms crystalline phases at low temperatures, might be an attractive alternative.

1.3 Objective and outline of this thesis

As shown in this introduction the combination of inorganic semiconducting materials and conjugated polymers is an attractive route towards simple and low cost photovoltaic devices, and will be the focus of this thesis. Non-toxic materials are studied in an effort to reach 'green' photovoltaic devices, therefore not exploring the use of CdSe but TiO₂ and ZnO instead, ZnO has also proven its application in dye-sensitized solar cells⁹⁷ and TiO₂ has been used in hybrid polymeric devices as well. Two of the three approaches to construct hybrid materials consisting of inorganic semiconductors and conjugated polymers will be explored. The main objective of this thesis is to explore the use of these hybrid materials in bulk heterojunction type polymer solar cells. The second approach, which explores the use of presynthesized nanoparticles, has proven to be successful using CdSe nanoparticles. This approach will be explored using ZnO nanoparticles. Bulk heterojunction solar cells will be constructed from ZnO nanoparticles and conjugated polymers. The third approach, the concept of in situ generation of metal oxides inside a polymer matrix, has proven to be effective using TiO₂ precursors. This last approach will be extended to ZnO, aiming at an improved performance due to higher crystallinity of the inorganic phase.

The second chapter explores the subject of heterosupramolecular chemistry, *i.e.* synthesis of supramolecular structures consisting of a condensed inorganic phase and an organic moiety. A heterosupramolecule consisting of a terthiophene attached to a TiO₂ nanoparticle is used to study the interaction between isolated polymer-like organic molecules and inorganic semiconductors.

Chapter 3 introduces ZnO as electron accepting species. The need for soluble nanoparticles is discussed and a synthesis of soluble ZnO nanoparticles is presented. Small (5 nm) crystalline ZnO nanoparticles can be made and can in a second step be converted into ZnO nanorods. The electrical and optical properties of the nanoparticles are characterized using different techniques. These nanoparticles appear very suitable for blending with conjugated polymers.

In chapter 4 the characterization of photovoltaic devices is explained in detail. The photovoltaic effect found in blends of ZnO nanoparticles and conjugated polymers, is studied as a function of the amount of ZnO, and the film thickness of the active blend layer. Light intensity dependence measurements, and incident photon to current conversion efficiencies, give insight into the factors that limit the performance of this solar cell. The photophysical properties and the morphology of these blends are examined in more detail in chapter 5. Different techniques are used to gain insight in the effectiveness of the electron transfer. Time-resolved microwave conductivity and analysis of J - V characteristics are used to study the electron mobility in these blends. TEM and AFM are used to relate the morphology of the blends to the performance of the solar cells.

The last chapter covers the in-situ generation of ZnO in MDMO-PPV. In contrast to TiO₂ it is possible to make crystalline ZnO at relatively low temperatures. Blends of in-situ generated ZnO and MDMO-PPV are characterized and their photovoltaic effect is studied. The extension of the in-situ concept to ZnO leads to a significant enhancement of the photovoltaic effect. Together with the promising results shown with blends from MDMO-PPV and ZnO nanoparticles, this raises high expectations for further research on application of ZnO in green photovoltaic devices.

- 1 Gomez-Romero, P. *Adv. Mater.* **2001**, *13*, 163.
- 2 Xiong, M.; Gu, G.; Wu, L. *J. Appl. Pol. Sci.* **2003**, *90*, 1932.
- 3 Hazan, I.; Rummel, M. U.S. Patent No. 5,162,426 (1992).
- 4 Sanchez, C.; Lebeau, B.; Chaput, F.; Boilot, J-P. *Adv. Mater.* **2003**, *15*, 1969.
- 5 Dirix, Y.; Bastiaansen, C.; Casero, W.; Smith, P. *Adv. Mater.* **1999**, *11*, 223.
- 6 Vaia, R. A.; Giannelles, E.P. *MRS Bulletin* **2001**, 394.
- 7 Gangopadhyay, R.; De, A. *Chem. Mater.* **2000**, *12*, 608.
- 8 a) Shirakawa, H.; Louis, E. J.; MacDiarmid, A. G.; Chiang, C. K.; Heeger A. J. *Chem. Commun.* **1977**, 578. b) Chiang, C. K.; Fincher, C. R., Jr.; Park, Y. W.; Heeger, A. J.; Shirakawa, H.; Louis, E. J. *Phys. Rev. Lett.* **1977**, *39*, 1098.
- 9 Sirringhaus, H.; Brown, P. J.; Friend, R. H.; Nielsen, M. M.; Bechgaard, K.; Langeveld-Voss, B. M. W.; Spiering, A. J. H.; Janssen, R. A. J.; Meijer, E. W.; Herwig, P. T.; de Leeuw, D. M. *Nature* **1999**, *401*, 685.
- 10 Babel, A.; Jenekhe, S. A. *J. Am. Chem. Soc.* **2003**, *125*, 13656.
- 11 Sanchez, C.; Soler-Illia, G.; Ribot, F.; Lalot, T.; Mayer, C. R.; Cabuil, V. *Chem. Mater.* **2001**, *13*, 3061.
- 12 Huynh, W. U.; Dittmer, J. J.; Alivisatos, A. P. *Science* **2002**, *295*, 2425.
- 13 Arici, E.; Hoppe, H.; Schäffler, F.; Meissner, D.; Malik, M. A.; Sariciftci, N. S. *Thin Solid Films* **2004**, *451-452*, 612.
- 14 Kwong, C. Y.; Djurišić, A. B.; Chui, P. C.; Cheng, K. W.; Chan, W. K. *Chem. Phys. Lett.* **2004**, *384*, 372.
- 15 Coe-Sullivan, S.; Woo, W-K.; Steckel J. S.; Bawendi, M. G.; Bulovic, V. *Org. Electr.* **2003**, *4*, 123.
- 16 Carter, S. A.; Scott, J. C.; Brock, P. J. *Appl. Phys. Lett.* **1997**, *71*, 1145.
- 17 Dabbousi, B. O.; Bawendi, M. G.; Onitsuka, O.; Rubner, M. F. *Appl. Phys. Lett.* **1995**, *66*, 1316.
- 18 Blom, P. W. M.; Schoo, H. F. M.; Matters, M. *Appl. Phys. Lett.* **1998**, *73*, 3914.
- 19 Hide, F.; Schwartz, B. J.; Díaz-García, M. A.; Heeger, A. J. *Chem. Phys. Lett.* **1996**, *256*, 424.
- 20 Sotzing, G. A.; Phend, J. N.; Grubbs, R. H.; Lewis, N. S. *Chem. Mater.* **2000**, *12*, 593.
- 21 Covington, J. A.; Gardner, J. W.; Briand D.; De Rooij, N. F. *Sens. Actuators B* **2001**, *77*, 155.
- 22 Möller, S.; Perlov, C.; Jackson, W.; Taussig, C.; Forrest S. R. *Nature* **2003**, *426*, 166.
- 23 Goward, G. R.; Leroux, F.; Nazar, L. F. *Electrochim. Acta* **1998**, *43*, 1307.
- 24 Gomez-Romero, P.; Chojak, M.; Cuentas-Gallegos, K.; Asenio, J. A.; Kulesza, P. J.; Casan-Pastor, N. Lira-Cantu, M. *Electrochem. Commun.* **2003**, *5*, 149.
- 25 EvidentTechnologies, 216 RiverStreet, Troy, NewYork (commercial application as phosphor in traditional LEDs, however not based on semiconducting polymer composites)
- 26 Katsoulis, D. *Chem. Rev.* **1998**, *98*, 359.
- 27 In chapter 4, section 4.2 more details about the characterization of solar cell efficiencies are given.
- 28 Kroon, J. M.; Wienk, M. M.; Verhees, W. J. H.; Hummelen, J. C. *Thin Solid Films* **2002**, *403-404*, 223.
- 29 The open-circuit voltage (V_{OC}) is the voltage measured under illumination when the current is zero.

- 30 $FF = \frac{J_{MPP} \times V_{MPP}}{J_{SC} \times V_{OC}}$, $J_{MPP} \times V_{MPP}$ stands for the maximum power point on the J - V curve between 0 volt and the V_{OC} .
- 31 Chapin, D. M.; Fuller, C. S.; Pearson, G. L. *J. Appl. Phys.* **1954**, *25*, 676.
- 32 <http://emsolar.ee.tu-berlin.de/~ilse/solar/gifs/solar61e.gif>
- 33 Goetzberger, A.; Hebling, C.; Schock, H-W. *Mater. Sci. Eng.* **2003**, *R40*, 1.
- 34 Data taken from ref. 26: world market shares in 2001.
- 35 Heeger, A. J. *J. Phys. Chem. B* **2001**, *105*, 8476.
- 36 Brabec, C. J.; Sariciftci, N. S.; Hummelen, J. C. *Adv. Mater.* **2001**, *11*, 15.
- 37 Campbell, I. H.; Hagler, T. W.; Smith D. L.; Ferrasis, J. P. *Phys. Rev. Lett.* **1996**, *76*, 1900.
- 38 Schweitzer, B.; Bäessler, H. *Synth. Met.* **2000**, *109*, 1.
- 39 Hendry, E.; Schins, J. M.; Candeias, L. P.; Siebbeles, L. D. A.; Bonn, M. *Phys. Rev. Lett.* **2004**, *92*, 196601-1.
- 40 Markov, D. E.; Amsterdam, E.; Blom, P. W. M.; Sieval, A. B.; Hummelen, J. C. *SPIE Proc.* **2004**, *5464*, 449.
- 41 Halls, J. J. M.; Pichler, K.; Friend, R. H.; Moratti, S. C.; Holmes, A. B. *Appl. Phys. Lett.* **1996**, *68*, 3120.
- 42 Savenije, T. J.; Warman, J. M.; Goossens, A. *Chem. Phys. Lett.* **1998**, *287*, 148.
- 43 Kroeze, J. E.; Savenije, T. J.; Vermeulen, M. J. W.; Warman, J. M. *J. Phys. Chem. B.* **2003**, *107*, 7696.
- 44 Stübinger, T.; Brütting, W. *J. Appl. Phys.* **2001**, *90*, 3632.
- 45 Gregg, B. A.; Sprague, J.; Peterson, M. W. *J. Phys. Chem. B.* **1997**, *101*, 5362.
- 46 As Gregg *et al.* (ref 45) state in their paper: shorter exciton diffusion lengths ($\sim 0.25 \mu\text{m}$) for perylene based materials, are more often reported (see their reference 10 and 37 for details). According to their discussion, the large exciton diffusion length of $2.5 \mu\text{m}$ can be considered as an accurate value and indicates excitons can be transferred over large distances in perylene films.
- 47 Tang, C. W. *Appl. Phys. Lett.* **1986**, *48*, 183.
- 48 Gebeyehu, D.; Pfeiffer, M.; Maennig, B.; Drechsel, J.; Werner, A.; Leo, K. *Thin Solid Films* **2004**, *451-452*, 29.
- 49 Xue, J.; Uchida, S.; Rand, B. P.; Forrest, S. R. *Appl. Phys. Lett.* **2004**, *84*, 3013.
- 50 Peumans, P.; Uchida, S.; Forrest, S. R. *Nature* **2003**, *425*, 158.
- 51 Uchida, S.; Xue, J.; Rand, B. P.; Forrest, S. R. *Appl. Phys. Lett.* **2004**, *84*, 4218.
- 52 Yu, G.; Gao, J.; Hummelen, J. C.; Wudl, F.; Heeger, A. J. *Science* **1995**, *270*, 1789.
- 53 Van Duren, J. K. J.; Yang, X.; Loos, J.; Bulle-Lieuwma, C. W. T.; Sieval, A. B.; Humelen, J. C.; Janssen, R. A. J. *Adv. Func. Mater.* **2004**, *14*, 425.
- 54 Martens, T.; Munters, T.; Goris, L.; D'Hean, J.; Schouteden, K.; D'Olieslaeger, M.; Lutsen, L. Vanderzande, D.; Geens, W.; Poortmans, J.; De Schepper, L; Manca, J. V. *Appl. Phys. A* **2004**, *79*, 27.
- 55 Shaheen, S. E.; Brabec, C. J.; Sariciftci, N. S.; Padinger, F.; Fromherz, T.; Hummelen, J. C. *Appl. Phys. Lett.* **2001**, 841.

- 56 Wienk, M. M.; Kroon, J. M.; Verhees, W. J. H.; Knol, J.; Hummelen, J. C.; Van Hal, P. A.; Janssen, R. A. J. *Angew. Chem. Int. Ed.* **2003**, *42*, 3371.
- 57 Padinger, F.; Rittberger, R. S.; Sariciftci, N. S. *Adv. Funct. Mater.* **2003**, *13*, 85.
- 58 Brabec, C. J. *Sol. Energy Mater. Sol. Cells* **2004**, *83*, 273.
- 59 Tanase, C.; Meijer, E. J.; Blom, P. W. M.; De Leeuw, D. M. *Phys. Rev. Lett.* **2003**, *91*, 216601.
- 60 Melzer, C.; Koop, E. J.; Mihailetschi, V. D.; Blom, P. W. M. *Adv. Funct. Mater.* **2004**, *14*, 865.
- 61 Konarka Technologies has acquired Siemens AG's organic PV in 2004. First commercial products are already expected in 2005.
- 62 PCNEPV: poly-[oxa-1,4-phenylene-(1-cyano-1,2-vinylene)-(2-methoxy-5-(3,7-dimethyloctyloxy)-1,4-phenylene)-1,2-(2-cyanovinylene)-1,4-phenylene]
- 63 Veenstra, S. C.; Verhees, W. J. H.; Kroon, J. M.; Koetse, M. M.; Sweelssen, J.; Bastiaansen, J. J. A. M.; Schoo, H. F. M.; Yang, X.; Alexeev, A.; Loos, J.; Schubert, U. S.; Wienk, M. M. *Chem. Mater.* **2004**, *16*, 2503.
- 64 M3EH-PPV: poly[2,5-dimethoxy-1,4-phenylene-1,2-ethenylene-2-methoxy-5-(2-ethylhexyloxy)-1,4-phenylene-1,2-ethenylene]
- 65 Breeze, A. J.; Schlesinger, Z.; Carter, S. A.; Tillmann, H.; Hörhold, H.-H. *Sol. Energy Mater. Sol. Cell* **2004**, *83*, 263.
- 66 O'Regan, B.; Grätzel, M. *Nature* **1991**, *353*, 737.
- 67 Hagfeldt, A.; Grätzel, M. *Acc. Chem. Res.* **2000**, *33*, 269.
- 68 Smestad, G. P.; Grätzel, M. *J. Chem. Edu.* **1998**, *75*, 752.
- 69 Wang, P.; Zakeeruddin, S. M.; Moser, J. E.; Nazeeruddin, M. K.; Sekiguchi, T.; Grätzel, M. *Nature Materials* **2003**, *2*, 402.
- 70 Hitachi, Ltd. presented dye-sensitized solar cells at the 'Eco-Products Exhibition', Tokyo, December 2003.
- 71 Wang, P.; Zakeeruddin, S. M.; Moser, J.-E.; Humphry-Baker, R.; Grätzel, M. *J. Am. Chem. Soc.* **2004**, *126*, 7164.
- 72 Dürr, M.; Bamedi, A.; Yasuda, A.; Nelles, G. *Appl. Phys. Lett.* **2004**, *84*, 3397.
- 73 O'Regan, B.; Lenzenmann, F.; Muis, R.; Wienke, J. *Chem. Mater.* **2002**, *14*, 5023.
- 74 Krüger, J.; Plass, R.; Grätzel, M.; Matthieu, H.-J. *Appl. Phys. Lett.* **2002**, *81*, 367.
- 75 Gebeyehu, D.; Brabec, C. J.; Sariciftci, N. S.; Vangeneugden, D.; Kiekebooms, R.; Vanderzande, D.; Kienberger, F.; Schindler, H. *Synth. Met.* **2002**, *125*, 279.
- 76 Saito, Y.; Fukuri, N.; Senadeera, R.; Kitamura, T.; Wada, Y.; Yanagida, S. *Electrochem. Commun.* **2004**, *6*, 71.
- 77 Huisman, C. L.; Huijser, H.; Donker, H.; Schoonman, J.; Goossens, A. *Macromolecules* **2004**, *37*, 5557.
- 78 Kajihara, K.; Tanaka, K.; Hirao, K.; Soga, N. *Jpn. J. Appl. Phys.* **1997**, *36*, 5537.
- 79 Slooff, L. H.; Kroon, J. M.; Loos, J.; Koetse, M. M.; Sweelssen, J. *Adv. Funct. Mater.* In press.
- 80 Breeze, A. J.; Schlesinger, Z.; Carter, S. A.; Brock, P. J. *Phys. Rev. B.* **2001**, *64*, 125205-1.

-
- 81 Ravirajan, P.; Haque, S. A.; Durrant, J. R.; Poplavskyy, D.; Bradley, D. D. C.; Nelson, J. J. *Appl. Phys.* **2004**, *95*, 1473.
- 82 Coakley, K.; McGehee, M. D. *Appl. Phys. Lett.* **2003**, *83*, 3380.
- 83 Coakley, K.; Liu, Y.; McGehee, M. D.; Frindell, K. L.; Stucky, G. D. *Adv. Funct. Mater.* **2003**, *13*, 301.
- 84 Nanosolar, Inc. Palo Alto, CA. <http://www.nanosolar.com> see *Technology Review*, **2004**, *July/August*, p34 for more information.
- 85 Vayssieres, L.; Keis, K.; Lindquist, S-T.; Hagfeldt, A. *J. Phys. Chem. B.* **2001**, *105*, 3350.
- 86 Vayssieres, L. *Adv. Mater.* **2003**, *15*, 464.
- 87 Lakshmi, B. B.; Dorhout, P. K.; Martin, C. R. *Chem. Mater.* **1997**, *9*, 857.
- 88 Fréchet J. M. J.; Houlihan, F. M.; Bouchard, F.; Kryczka, B; Wilson, C. G. *J. Chem. Soc. Commun.* **1985**, 1514.
- 89 Salafsky, J. S.; Lubberhuizen, W. H.; Schropp, R. E. I. *Chem. Phys. Lett.* **1998**, *290*, 297.
- 90 Arango, A. C.; Carter, S. A.; Brock, P. J. *Appl. Phys. Lett.* **1999**, *74*, 1698.
- 91 Greenham, N. C.; Peng, X.; Alivisatos, A. P. *Phys. Rev. B.* **1996**, *54*, 17628.
- 92 Huynh, W. U.; Dittmer, J. J.; Libby, W. C.; Whiting, G. L.; Alivisatos, A. P. *Adv. Funct. Mater.* **2003**, *13*, 73.
- 93 Sun, B; Marx, E.; Greenham, N. C. *Nano Lett.* **2003**, *3*, 961.
- 94 Nanosys, Palo Alto, California, <http://www.nanosysic.com>
- 95 Van Hal, P. A.; Wienk, M. M.; Kroon, J. M.; Verhees, W-J. H.; Slooff, L. H.; Van Gennip, W. J. H.; Jonkheijm, P.; Janssen, R. A. J. *Adv. Mater.* **2003**, *15*, 118.
- 96 Slooff, L. H.; Wienk, M. M.; Kroon, J. M. *Thin Solid Films* **2004**, *451-452*, 634.
- 97 Keis, K.; Magnusson, E.; Lindström, H.; Lindquist, S-T.; Hagfeldt, A. *Sol. Energy Mater. Sol. Cell* **2002**, *73*, 51.

Chapter 2

Heterosupramolecular chemistry:

Heterosupramolecules from organic π -conjugated systems and TiO_2 nanoparticles as model compounds for electron transfer studies

Abstract

The heterosupramolecular approach is used to study the interaction between inorganic nanoparticles and organic polymer-like materials. Titanium dioxide nanoparticles smaller than 3 nm in size have been prepared and characterized. The nanoparticles are soluble in common apolar organic solvents and bind to acid functionalized π -conjugated oligomers to form heterosupramolecular assemblies. When [2,2';5',2'']terthiophene-5-carboxylic acid is coupled to the nanoparticles, the photoluminescence of the terthiophene moiety of the heterosupramolecular system is completely quenched due to a photoinduced electron transfer from terthiophene to titanium dioxide. The distance dependence of photoinduced charge transfer in hybrid organic-inorganic systems has been investigated using heterosupramolecular assemblies of TiO_2 nanoparticles and fluorescent conjugated terthiophene oligomers, connected via saturated spacers with 5, 9, and 13 single bonds. In chloroform, the rate for charge transfer in these oligomer- TiO_2 conjugates decreases with increasing spacers length from 2.5×10^{10} to $1.6 \times 10^9 \text{ s}^{-1}$. Hence, charge transfer is relatively fast, even for the longest linker. The rate constant does not follow a simple exponential decay with spacer length and the logarithmic attenuation per bond is relatively low ($0.3 < \beta < 0.6$). This effect has been discussed in terms of back folding or amplification of the electronic coupling by proximate alkyl chains on the surface of the nanoparticle.

2.1 Introduction to heterosupramolecular chemistry

Donald Fitzmaurice introduced the term heterosupramolecular chemistry in 1994¹. The concept of heterosupramolecular chemistry is based on that of supramolecular chemistry as defined by Jean-Marie Lehn. A heterosupramolecule is formed by covalently or non-covalently linking a condensed phase and molecular components. Its properties are not a simple superposition of the properties of the components, but the assembly creates a new heterosupramolecular function². The definition of heterosupramolecules shows great resemblance to the definition for hybrid materials as given in chapter 1; a heterosupramolecule is a hybrid material on a molecular scale. Two examples of associated heterosupramolecular functions are shown in figure 2.1. The first exists of gold nanoparticles covered with a disulfide biotin analogue (DSBA), used for molecular recognition³. When mixed with streptavidin proteins, the gold nanoparticles agglomerate, which results in a color change of the sol from red to blue. In this case the distance dependant optical properties of gold nanoparticles are used to monitor molecular recognition of proteins. The second examples shows TiO₂ nanoparticles bound to viologen derivatives that exhibit a photoinduced electron transfer from TiO₂ to the viologen⁴. One other nice example is given by Kamat *et al.*, who show photoinduced electron transfer from a pyrene moiety to a gold nanoparticle in a pyrene-gold nano-assembly⁵.

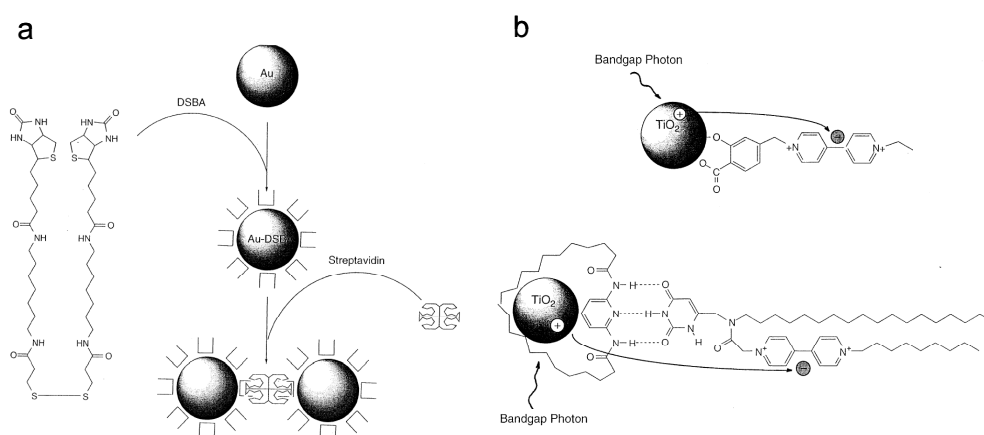


Figure 2.1 Examples of added heterosupramolecular function. a) Molecular recognition of a streptavidin enzyme by DSBA coated gold nanoparticles. b) Photoinduced electron transfer from a TiO₂ nanoparticle to a viologen derivative.

This thesis focuses on hybrid materials having photoinduced electron transfer as added value; the individual components ensure the electron and hole transport, necessary for an efficient photovoltaic effect. The objective of this chapter is to investigate photoinduced electron transfer from π -conjugated oligomers to TiO₂ nanoparticles, mimicking the interactions as found in solid state dye sensitized solar cells, where the dye and electrolyte have been replaced by a conjugated polymer. A

heterosupramolecule consisting of a π -conjugated oligomer and a TiO_2 nanoparticle is a viable candidate to study this interaction in solution, without interference caused by multiple polymer-polymer and polymer-nanoparticle interactions. For this goal, heterosupramolecular assemblies have been constructed from functionalized π -conjugated oligomers, and nanosized TiO_2 particles that have been solubilized in common (apolar) organic solvents by stearate surface modification. Excited-state electron transfer within these heterosupramolecular assemblies is studied as a function of the type of functional group and the distance between the chromophore and the TiO_2 nanoparticle.

2.2 TiO_2 nanoparticle synthesis and characterization

2.2.1 TiO_2 nanoparticle preparation

TiO_2 nanoparticles were prepared via arrested hydrolysis⁶ of titanium(IV) isopropoxide in anhydrous chloroform containing anhydrous 1-propanol (5 vol.-%) and 2.6 mol equiv. doubly distilled water in the presence of stearic acid (1 mol equiv.) as a surfactant to solubilize the nanoparticles in the organic solvent. After stirring, a colorless and nonscattering solution was obtained. Purification of the nanoparticles was achieved by precipitation from solution using acetonitrile. A similar procedure applied by Wu *et al.*⁷ using TiCl_4 and stearic acid leads to 6-8 nm sized nanoparticles that are soluble in acetone, THF and alkanes. The as prepared nanoparticles did not give rise to clear XRD signals, indicating their poor crystallinity.

2.2.2 Compositional analysis

To establish that the arrested hydrolysis indeed forms TiO_2 , X-ray photoelectron spectroscopy (XPS) was performed on the purified nanoparticles. The XPS spectrum at the binding energy of the Ti 2p-electrons (figure 2.2) closely matches the spectrum of bulk TiO_2 (anatase) having a $2p^{3/2}$ -electron binding energy of 458.5 eV (lowest binding energy peak). This implies that the core of the nanoparticles strongly resembles bulk TiO_2 . The signals of the Ti 2p electrons are somewhat broadened, likely due to the presence of slightly different types of Ti atoms. This is consistent with a large surface area. At the surface, the carboxylate groups impose a different chemical environment compared to the core of the TiO_2 particle, slightly changing the Ti 2p-electron binding energy.

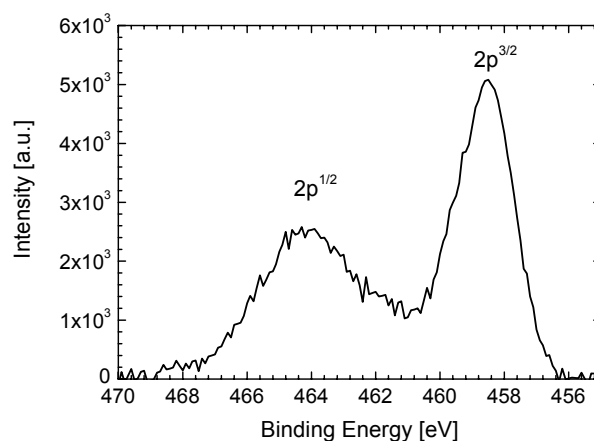


Figure 2.2 Photoelectron spectrum (XPS) of the Ti 2p binding energy region of purified stearate-coated TiO_2 nanoparticles.

Elemental analysis (combustion) indicates that the purified nanoparticles have an organic/inorganic ratio of 7:3, *i.e.* the mass of the stearate shell around the TiO₂ core forms 70% of the heterosupramolecular mass. Assuming a core size of 3 nm (see section ‘2.2.3 Size analysis’) and a core density of 3.8 g cm⁻³ (anatase), approximately 80 stearate molecules attach to one nanoparticle. FT-IR (ATR) spectroscopy revealed the type of bonding of the stearic acid to the TiO₂ surface. Figure 2.3 shows the FT-IR spectra of pure nanoparticles and of stearic acid. The C-H stretch vibrations of the alkyl chain of stearic acid can be observed in both spectra between 2850 and 2950 cm⁻¹. The spectrum of pure stearic acid shows the C=O stretch vibration at 1700 cm⁻¹. This band has completely been converted into three new bands in the spectrum of the stearic acid coated TiO₂ nanoparticles. The new bands at 1590, 1540, and 1445 cm⁻¹ originate from carboxylate binding to the TiO₂ surface.⁸ Two different carboxylate binding sites can be identified (see inset of figure 2.3); a bridging complex ($\nu_a = 1590$ cm⁻¹, $\nu_s = 1445$ cm⁻¹) and a bidentate complex ($\nu_a = 1540$ cm⁻¹, $\nu_s = 1445$ cm⁻¹).⁹

The FT-IR spectrum shows that complexation of the stearic acid to the nanoparticle is via a strong ionic/covalent bond. This ensures that the nanoparticles are soluble in organic solvents like chloroform and toluene. ¹H NMR spectroscopy of the purified nanoparticles in CDCl₃ revealed the presence of some propyl stearate, formed as byproduct during preparation. The absence of an absorption band at 1755 cm⁻¹ in the FT-IR spectrum, characteristic for this ester, demonstrates that propyl stearate is only a minor impurity.

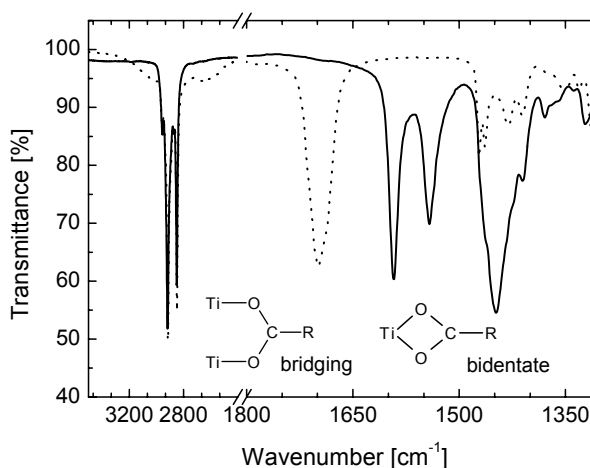


Figure 2.3 Solid-state ATR FT-IR spectra of stearic acid (dotted line) and purified stearate-coated TiO₂ nanoparticles (solid line). The inset shows the bridging and bidentate types of the carboxylate bonding to TiO₂, R = C₁₇H₃₅.

2.2.3 Size analysis

The size of the particles has been determined using a number of different techniques. For atomic force microscopy (AFM) a dilute solution of the purified nanoparticles in chloroform was drop cast on a freshly cleaned mica substrate. The height of the nanoparticles as determined from the AFM image, shown in figure 2.4, is approximately 2.5 nm; the diameter is 3-5 nm, after deconvolution with the AFM tip size. The diameter according to AFM is close to the average diameter of 3.2 nm that has been obtained from small angle X-ray scattering (SAXS) of the nanoparticles in solution.

Size exclusion chromatography (SEC) is commonly used to determine the molecular weight and molecular weight distribution of polymers. Because the stearate-coated TiO₂ particles are soluble in chloroform, SEC can be utilized to obtain information on the size distribution. Figure 2.6 displays the SEC traces of the purified nanoparticles in chloroform with UV detection at 254 nm. The polydispersity, $M_w/M_n = 1.06$, of the particles is very low. In a control experiment, the same SEC curve has been obtained for the “as prepared” nanoparticles, showing that precipitation has no significant effect on the size or size distribution. Based on SEC, monodisperse particles have been prepared. The apparent molecular weight relative to monodisperse polystyrene standards is 2600 g mol⁻¹. Under assumption of a polystyrene density of 1.047 g cm⁻³ the volume of the nanoparticles has been estimated to be 4.2 nm³ and the diameter approximately 2 nm.

Because the extension of the electronic wavefunctions of semiconductor quantum dots is confined to the particle, their energy levels are size-dependent and, in principle, UV-vis spectroscopy can be used to determine the diameter of semiconductor nanoparticles like TiO₂. The UV-vis spectra of the nanoparticles in chloroform solution show an onset of absorption at 316 nm, while in a drop cast film on quartz the onset is at 340 nm. In literature, there is some ambiguity on the exact relation between the onset of the UV absorption and the diameter of TiO₂ nanoparticles. According to Kotov, using an empirical model based on two UV curves and two TEM particle size diameters,^{6,10} an onset of 316 nm corresponds to a diameter of 1.8 nm, while 340 nm relates to 2 nm. According to Fitzmaurice,¹¹ applying a more theoretical model, 316 nm matches 1.4 nm in diameter and 340 nm implies a diameter of 1.7 nm. Because of the modest conformity of the two models and the uncertainty whether these results can be used for non-crystalline TiO₂, UV-vis cannot provide an accurate estimate of the

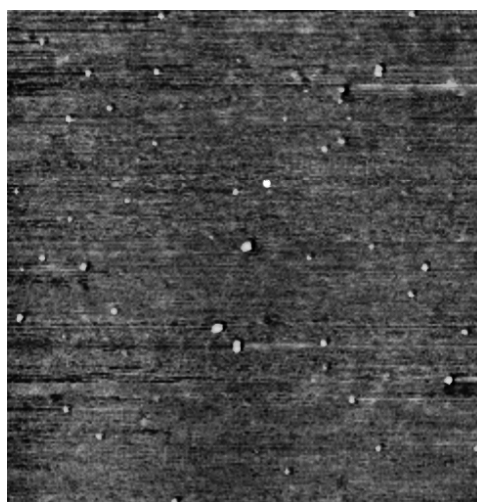


Figure 2.4 AFM tapping mode image of purified stearate-coated TiO₂ nanoparticles on a mica substrate. Image size is 2 × 2 μm.

size in the present case. Even so, the models and UV-vis spectra are consistent with the expectation that the core diameter is somewhat less than the total diameter as determined from AFM and SAXS. The maximum diameter of the core is 3 nm, as estimated from AFM and SAXS measurements.

2.3 Electron transfer in heterosupramolecular assemblies

2.3.1 Formation of heterosupramolecular assemblies

The formation of heterosupramolecular assemblies of a fluorescent π -conjugated oligomer and a TiO_2 nanoparticle is expected to result in a quenching of the photoluminescence due to electron transfer from the oligomer towards TiO_2 . The oligomer and the TiO_2 nanoparticle are linked using a carboxylic acid functional group. Accordingly, the photoluminescence of [2,2';5',2'']terthiophene-5-carboxylic acid (**1a**, T_3COOH , figure 2.5) in chloroform (6.85×10^{-6} M) is effectively quenched upon stepwise addition of a solution of 0.1 mg mL^{-1} TiO_2 nanoparticles in chloroform (figure 2.5). After addition of nanoparticles the absorption of free **1a** in chloroform at 379 nm has shifted slightly to 384 nm, due to complexation of the terthiophenecarboxylate to the TiO_2 surface.

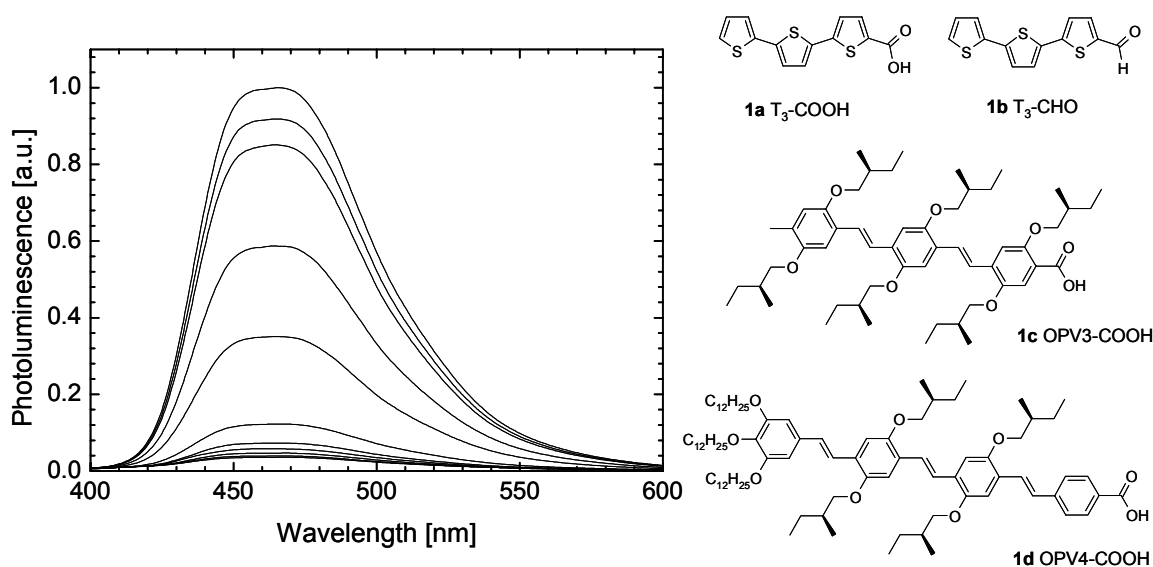


Figure 2.5 Photoluminescence of **1a** in chloroform upon addition of stearate-coated TiO_2 nanoparticles in chloroform. Excitation was at 381 nm; the data have been corrected for dilution effects. On the right the π -conjugated oligomers used in the formation of heterosupramolecular assemblies are shown.

The photoluminescence quenching strongly suggests that a complex between **1a** and the nanoparticle has formed, resulting in a heterosupramolecular assembly. SEC has been used to verify that the heterosupramolecular assembly has been formed. Comparison of the SEC traces of the pure nanoparticles (0.05 mg mL^{-1}) and of a mixture of nanoparticles (0.05 mg mL^{-1}) and **1a** (1.7×10^{-5} M) reveals that adsorption of **1a** onto the nanoparticles results in a small increase of the elution time (from 8.31 to 8.36 min., figure 2.6). To confirm the binding of **1a**, the experiment is repeated with UV

detection at 360 nm, where **1a** absorbs but the nanoparticles are transparent. The inset of figure 2.6 shows that the detection at 360 nm gives a signal at exactly the same retention time (8.36 min.) compared to the nanoparticles measured at 254 nm, while untreated nanoparticles give no signal at 360 nm. This is unambiguous proof of the binding of **1a** to the TiO₂ nanoparticles in chloroform solution.

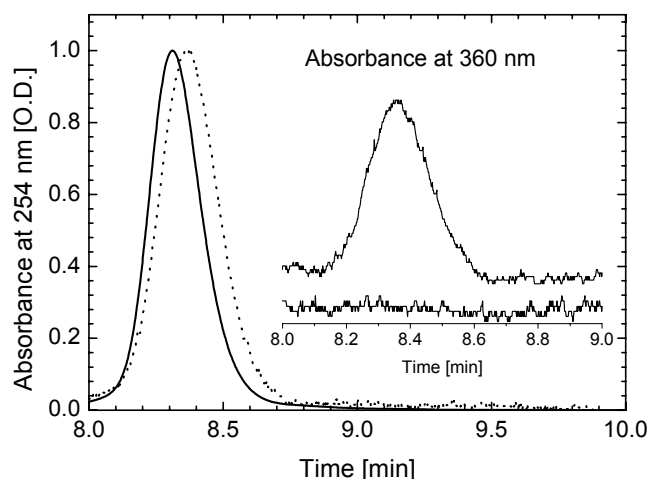


Figure 2.6 Size exclusion chromatogram (SEC) recorded at 254 nm, of stearate-coated TiO₂ nanoparticles. Dotted curve is the SEC of T₃COO-TiO₂ heterosupramolecular assemblies. The inset shows the chromatogram detected at 360 nm of stearate-coated TiO₂ nanoparticles (lower curve) and T₃COO-TiO₂ heterosupramolecular assemblies (upper curve).

The small increase of the SEC elution time of the nanoparticle after **1a** adsorption can be explained if the binding of the **1a** with the nanoparticle involves the replacement of a stearate group on the surface of the nanoparticle following the equilibrium:



In this reaction, the long alkyl chain of C₁₇H₃₅COOH is replaced by the somewhat smaller terthiophene. This leads to a reduction of the hydrodynamic diameter, and might explain the small increase of the SEC elution time.

Based on an estimated value of 3 nm for the diameter of the TiO₂ core, the ratio of **1a** to nanoparticle is approximately 20:1 at the end of the quenching experiment. Hence, about twenty molecules of **1a** can be attached to the nanoparticle. As some photoluminescence is left, it seems that there is an equilibrium between the adsorbed and free **1a** in this experiment. The presence of this equilibrium has been confirmed by the observed increase of photoluminescence when some stearic acid is added to T₃COO-TiO₂ and has been supported by the time-resolved photoluminescence experiments described in section 2.3.2.

2.3.2 Static photoluminescence quenching by photoinduced electron transfer

Time-correlated single photon counting luminescence studies have been performed to determine the origin of the quenching in more detail. In the photoluminescence experiment (figure 2.5), the quenching does not go to completion and a small amount of photoluminescence remains. In order to establish the lifetime of the residual photoluminescence, the quenching experiment has been repeated, monitoring the temporal evolution of the photoluminescence intensity, (figure 2.7a). These time-resolved experiments reveal that the photoluminescence lifetime remains constant at approximately 230 ps during the whole experiment. This indicates that the residual photoluminescence originates from free **1a** in solution, *i.e.* not bonded to a TiO₂ particle.

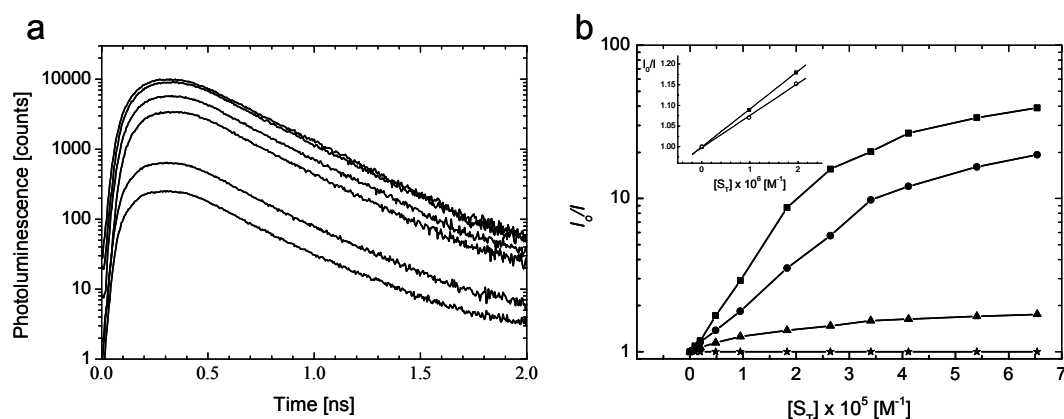


Figure 2.7 a) Time-resolved photoluminescence of **1a** in chloroform displaying the effect of the addition of stearate-coated TiO₂ nanoparticles. Excitation was at 400 nm; the data have been corrected for dilution effects. b) Stern-Volmer plots showing the quenching factor I_0/I for different oligomers versus the total concentration of the stearate tails: **1a** in chloroform (■); **1a** in toluene (●); **1b** and **1c** in chloroform (★) and **1d** in chloroform (▲). The inset shows the linear fits of the initial slope, used for determining the binding constants K_S for **1a** finding $K_S = 9.2 \times 10^4 \text{ L mol}^{-1}$ in chloroform and $K_S = 7.8 \times 10^4 \text{ L mol}^{-1}$ in toluene.

The result shown in figure 2.7a is in accordance with a static quenching mechanism rather than a dynamic (collisional) quenching: **1a** connected to the nanoparticle is non-fluorescent and non-bonded **1a** is the only source of the photoluminescence. The static quenching is attributed to a photoinduced electron transfer from the terthiophene moiety to the TiO₂ nanoparticle. Energy transfer is less likely to be involved in the quenching because the band gap of terthiophene (3.0 eV) is significantly less than the band gap of TiO₂ nanoparticles (3.6-3.7 eV) and, hence, energy transfer to TiO₂ is endergonic. The ratio of integrated photoluminescence intensities before (I_0) and after (I) addition of TiO₂, also referred to as the quenching factor, can be used to determine a lower limit for the rate constant of charge transfer (k_{CT}) using the luminescence lifetime of **1a** ($\tau = 230 \text{ ps}$) via:

$$k_{CT} \geq \frac{(I_0/I) - 1}{\tau} \quad (2)$$

Because the photoluminescence quenching has been limited by free **1a** present in the solution rather than by the competition between electron transfer and radiative decay of T₃COO-TiO₂, the actual charge separation rate is likely to be significantly higher than the result, $k_{CT} \geq 1.7 \times 10^{11} \text{ s}^{-1}$. The actual value may be comparable to, or higher than the high k_{CT} values ($10^{12} - 10^{13} \text{ s}^{-1}$) reported for Ru^{II} dye sensitizer molecules on nanocrystalline TiO₂, measured in alcoholic media¹².

The conclusion that dynamic quenching is a minor process has been supported by the fact that no photoluminescence quenching is observed when **1a** is replaced by an aldehyde-functionalized terthiophene (**1b**, T₃CHO, figure 2.5). The aldehyde of **1b** lacks the binding tendency associated with the carboxyl group of T₃COOH and, hence, **1b** can only give dynamic (collisional) quenching. These quenching experiments have been summarized in figure 2.7b, where the quenching factor I_0/I is plotted versus the total concentration in solution of the stearate chains on the nanoparticle surface (calculated using the results of the elemental analysis). It is reasonable to assume that the stearate adsorption sites are the active sites on the surface, where the reaction takes place. According to the Stern-Volmer equation for static quenching, the initial slope of the curve in figure 2.7b can be related to the binding constant for the terthiophene-nanoparticle complex:

$$\frac{I_0}{I} = 1 + K_S [\text{C}_{17}\text{H}_{35}\text{COO} - \text{TiO}_2] \quad (3)$$

Where $[\text{C}_{17}\text{H}_{35}\text{COO} - \text{TiO}_2]$ is the concentration in solution of stearate chains present on the nanoparticles. This concentration is unknown but can be approximated by the total concentration of the stearate in solution and on the surface $[S_T]$, which was calculated using the results from the elemental analysis. As only a minor amount of the stearate tails are removed initially, K_S can be approximated from the initial slope of the Stern-Volmer plot. The binding constant K_S is defined as:

$$K_S = \frac{[\text{T}_3\text{COO} - \text{TiO}_2]}{[\text{T}_3\text{COOH}][S_T]} \quad (4)$$

From the curves for chloroform and toluene (see inset in figure 2.7b) an average binding constant $K_S = 8.5 \times 10^4 \text{ L mol}^{-1}$ is obtained.

The photoluminescence quenching experiment performed on **1a** in chloroform, has also been performed in toluene to investigate the effect of the nature of the solvent. Again, a significant quenching is observed, which reveals that the electron transfer even occurs in apolar solvents as toluene. The Stern-Volmer plot (figure 2.7b) shows that the quenching in toluene is less effective than in chloroform. The difference between chloroform and toluene at higher quenching factors has been explained by the equilibrium shown in equation (1). Although not investigated in detail, it is likely that the substitution of stearic acid by **1a** is less favorable in toluene, because stearic acid is insoluble in toluene.

2.3.3 Structure of the oligomer used in a heterosupramolecule

The strong difference in quenching observed between the acid (**1a**) and the aldehyde (**1b**) of terthiophene suggests that a functional group with strong binding to the TiO₂ particles, such as a carboxylic acid, is required. Subsequently two other π -conjugated carboxylic acid functionalized oligomers (figure 2.5) have been tested for binding to the stearic acid TiO₂ nanoparticles. Surprisingly, no photoluminescence quenching has been observed for **1c** (OPV3-COOH), while some quenching could be established for **1d** (OPV4-COOH). The maximum quenching factor obtained with **1d** of $I_0/I = 1.8$ is, however, much less than observed for **1a**. The electronic properties (oxidation potentials and excited state energies) of **1c** and **1d** are similar to those of **1a** and unlikely cause this dramatic difference. Therefore, the remarkable dependence of photoluminescence quenching on the structure of the oligomer is tentatively attributed to the steric hindrance imparted by the solubilizing side chains of **1c** and **1d**. The spatial requirements of these oligomers to enter the stearic acid shell of the nanoparticles seem to inhibit the formation of the heterosupramolecular assembly.

2.4 Spacer length dependence of photoinduced electron transfer in heterosupramolecules

To determine the distance dependence for the rate of charge transfer, photoinduced electron transfer has been studied in a homologous series of heterosupramolecules consisting of terthiophene units connected to a TiO₂ nanoparticle via saturated spacers of different length.

2.4.1 Distance dependence of charge transfer rate constants in the nonadiabatic weak-coupling regime

When a saturated spacer is placed in between the terthiophene moiety and the TiO₂ nanoparticle, the charge transfer is expected to occur in the nonadiabatic, weak-coupling regime.¹³ In this regime it is generally assumed that the rate constant for charge transfer k_{CT} decreases exponentially with the distance $R-R_0$ between the donor and acceptor, or by the number of sigma bonds σ in the saturated spacer:

$$\begin{aligned} \ln k_{CT} &= \ln k_0 - \beta'(R - R_0) \quad \text{and} \\ \ln k_{CT} &= \ln k_0 - \beta\sigma \end{aligned} \quad (5)$$

Here β and β' are the attenuation coefficients accounting for the distance dependence of the charge transfer rate constant. Typical values for β over saturated spacers are found to be approximately 1 per bond.^{13,14}

The distance dependence of the photoinduced electron transfer has been studied for dye molecules adsorbed on nanocrystalline TiO₂ thin films. For example, femtosecond mid-IR spectroscopy has revealed that for Ru(dcbpy)₂(NCS)₂ (dcbpy = 4,4'-dicarboxy-2,2'-bipyridine), which had directly been coupled to TiO₂, charge transfer is extremely fast (≤ 100 fs, $k_{CT} \geq 1 \times 10^{13}$ s⁻¹).¹⁵ Modification of

these dyes with a spacer allows to study the rate constant for charge transfer at longer distances.^{16,17} Insertion of $(\text{CH}_2)_n$ spacers between the bipyridine and carboxy groups of $\text{Re}(\text{CO})_3\text{Cl}(\text{dcbpy})$ ¹⁶ reveals that charge transfer for $n = 0$ (no spacer) occurs in the adiabatic region (strong electronic coupling), and results in an injection time of less than 100 fs. For $n = 1$ and 3, however, the electronic coupling is reduced significantly, and consequently injection times are longer, 19 and 240 ps, in qualitative agreement with the trend predicted for nonadiabatic charge transfer. Rapid ($k_{\text{CT}} > 10^8 \text{ s}^{-1}$) long distance (18 Å) electron transfer across a molecule-nanocrystalline semiconductor interface has been observed for rigid ruthenium dye tripods with a fixed distance between the Ru atom and the surface.¹⁷ The distance dependence of the charge recombination in dye-sensitized nanocrystalline TiO_2 films has been studied lately.¹⁸ A strong correlation has been observed between the recombination dynamics and the spatial separation, with an exponential dependence of the recombination half-time and the distance.^{18c}

2.4.2 Heterosupramolecular assemblies with carboxylic acid linkers

Replacement of stearate molecules as shown in equation 1 by other molecules is possible provided they contain an acidic or similar functional group with affinity for the TiO_2 surface. Because complexation of the carboxylic acid functionality in **1a** to the TiO_2 nanoparticle seems sufficient, the first expansion of the homologues series was tested introducing a simple $(\text{CH}_2)_4$ bridge between the terthiophene and the carboxylic acid functional group, see molecule **2**, figure 2.8a.

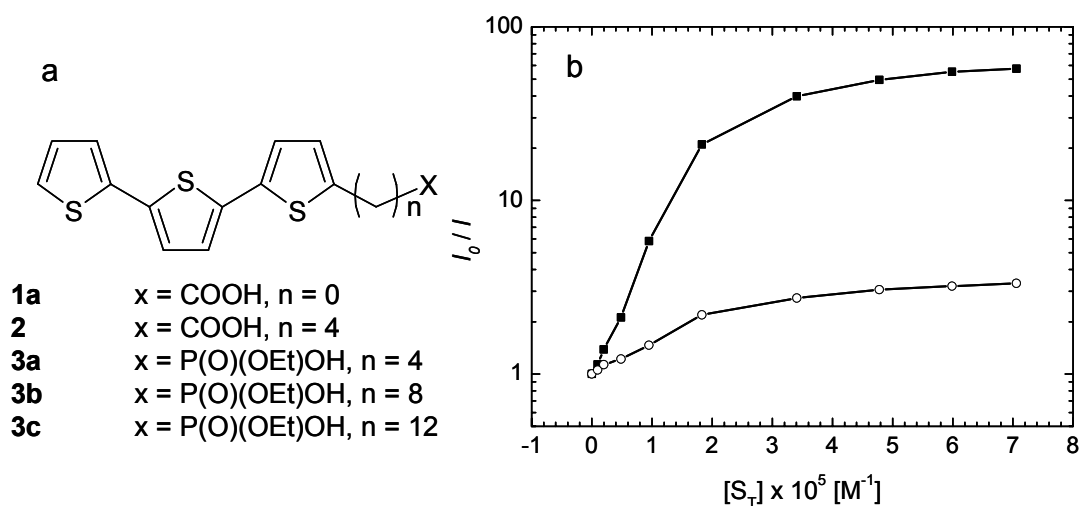
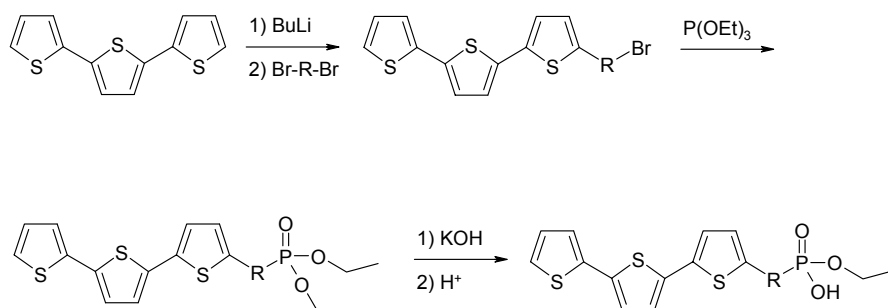


Figure 2.8 a) Molecular structures of **1a**, **2**, and **3a-c**. b) Stern-Volmer plot of the photoluminescence quenching (I_0/I) of **1a** (■) and **2** (○) in chloroform plotted as function of concentration of stearate molecules present on the surface. The lifetime of the residual photoluminescence was monitored during the experiments and remained constant.

[2,2':5',2''-Terthiophene]-5-pentanoic acid (**2**) having a flexible butyl spacer between the T₃ and COOH moieties was prepared analogous to published methods from the corresponding bromobutylterthiophene via nucleophilic substitution with KCN and hydrolysis of the nitrile under basic conditions.^{19,20} A Stern-Volmer plot (figure 2.8b) of the photoluminescence quenching of **1a** (T₃COOH) and **2** as function of the total concentration of stearate molecules on the nanoparticle surface (approximating the number of available adsorption sites) shows that high quenching values can be reached for **1a**, while for **2** the ratio I_0/I does not exceed a value of 3.5. A reduction of the electron transfer rate as consequence of the increased distance seems a likely explanation for this observation. However, the observed photoluminescence lifetimes of both **1a** and **2** do not decrease when TiO₂ nanoparticles are added. This indicates that the residual photoluminescence mainly originates from non-bonded molecules, as stated in section 2.3.2. Hence, the lower photoluminescence quenching of **2** compared to **1a** is most likely due to a lower amount of **2** bound to the TiO₂ nanoparticles. For a strong interaction, the stearate chains covering the nanoparticle surface must be replaced. The aromatic carboxylic acid ($pK_a \sim 3.5$) in **1a** is more effective because it is a stronger acid than the aliphatic acid of **2**, which has a pK_a value of ~ 5 , similar to stearic acid.

2.4.3 Heterosupramolecular assemblies with phosphonic acid linkers

To overcome weak complex formation a stronger anchoring group must be used. Phosphonic acids have been reported to be stronger anchoring groups for TiO₂ nanocrystals²¹. Phosphonic acid monoethyl esters ($pK_a \sim 2.5$) are also likely stronger anchoring groups. Therefore three different molecules with a butyl (**3a**), octyl (**3b**), and dodecyl (**3c**) spacer between the phosphonic acid linker and the fluorescent terthiophene unit have been prepared (figure 2.8a). The synthesis of **3a-3c** is outlined in Scheme 2.1. Lithiated terthiophene was reacted with the appropriate 1, ω -dibromo-*n*-alkane to form the ω -bromoalkylterthiophene. The corresponding phosphonic acid diethyl esters were obtained in an Arbuzov reaction with triethyl phosphite and converted to the phosphonic acid monoethyl ester by mild alkaline treatment and protonation. Although the phosphonic acid can be fully hydrolyzed under acidic conditions, most acid treatments turned out to be destructive for the terthiophene moiety and did not give quantitative conversion. Compounds **3a-3c** were characterized with NMR and elemental analysis.



Scheme 2.1 : Synthetic route towards phosphonic acid monoethyl ester derivatives of terthiophene. R = (CH₂)_n for **3a** n = 4 for **3b** n = 8, and for **3c** n = 12.

The photoluminescence quenching of **3a**, **3b**, and **3c** in chloroform solution has been measured with stepwise addition of stearate-coated TiO₂ nanoparticles (figure 2.9). For each molecule, the photoluminescence quenching reaches a limiting value and subsequent addition of TiO₂ nanoparticles does not further decrease the photoluminescence intensity. This limit suggests that virtually all molecules are adsorbed on the TiO₂ surface. Adsorption on TiO₂ seems equally effective for the three probe molecules, because the limiting quenching is reached at the same TiO₂ concentration. As expected, the phosphonic acid monoesters are more effective in forming heterosupramolecules than carboxylic acids, because this limit is not reached for **1a** (T₃COOH), even when 10 times more TiO₂ nanoparticles are added. In accordance with this result, the photoluminescence lifetime of **3a-3c** is decreased (figure 2.10a) in contrast to that of **1a**, suggesting that the majority of **3a-3c** is connected to the nanoparticle. The dominant lifetimes in a biexponential fit of the curves in figure 2.10a are $\tau = 22$ (**3a**), 123 (**3b**), and 180 ps (**3c**).

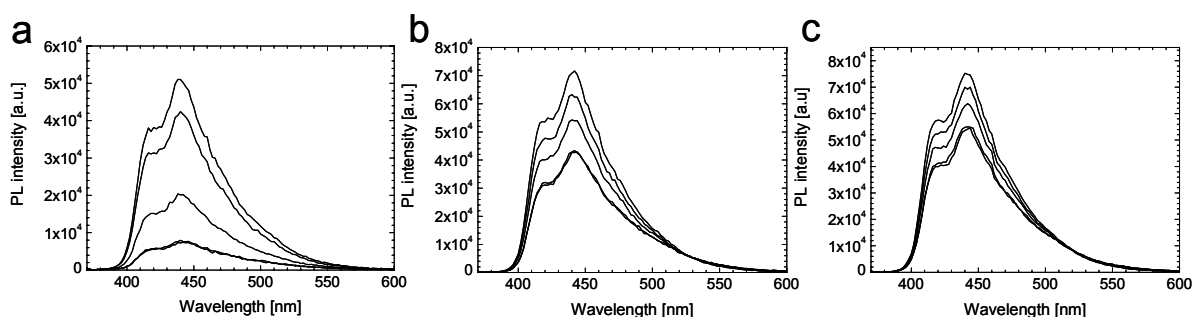


Figure 2.9 Photoluminescence quenching of **3a** (a), **3b** (b), and **3c** (c) in chloroform (7×10^{-6} M) upon addition of TiO₂ nanoparticles. The excitation wavelength is 360 nm. The top curves in each panel represent the photoluminescence without quencher and subsequent curves are measured after addition of 1×10^{-6} , 2×10^{-6} , 5×10^{-6} , 1×10^{-5} , and 2×10^{-5} g of TiO₂ nanoparticles.

The residual photoluminescence of **3a-3c** (figure 2.9) is more intense for the longer spacers. This indicates that the rate for charge transfer decreases with increasing distance between the terthiophene and the TiO₂ nanoparticle surface. The rate constants for charge transfer have been determined from

the quenching factor (I_0/I) and the intrinsic photoluminescence lifetime ($\tau_\infty = 200$ ps) (Table 2.1). The data reveal that the process remains fast, even for a long saturated linker of thirteen carbon-carbon bonds. Table 1 also shows the results for experiments in toluene, where a slightly higher rate constant has been found. The rate constants obtained from the photoluminescence quenching corroborate qualitatively with the rate constants that are obtained from the photoluminescence lifetime $k'_{CT} = (1/\tau - 1/\tau_\infty)$ (Table 2.1). The charge transfer rates in these heterosupramolecules are similar to those found by Oevering *et al.* in molecular donor-bridge-acceptor dyads having similar distances between the donor and acceptor groups, but with rigid nonconjugated spacers.²² For these rigid saturated bridges k_{CT} decreases from $> 10^{11}$ s⁻¹ for a four-bond separation, via $\sim 4 \times 10^{10}$ s⁻¹ for an eighth-bond spacer, to $\sim 4 \times 10^8$ s⁻¹ for a twelve-bond spacer. Interestingly, fast electron transfer (10^9 s⁻¹) has also been observed across 2-3 nm thick monolayers of fatty acids in Langmuir-Blodgett films, where the alkyl chain has a stretched conformation.²³ The stretched conformation optimizes the through-bond electronic coupling.²⁴

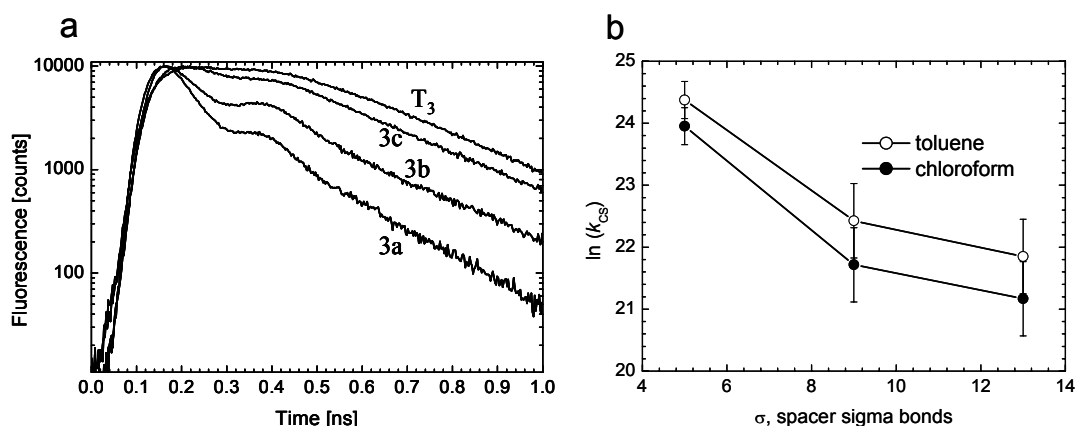


Figure 2.10 a) Time-resolved photoluminescence recorded at 440 nm with excitation at 400 nm for **3a-3c** with TiO₂ added to achieve maximum photoluminescence quenching. For comparison the photoluminescence trace of free terthiophene (T₃) is also shown. The bump around 0.4 ns is an experimental artefact. b) Spacer length dependence of the electron transfer rate constant in **3a-3c** TiO₂ conjugates in chloroform (●) and toluene (○) plotted as function of the number of sigma bonds in the spacer.

Table 2.1 Photoluminescence quenching factors (I_0/I) and rate constants for charge transfer (k_{CT}) obtained from photoluminescence quenching (k_{CT}) and lifetime reduction (k'_{CT}) of heterosupramolecules of **3a-3c** and TiO₂ nanoparticles.

compound	solvent	I_0/I	k_{CT} (s ⁻¹)	k'_{CT} (s ⁻¹)
3a	chloroform	6.06	2.5×10^{10}	4.0×10^{10}
	toluene	8.71	3.9×10^{10}	
3b	chloroform	1.54	2.7×10^9	3.1×10^9
	toluene	2.10	5.5×10^9	
3c	chloroform	1.31	1.6×10^9	0.6×10^9
	toluene	1.62	3.1×10^9	

The experimental rate constants do not exhibit a linear relation with spacer length in a semi-logarithmic plot (figure 2.10). The plot suggests that $0.3 < \beta < 0.6$ per bond, *i.e.* somewhat less than values of $0.8 < \beta < 1.0$ established for various saturated spacers.¹³ The β value is somewhat smaller than $\beta = 0.98$ found by Oevering *et al.* for a rigid spacer.²² The deviation from a linear relation is possibly due to the flexibility of the spacer. For a flexible spacer there is no simple relation between the actual distance between the chromophores and the number of sigma bonds when back folding occurs. In this event, k_{CT} may be enhanced, although such enhancement is not expected when the electronic coupling is strictly through bond. Another explanation may lie in an enhancing effect of proximate alkyl chains present on the TiO₂ surface. These so-called interrelay constructive interference effects as discussed by Paddon-Row and Shephard might explain the lower β values found in hole and electron transfer experiments across monolayer assemblies.²⁵ At the end of the titration experiment shown in figure 2.9, the ratio of terthiophene unit to TiO₂ nanoparticle (3 nm) is approximately 200:1, illustrating an almost full surface coverage. From photoluminescence and UV-vis absorption spectroscopy, no indication of stacks of T₃ units is apparent, eliminating this as contributing to the observed photoluminescence quenching. Mutual interferences between the terthiophene moieties will give rise to the non-linear relation as observed, backfolding in such a dense monolayer is not likely but interrelay effects are still possible and a likely explanation for the observed deviation from linearity.

2.5 Conclusions

Nanosized TiO₂ particles have been prepared by arrested hydrolysis. The nanoparticles consist of a TiO₂ core of approximately 2-3 nm in diameter, surrounded by a shell of stearate tails connected to the TiO₂ surface via the carboxylate group, involving bridging and bidentate binding sites. The strong binding of the stearate shell prevents aggregation and renders the nanoparticles soluble in common apolar organic solvents. In solution, the nanoparticles can form heterosupramolecular assemblies in the presence of π -conjugated oligomers containing a carboxylic acid functional group. The binding of T₃COOH to the TiO₂ nanoparticle results in quenching of the photoluminescence. According to time-resolved photoluminescence, the quenching is static and due to a photoinduced electron transfer from the terthiophene moiety to TiO₂. In chloroform, the rate constant for charge separation is larger than $1.7 \times 10^{11} \text{ s}^{-1}$. This is the first time that interactions between π -conjugated oligomers and inorganic nanoparticles have been studied in solution. Charge transfer in organic solvents appear extremely fast even compared to the high rates observed for electron injection from Ru-dyes into TiO₂ in polar media.

Heterosupramolecular assemblies of terthiophene moieties and TiO₂ nanoparticles, linked by alkyl spacers of different length have been constructed using phosphonic acid monoethyl esters as surface-anchoring group. The rate for charge transfer from the photoexcited terthiophene to TiO₂ has been studied by monitoring the changes in the competing photoluminescence decay. Never before, electron transfer over a saturated spacer from a π -conjugated oligomer to a TiO₂ nanoparticle has been measured in solution. Elongation of the spacer lowers the charge transfer rate as expected, but the attenuation per bond is less than expected. Based on a simple exponential decay of the rate with the length of the spacer, the electron transfer over long saturated spacers is higher than expected. It is quite remarkable that high rates over such distances can be observed in apolar organic media.

2.6 Experimental

General. ¹H-NMR spectra were recorded on a Varian Gemini spectrometer at a frequency of 300.08 MHz and a Varian Mercury spectrometer at 400.16 MHz. Deuterated solvents were used with tetramethylsilane (TMS) as an internal standard. Elemental analyses were performed on a Perkin Elmer 2400 series II CHN Analyzer.

Preparation of TiO₂ nanoparticles.⁶ Arrested hydrolysis of titanium(IV) isopropoxide (95 μL , 0.32 mmol) (Acros, > 98%) in anhydrous chloroform (100 mL) containing 5 vol.-% anhydrous 1-propanol and doubly distilled water (15 μL , 0.83 mmol) in the presence of stearic acid (88 mg, 0.31 mmol) (Merck, > 97%), afforded TiO₂ nanoparticles. After stirring for a few days, the resulting solution was

colorless, nonscattering, and stable for at least 6 months. The nanoparticles were purified by precipitation, by adding acetonitrile to the solution. After filtering and drying in air, the resulting white powder could be redissolved in solvents like chloroform and toluene.

5-(4-Bromobutyl)-2,2':5',2''-terthiophene. To a solution of 2,2':5',2''-terthiophene (1 g, 4 mmol) in THF (30 mL) at $-78\text{ }^{\circ}\text{C}$ under argon atmosphere, *n*-butyllithium in hexane (2.8 mL, 1.6 mol L^{-1} , 4.4 mmol) was slowly added. The solution was stirred for 10 min. at $-78\text{ }^{\circ}\text{C}$ and subsequently allowed to warm to room temperature. In a separate flask, a solution of 1,4-dibromobutane (5.22 g, 36 mmol) in THF (40 mL) was heated to $50\text{ }^{\circ}\text{C}$. The lithiated terthiophene was slowly added to the 1,4-dibromobutane solution with the use of a canule under clean argon flow, and stirred for 2 h at $50\text{ }^{\circ}\text{C}$. The reaction mixture was then washed with aqueous ammonium chloride (100 mL). The product was extracted with dichloromethane, washed with water, and dried over MgSO_4 . The excess of 1,4-dibromobutane was removed under reduced pressure (0.5 mbar, $70\text{ }^{\circ}\text{C}$). The crude product was purified using column chromatography, using a silica support and 4 vol.-% dichloromethane in hexane as eluent, yielding 0.64 g (42%) of $\text{T}_3(\text{CH}_2)_4\text{Br}$. $^1\text{H-NMR}$ (CDCl_3): δ 1.85 (m, 2H), 1.95 (m, 2H), 2.82 (t, 2H), 3.42 (t, 2H), 6.7 (dt, $^3J = 1.8\text{ Hz}$, $^4J = 0.1\text{ Hz}$, 1H), 6.98 (d, $^3J = 3.7\text{ Hz}$, 1H), 7.0 (d, $^3J = 3.7\text{ Hz}$, 1H), 7.02 (dd, $^3J = 4.8\text{ Hz}$, $^3J = 3.5\text{ Hz}$, 1H), 7.06 (d, $^3J = 4.0\text{ Hz}$, 1H), 7.16 (dd, $^3J = 3.5\text{ Hz}$, $^4J = 1\text{ Hz}$, 1H), 7.21 (dd, $^3J = 4.8\text{ Hz}$, $^4J = 1\text{ Hz}$, 1H).

5-(8-Bromooctyl)-2,2':5',2''-terthiophene. $\text{T}_3(\text{CH}_2)_8\text{Br}$ was prepared following the procedure described for 5-(4-bromobutyl)-[2,2':5',2'']terthiophene using 1,8-dibromooctane instead of 1,4-dibromobutane. $^1\text{H-NMR}$ (CDCl_3): δ 1.25-1.45 (m, 8H), 1.67 (m, 2H), 1.85 (m, 2H), 2.80 (t, 2H), 3.40 (t, 2H), 6.68 (dt, $^3J = 1.8\text{ Hz}$, $^4J = 0.1\text{ Hz}$, 1H), 6.98 (d, $^3J = 3.7\text{ Hz}$, 1H), 6.98 (d, $^3J = 3.7\text{ Hz}$, 1H), 7.0 (dd, $^3J = 4.8\text{ Hz}$, $^3J = 3.5\text{ Hz}$, 1H), 7.04 (d, $^3J = 4.0\text{ Hz}$, 1H), 7.14 (dd, $^3J = 3.5\text{ Hz}$, $^4J = 1\text{ Hz}$, 1H), 7.20 (dd, $^3J = 4.8\text{ Hz}$, $^4J = 1\text{ Hz}$, 1H).

5-(12-Bromododecyl)-2,2':5',2''-terthiophene. $\text{T}_3(\text{CH}_2)_{12}\text{Br}$ was prepared following the procedure described for 5-(4-bromobutyl)-[2,2':5',2'']terthiophene using 1,12-dibromododecane instead of 1,4-dibromobutane. $^1\text{H-NMR}$ (CDCl_3): δ 1.25-1.45 (m, 16H), 1.68 (m, 2H), 1.85 (m, 2H), 2.80 (t, 2H), 3.40 (t, 2H), 6.68 (dt, $^3J = 1.8\text{ Hz}$, $^4J = 0.1\text{ Hz}$, 1H), 6.98 (d, $^3J = 3.7\text{ Hz}$, 1H), 6.98 (d, $^3J = 3.7\text{ Hz}$, 1H), 7.0 (dd, $^3J = 4.8\text{ Hz}$, $^3J = 3.5\text{ Hz}$, 1H), 7.04 (d, $^3J = 4.0\text{ Hz}$, 1H), 7.14 (dd, $^3J = 3.5\text{ Hz}$, $^4J = 1\text{ Hz}$, 1H), 7.20 (dd, $^3J = 4.8\text{ Hz}$, $^4J = 1\text{ Hz}$, 1H).

[2,2':5',2''-Terthiophene]-5-pentanoic acid (2). 5-(4-Bromobutyl)-2,2':5',2''-terthiophene (0.57 g, 1.5 mmol) in DMF (50 mL) was added to a dispersion of KCN (0.2 g, 3 mmol) in DMF (50 mL) at 90 °C, in 45 min. Subsequently the reaction mixture is kept at 90 °C for another 15 min. Workup is performed by slow addition to water under argon flow. The crude product is extracted with dichloromethane, washed with concentrated NaCl solution, and dried over MgSO₄, yielding 0.45 g (92%) T₃(CH₂)₄CN. T₃(CH₂)₄CN was then dissolved in a water:ethanol mixture (v:v = 1:3, 200 mL) containing KOH (2 g) and hydrolyzed under reflux for 3 days. After removal of ethanol the reaction mixture was added to THF and concentrated HCl was added until pH = 1. After removal of THF, the product was dissolved in dichloromethane, washed with dilute HCl, and dried over MgSO₄. Recrystallization from dichloromethane:hexane (v:v = 1:1) yielded 0.233 g (50%) of **3**. ¹H-NMR (CDCl₃): δ 1.75 (m, 4H), 2.40 (t, 2H), 2.8 (t, 2H), 6.7 (dt, ³J = 1.8 Hz, ⁴J = 0.1 Hz, 1H), 6.98 (d, ³J = 3.7 Hz, 1H), 7.0 (d, ³J = 3.7 Hz, 1H), 7.02 (dd, ³J = 4.8 Hz, ³J = 3.5 Hz, 1H), 7.06 (d, ³J = 4.0 Hz, 1H), 7.16 (dd, ³J = 3.5 Hz, ⁴J = 1 Hz, 1H), 7.21 (dd, ³J = 4.8 Hz, ⁴J = 1 Hz, 1H).

(4-[2,2':5',2''-Terthiophen]-5-ylbutyl)-phosphonic acid monoethyl ester (3a). 5-(4-Bromobutyl)-2,2':5',2''-terthiophene (0.3 g, 0.8 mmol) was dissolved in triethyl phosphite (30 mL) and reacted for 20 h at 150 °C. After the reaction, triethyl phosphite was removed by distillation. Conversion to the phosphonic diethyl ester was quantitative. ¹H-NMR (CDCl₃): δ 1.25 (t, 6H), 1.6-1.8 (m, 6H), 2.75 (t, 2H), 4.0 (m, 4H), 6.7 (dt, ³J = 1.8 Hz, ⁴J = 0.1 Hz, 1H), 6.98 (d, ³J = 3.7 Hz, 1H), 7.0 (d, ³J = 3.7 Hz, 1H), 7.02 (dd, ³J = 4.8 Hz, ³J = 3.5 Hz, 1H), 7.06 (d, ³J = 4.0 Hz, 1H), 7.16 (dd, ³J = 3.5 Hz, ⁴J = 1 Hz, 1H), 7.21 (dd, ³J = 4.8 Hz, ⁴J = 1 Hz, 1H). Conversion of the diethyl ester to the monoethyl phosphonic acid was achieved by hydrolysis in a mixture of water (30 mL) and ethanol (50 mL) containing KOH (1 g) maintained at reflux for 2 days. Workup was performed by dilution with water (100 mL) and removal of the ethanol by evaporation. The crude potassium salt was water-soluble. By addition of concentrated HCl (20 mL) the acid precipitates and can be extracted with dichloromethane. The dichloromethane phase was washed with water, and dried over a small amount of Na₂SO₄. ¹H-NMR revealed the presence of up to 10% of a side product, T₃(CH₂)₄OH (¹H-NMR, CH₂-OH t δ 3.62 ppm). This side product was successfully removed by dissolving the crude product in chloroform and extraction with K₂CO₃ into water. After washing with chloroform, the water phase was acidified and the purified product extracted in chloroform and dried over Na₂SO₄, yielding 0.275 g (85%) of **3a**. Further purification was performed by recrystallization from chloroform:hexane (v:v = 5:95). ¹H-NMR (CDCl₃): δ 1.25 (t, 3H), 1.6-1.8 (m, 6H), 2.75 (t, 2H), 4.0 (m, 2H), 6.7 (dt, ³J = 1.8 Hz, ⁴J = 0.1 Hz, 1H), 6.98 (d, ³J = 3.7 Hz, 1H), 7.0 (d, ³J = 3.7 Hz, 1H), 7.02 (dd, ³J = 4.8 Hz, ³J = 3.5 Hz, 1H), 7.06 (d, ³J = 4.0 Hz, 1H), 7.16 (dd, ³J = 3.5 Hz, ⁴J = 1 Hz, 1H), 7.21 (dd, ³J = 4.8 Hz, ⁴J = 1

Hz, 1H). Elemental analysis: Calculated for $C_{18}H_{21}O_3PS_3$: 52.65% C, 4.96% H; Found: 52.41% C, 5.13% H.

(8-[2,2':5',2''-Terthiophen]-5-yloctyl)-phosphonic acid monoethyl ester (3b). Following the procedure for the preparation of **3a**, **3b** was prepared from 5-(8-bromooctyl)-2,2':5',2''-terthiophene. After hydrolysis of the phosphonic diethyl ester a side product appeared, which was removed as described in the procedure for **3a**. **3b**: 1H -NMR ($CDCl_3$): δ 1.2-1.4 (m, 11H), 1.5-1.8 (m, 6H), 2.75 (t, 2H), 4.1 (m, 2H), 6.7 (dt, $^3J = 1.8$ Hz, $^4J = 0.1$ Hz, 1H), 6.98 (d, $^3J = 3.7$ Hz, 1H), 7.0 (d, $^3J = 3.7$ Hz, 1H), 7.02 (dd, $^3J = 4.8$ Hz, $^3J = 3.5$ Hz, 1H), 7.06 (d, $^3J = 4.0$ Hz, 1H), 7.16 (dd, $^3J = 3.5$ Hz, $^4J = 1$ Hz, 1H), 7.21 (dd, $^3J = 4.8$ Hz, $^4J = 1$ Hz, 1H). Elemental analysis: Calculated for $C_{22}H_{29}O_3PS_3$: 56.20% C, 6.08% H; Found: 56.39% C, 6.24% H.

(12-[2,2':5',2''-Terthiophen]-5-ylododecyl)-phosphonic acid monoethyl ester (3c). Following the procedure for the preparation of **3a**, **3b** was prepared from 5-(12-bromododecyl)-2,2':5',2''-terthiophene. For **3c** removal of the side product, in the same manner as for **3a**, was not possible because the potassium salt of **3c** did not dissolve in water. After two recrystallization steps the impurity in **3c** was reduced to 2%. **3c**: 1H -NMR ($CDCl_3$): δ 1.2-1.4 (m, 19H), 1.5-1.8 (m, 6H), 2.75 (t, 2H), 4.1 (m, 2H), 6.7 (dt, $^3J = 1.8$ Hz, $^4J = 0.1$ Hz, 1H), 6.98 (d, $^3J = 3.7$ Hz, 1H), 7.0 (d, $^3J = 3.7$ Hz, 1H), 7.02 (dd, $^3J = 4.8$ Hz, $^3J = 3.5$ Hz, 1H), 7.06 (d, $^3J = 4.0$ Hz, 1H), 7.16 (dd, $^3J = 3.5$ Hz, $^4J = 1$ Hz, 1H), 7.21 (dd, $^3J = 4.8$ Hz, $^4J = 1$ Hz, 1H). Elemental analysis: Calculated for $C_{26}H_{37}O_3PS_3$: 58.74% C, 6.87% H; Found: 59.21% C, 7.11 H.

Other oligomers: [2,2';5',2'']terthiophene-5-carboxylic acid (**1a**, T_3COOH),²⁶ [2,2';5',2'']terthiophene-5-aldehyde (**1b**, T_3CHO),²⁷ (*E,E*)-4-{4-(4-methyl-2,5-bis[(*S*)-2-methylbutoxy]styryl)-2,5-bis[(*S*)-2-methylbutoxy]benzoic acid (**1c**, OPV3-COOH),²⁸ and (*E,E,E*)-4-[4-{4-(3,4,5-tridodecyloxystyryl)-2,5-bis[(*S*)-2-methylbutoxy]styryl}-2,5-bis[(*S*)-2-methylbutoxy]styryl]benzoic acid (**1d**, OPV4-COOH)²⁹ have been prepared according to published methods.

Characterization: AFM measurements were performed on a Nanoscope IIIa (Digital Instruments), using a RTESP tip. Elemental analysis was performed on a Perkin Elmer Series II CHNS/O analyzer 2400. Size exclusion chromatography (SEC) was performed on a Shimadzu LC-10AD, using an Applied Biosystems 785A UV absorbance detector and a 1×10^4 Å Calmix D column for M_w between 1000 and 500.000 Dalton. UV-vis spectra were recorded using a Perkin-Elmer Lambda 40 spectrometer. FT-IR spectra were recorded using a Perkin-Elmer Spectrum One FT-IR ATR

spectrometer. XPS spectra were recorded using a VG Scientific Escalab 200 MKII utilizing a twin Al K α X-ray source. Small angle X-ray scattering (SAXS) measurements were performed on a nanoparticle solution in toluene, using a Rigaku Geigerflex with a Cu K α X-ray source operating at a tube voltage of 40 kV and a current of 30 mA.

Photoluminescence: photoluminescence spectra were recorded on an Edinburgh Instruments FS920 double-monochromator spectrometer and a Peltier-cooled red-sensitive photomultiplier. Spectra were recorded at room temperature using 2.5 mL of a 7×10^{-6} M oligomer concentration in chloroform or toluene. The fluorescence quenching was performed using a 0.1 mg mL^{-1} solution in chloroform or toluene of the TiO₂ nanoparticles prepared as described above. Time-correlated single photon counting fluorescence studies were performed using an Edinburgh Instruments LifeSpec-PS consisting of a 400 nm picosecond (pulse width ~50 ps) laser (PicoQuant PDL 800B) operated at 2.5 MHz and a Peltier-cooled Hamamatsu micro-channel plate photomultiplier (R3809U-50). Lifetimes were determined after deconvolution with the instrument response function using the Edinburgh Instruments software package.

- 1 Marguerettaz, X.; Fitzmaurice, D. *J. Am. Chem. Soc.* **1994**, *116*, 5017.
- 2 Connolly, S.; Rao, N.; Rizza, R.; Zaccheroni, N.; Fitzmaurice, D. *Coord. Chem. Rev.* **1999**, *185-186*, 277.
- 3 Connolly, S.; Fitzmaurice, D. *Adv. Mater.* **1999**, *11*, 1202.
- 4 Marguerettaz, X.; Merrins, A.; Fitzmaurice, D. *J. Mater. Chem.* **1998**, *8*, 2157.
- 5 Ipe, B. I.; Thomas, K. G.; Barazzouk, S.; Hotchandani, S.; Kamat, P. V. *J. Phys. Chem.* **2002**, *106*, 18.
- 6 Kotov, N. A.; Meldrum, F. C.; Fendler, J. H. *J. Phys. Chem.* **1994**, *89*, 8827
- 7 Wu, X.; Wang, D.; Yang, S. *J. Colloid Interface Sci.* **2000**, *222*, 37.
- 8 Duffy, N. W.; Dobson, K. D.; Gordon, K. C.; Robinson, B. H.; McQuillan, A. J. *Chem. Phys. Lett.* **1997**, *266*, 451.
- 9 Nakamoto, K. *Infrared and Raman Spectra of Inorganic and Organic Compounds*, Wiley-Interscience, New York, **1978**, p. 230.
- 10 Bahnemann, D. W. *Isr. J. Chem.* **1993**, 115.
- 11 Enright, B.; Fitzmaurice, D. *J. Phys. Chem.* **1996**, *100*, 1027.
- 12 Balzani, V. *Electron transfer in chemistry* Wiley, Weinheim, **2001** Vol. 5 *Molecular level electronics, imaging and information, energy and environment*. p. 619. Table 1.
- 13 a) Shepard, M. J.; Paddon-Row M. N.; Jordan, K. D. *J. Am. Chem. Soc.* **1994**, *116*, 5328. b) Closs, G. L.; Miller, J. R. *Science* **1988**, *240*, 440.
- 14 Smalley, J. F.; Feldberg, S. W.; Chidsey, C. E. D.; Linford, M. R.; Newton, M. D.; Liu, Y. P. *J. Phys. Chem.* **1995**, *99*, 13141.
- 15 Asbury, J. B.; Ellingson, R. J.; Gosh, H. N.; Ferrere, S.; Nozik A. J.; Lian, T. *J. Phys. Chem. B* **1999**, *103*, 3110.
- 16 Asbury, J. B.; Hao, E.; Wang Y.; Lian, T. *J. Phys. Chem. B* **2000**, *104*, 11957.
- 17 a) Galoppini, E.; Guo, W.; Qu P.; Meyer, G. J. *J. Am. Chem. Soc.* **2001**, *123*, 4342. b) Galoppini, E.; Guo, W.; Zhang, W.; Hoertz, P. G.; Qu P.; Meyer, G. J. *J. Am. Chem. Soc.* **2002**, *124*, 7801.
- 18 a) Clifford, J. N.; Yahioğlu, G.; Milgrom L. R.; Durrant, J. R. *Chem. Commun.* **2002**, *1260*. b) Hirata, N.; Lagref, J.-J.; Palomares, E. J.; Durrant, J. R.; Nazeeruddin, M. K.; Grätzel M.; Di Censo, D. *Chem. Eur. J.* **2004**, *10*, 525. c) Clifford, J. N.; Palomares, E. J.; Nazeeruddin, M. K.; Grätzel, M.; Nelson, J.; Li, X.; Long N. J.; Durrant, J. R. *J. Am. Chem. Soc.* **2004**, *126*, 5225.
- 19 Hempenius, M. A.; Langeveld-Voss, B. M. W.; Van Haare, J. A. E. H.; Janssen, R. A. J.; Sheiko, S. S.; Spatz, J. P.; Möller M.; Meijer, E. W. *J. Am. Chem. Soc.* **1998**, *120*, 2798.
- 20 Berlin, A.; Zotti, G.; Schiavon G.; Zecchin, S. *J. Am. Chem. Soc.* **1998**, *120*, 13453.
- 21 Péchy, P.; Rotzinger F. P.; Nazeeruddin, M. K.; Kohle, O.; Zakeeruddin, S. M.; Humphy-Baker, R.; Grätzel, M. *J. Chem. Soc. Chem. Commun.* **1995**, *1*, 65-66.
- 22 Oevering, H.; Paddon-Row, M. N.; Heppener, M.; Oliver, A. M.; Cotaris, E.; Verhoeven J. W.; Hush, N. S. *J. Am. Chem. Soc.* **1987**, *109*, 3258.
- 23 a) Kuhn, H. *J. Photochem.* **1979**, *10*, 111. b) Möbius, D. *Ber. Bunsenges. Phys. Chem.* **1978**, *82*, 848.

- 24 a) Hoffmann, R.; Imamura A.; Hehre, W. J. *J. Am. Chem. Soc.* **1968**, *90*, 1499. b) Padden-Row M. N., *Acc. Chem. Res.* **1982**, *15*, 245.
- 25 Padden-Row, M. N.; Shephard, M. J. *J. Am. Chem. Soc.* **1997**, *119*, 5355.
- 26 Kagan, J.; Arora, S. K.; Ustunol, A. *J. Org. Chem.* **1983**, *48*, 4076.
- 27 MacEachern, A.; Soucy, C.; Leitch, L. C.; Arnason, J. T.; Morand, P. *Tetrahedron* **1988**, *44*, 2403.
- 28 Schenning, A. P. H. J.; Peeters, E.; Meijer, E. W. *J. Am. Chem. Soc.* **2000**, *122*, 4489.
- 29 Schenning, A. P. H. J.; Jonkheijm, P.; Peeters, E.; Meijer, E. W. *J. Am. Chem. Soc.* **2001**, *123*, 409.

Chapter 3

ZnO nanoparticles for application in bulk heterojunction solar cells

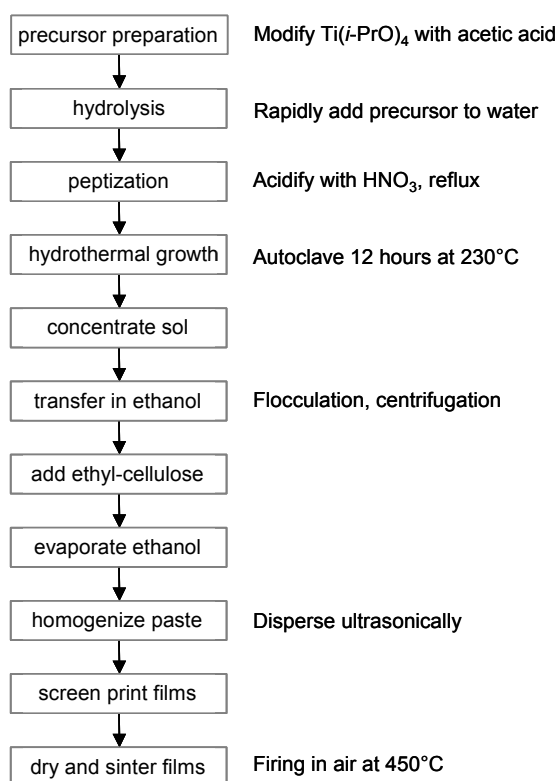
Abstract

This chapter introduces ZnO nanoparticles for application in bulk heterojunction type solar cells. ZnO nanoparticles of 5 nm in size have been synthesized at relatively low temperatures. The nanoparticles are crystalline, monodisperse in size, and soluble in apolar organic solvents. In a second step these nanoparticles can be converted into rods. The electrical and optical properties of these nanoparticles are characterized using different techniques. These nanoparticles can be made n-type by electron doping, leading to a complete quenching of the visible photoluminescence. The high solubility in apolar solvents, combined with their electron accepting and transport properties, makes the ZnO nanoparticles interesting candidates for application in bulk heterojunction photovoltaic devices.

3.1 Introduction

To construct bulk heterojunction hybrid polymer solar cells, metal oxide nanoparticles have to be created and blended with conjugated polymers. The synthesis of metal oxide nanoparticles is the subject of this chapter. Successful blending with conjugated polymers, requires the synthesis of nanoparticles that are small and soluble in apolar solvents. The application of metal oxides in solar cells has received considerable attention since O'Regan and Grätzel showed well performing dye sensitized solar cells based on nano-crystalline TiO_2 ¹. The synthesis of nano-crystalline TiO_2 electrodes is described in scheme 3.1^{2,3}. After hydrolysis of the TiO_2 precursor ($\text{Ti}(i\text{-PrO})_4$ or TiCl_4), small 1-2 nm sized particles are obtained during the peptization step. Under hydrothermal conditions these primarily particles are converted into 20 nm sized particles with a better crystallinity. Together with a binder (ethyl-cellulose or polyethylene glycol), these particles are ultrasonically redispersed into a paste.

Harsh hydrothermal synthetic conditions are required to crystallize the TiO_2 . Aggregate formation, being the result of these harsh conditions, leads to a low solubility of the particles in most solvents. The TiO_2 particles can be redispersed into alcoholic media but alcohols are not suitable solvents for conjugated polymers. To overcome this problem, Salafsky *et al.*⁴ used a methanol soluble precursor PPV. Blending with TiO_2 nanoparticles and converting the precursor to PPV, led to a small photovoltaic effect, with external quantum efficiency of 2%. The recent work of Kwong *et al.* shows application of TiO_2 nanoparticles in well working bulk heterojunction devices with an AM1.0 solar conversion efficiency of 0.42%⁵. For most TiO_2 nanoparticles reported in literature, solubility in organic solvents is achieved by addition of surfactants at some stage during synthesis⁶. As has been shown in chapter 2, using stearic acid as the surfactant and mild synthetic conditions, solubility in organic solvents has been achieved. However, a similar procedure⁷ led to poorly crystalline materials that are not likely suitable for application in bulk heterojunction



Scheme 3.1 Synthetic procedure for nano-crystalline TiO_2 electrodes as used in the dye-sensitized solar cells.

solar cells. Poorly crystalline materials are in most cases the outcome of sol-gel synthesis of TiO₂ nanostructures. Recently a procedure has been published showing the low temperature (80-100 °C) synthesis of crystalline TiO₂ nanoparticles and rods, capped with oleic acid to make them soluble in organic solvents like chloroform and hexane⁸. After exchange with phosphonic acids a high solubility of approximately 120 mg mL⁻¹ in chloroform has been obtained. The authors of that work recognize, that for application in photovoltaic devices the surfactants should be removed. This is well shown by Greenham *et al.*⁹ in their work on trioctylphosphineoxide (TOPO) coated CdSe nanocrystals. Only after efficient removal of the surfactant electron transfer processes occur and a photovoltaic effect is observed^{10,11}. The conclusion is that for well performing bulk heterojunction photovoltaic devices surfactant-coated oxide nanoparticles are not desired.

An alternative for TiO₂ is ZnO, because it shows great similarity to TiO₂ but has some advantages. Some relevant properties of ZnO are summarized in table 3.1¹². At room temperature the stable phase is a wurtzite type crystal, and in contrast to TiO₂ this is already formed at temperatures as low as 4°C¹³.

Table 3.1 Some relevant properties of ZnO

Property	Value
Density	5.606 g cm ⁻³
Stable phase at 300 K	Wurtzite
Melting point	1975 °C
Static dielectric constant	8.656
Band gap	3.2 (direct)
Conduction band level	- 4.4 V versus vacuum ¹⁴
Intrinsic carrier concentration	< 10 ⁶ cm ⁻³
Exciton binding energy	60 meV
Electron effective mass	0.24
Electron mobility at 300 K	180 cm ² V ⁻¹ s ⁻¹ ¹⁵ , >100 cm ² V ⁻¹ s ⁻¹ ¹⁶
Hole effective mass	0.59
Hole mobility at 300 K	5-50 cm ² V ⁻¹ s ⁻¹

The conduction band energy level is the same as found for TiO₂, implying that ZnO will also function as electron accepting species in photovoltaic devices. Keis *et al.* show the application of ZnO in dye-sensitized solar cells. This cell's performance (5%) is less than reported for TiO₂ even though electron transport through the ZnO appeared better than through TiO₂¹⁷. The high electron mobility encountered in bulk crystalline ZnO makes this material very interesting for application in photovoltaic devices. The values shown in table 3.1 are for pure non-doped ZnO (> 100 cm² V⁻¹ s⁻¹) and for slightly n-type doped ZnO (180 cm² V⁻¹ s⁻¹) bulk crystalline materials, not for nanoparticulate

electrodes. Meulenkamp¹⁸ and Noack¹⁹ showed that in these nanoparticulate films, interparticle electron transfer slows down the electron transport. Still reasonable electron mobilities of 10^{-3} till 10^{-1} $\text{cm}^2 \text{V}^{-1} \text{s}^{-1}$ have been found, depending on the electron density in the ZnO ²⁰. Small monodisperse nanoparticles are made using a simple wet-chemical procedure²¹, allowing dispersion into apolar solvents, without the use of surfactants. When considering application in bulk heterojunction solar cells, making non-coated, soluble, crystalline nanoparticles at low temperatures is the biggest advantage of ZnO over TiO_2 .

ZnO is a very versatile material; in recent years a plentitude of different structures of ZnO have been made. Figure 3.1 shows a small collection of some of the versatile structures and shapes that can be obtained²².

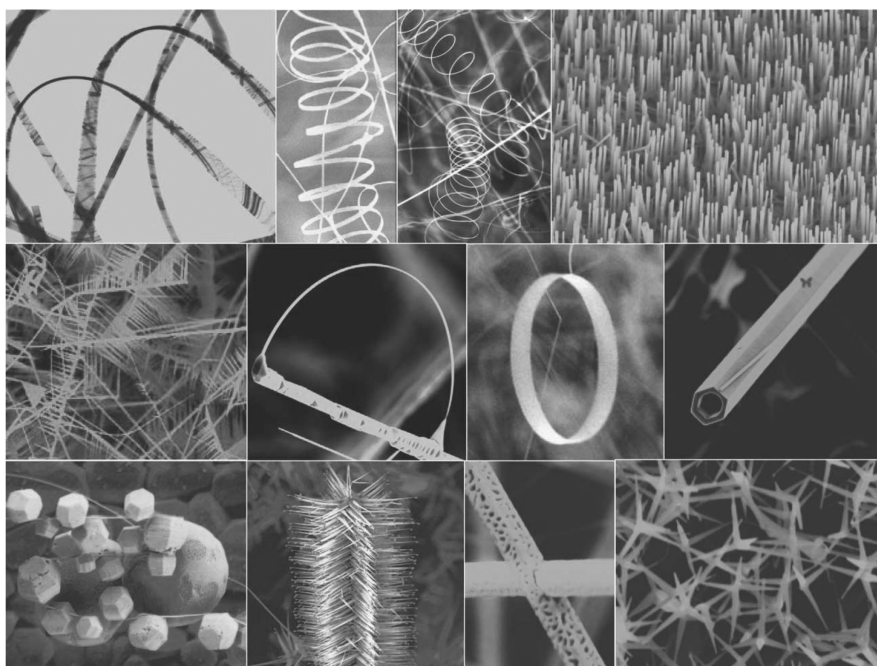


Figure 3.1 A diverse group of structures can be grown from ZnO using controlled thermal evaporation of ZnO powders. Reprinted with permission from Elsevier.²³

Simple wet-chemical techniques also allow the synthesis of a wide range of structures. For example nano pillars can be grown aligned on various substrates^{24,25}. Well defined ZnO nanoparticles and rods can also be formed; and this is the subject of the next section. The diversity of nanostructures combined with their electrical properties, makes ZnO one of the most actively investigated nano-materials in current research.

3.2 Synthesis of soluble non-surfactant coated ZnO nanoparticles

ZnO nanoparticles of approximately 5 nm in diameter have been synthesized by hydrolysis and condensation of zinc acetate dihydrate by potassium hydroxide in methanol, using the method of Pacholski *et al.*²¹. The synthesis is based on procedures described previously by Henglein *et al.*²⁶ using NaOH as the base, and Meulenkamp¹³ using LiOH. Thus prepared nanoparticles are insoluble in pure methanol, but by addition of suitable amounts of less polar solvents like dichloromethane, chloroform, or chlorobenzene stable solutions are obtained. No additional surfactants or ligands are needed to disperse the ZnO nanoparticles in these solvent mixtures to reach solubilities up to 75 mg mL⁻¹. The size of the nanoparticles can be increased by raising the precursor concentration in the starting solution and by increasing the reaction time²⁷. The size of the particles also strongly depends on the Zn²⁺:OH⁻ ratio. A ratio of 1:1.7 is used in this work, and gives stable colloidal solutions. Increasing the Zn²⁺:OH⁻ ratio from 1:1 to 1:1.75 results in larger particles²⁷. A further increase of the Zn²⁺:OH⁻ ratio leads to smaller particles, and at a ratio of 1:2.5 the sol becomes unstable²⁷.

For stable (> two weeks) solutions, a certain amount of methanol is needed. The procedure that is described in the experimental section for chlorobenzene based ZnO sols, leads to 18 ± 3 vol.-% of methanol in chlorobenzene. The amount of methanol is dependent on the amount of ZnO in the obtained solution, which ranges from 60 to 75 mg mL⁻¹. The amount of methanol can be decreased to 10 vol.-% by centrifugation of the ZnO precipitate. Initially the ZnO sols are almost optically clear, slightly translucent. The sols are not unlimitedly stable, and show some turbidity after a few weeks. Addition of small amounts of *n*-propylamine leads to completely clear solutions with long-time stability²⁸. For characterization, and the evaluation of the photovoltaic effect (in chapter 4) no amines are used, because the stability of approximately two weeks is sufficient.

As described by Pacholski *et al.*²¹, ZnO nanorods can be grown from the nanoparticles. The synthesis of approximately 5-by-25 nm sized nanorods has been achieved by heating a 10 times concentrated sol of the ZnO nanoparticles at 60 °C in methanol for 15 hours. The length of the rods can be tuned varying the heating time. The solubility of the rods is rather low, compared to the nanoparticles; only after addition of *n*-propylamine stable sols have been obtained.

3.3 Characterization of ZnO nanoparticles and rods

3.3.1 Size and composition analysis of ZnO nanoparticles

The size and size distribution of the ZnO nanoparticles and rods have been determined with transmission electron microscopy (TEM). Following the procedure described in the experimental section for ZnO nanoparticles, particles of 5 nm in diameter have been obtained, which appear monodisperse (figure 3.2a). In a consecutive step these nanoparticles have been converted into nanorods. Nanorods, prepared by heating at 60 °C a concentrated nanoparticle solution for 20 hours, are shown in figure 3.2b.

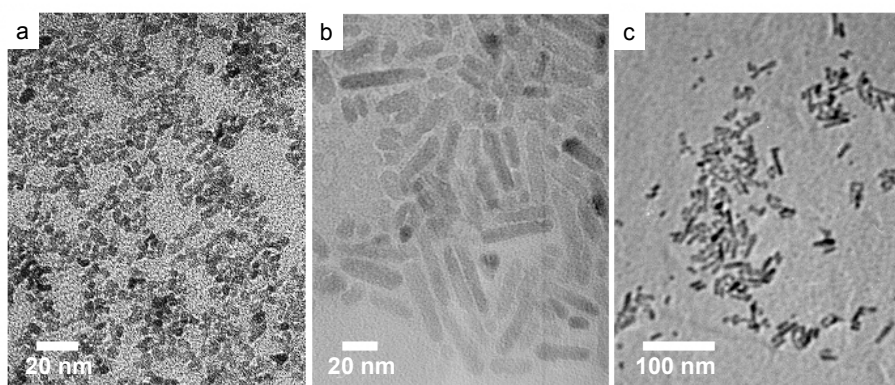


Figure 3.2 TEM photographs of: a) ZnO nanoparticles prepared with a $\text{Zn}^{2+}:\text{OH}^-$ ratio of 1.7. b) Rods prepared after heating a concentrated solution of these nanoparticles for 20 hours. c) Rods prepared after heating a concentrated solution of these nanoparticles for 15 hours.

Rods formed after 20 hours are up to 60 nm in length and are almost insoluble in organic solvents. Heating for 15 hours gives nanorods of approximately 25 nm in length (figure 3.2c), these can be dissolved in chloroform and chlorobenzene using 2 vol.-% *n*-propylamine.

Because the extension of the electronic wavefunctions of semiconductor quantum dots is confined to the particle, their energy levels are size-dependent and UV-vis spectroscopy can be used to determine the diameter of semiconductor nanoparticles like ZnO. Figure 3.3a shows the UV absorption spectrum of ZnO nanoparticles in a chloroform:methanol mixture. According to a relation that has been derived by Meulenkamp¹³ the observed $\lambda_{1/2}$ ²⁹ of 360 nm corresponds to a particle of 4.9 nm in diameter³⁰. The rods synthesized after 15 and 20 hours, both give a similar UV absorption with a $\lambda_{1/2}$ of 365 nm corresponding to 6 nm sized particles according to this relation. As is shown by Meulenkamp¹³ the $\lambda_{1/2}$ levels off at approximately 365 nm after the nanoparticles reach a diameter of 6 nm. This indicates that the quantum confinement effect, and its effect on the UV absorption onset, is only present in smaller particles. Therefore the UV onset is not a measure for the size of bigger particles.

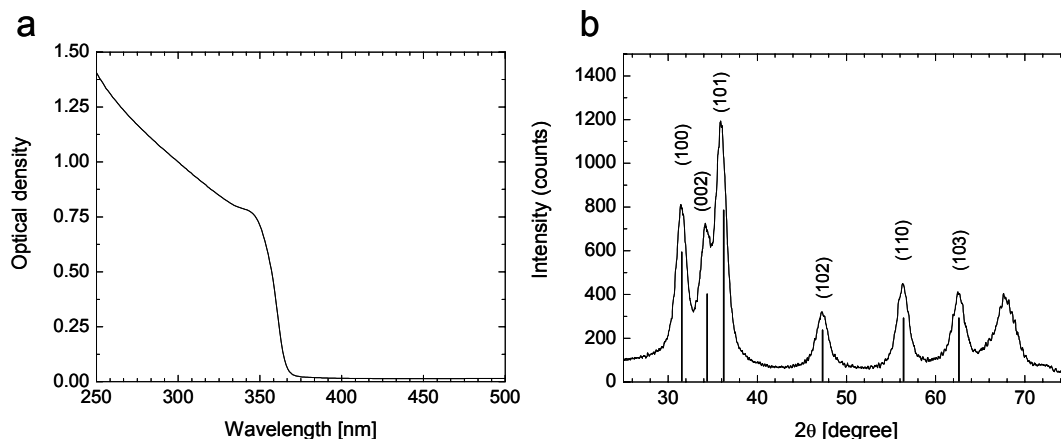


Figure 3.3 a) UV absorption spectrum of ZnO nanoparticles in a chloroform:methanol (v:v = 90:10) mixture. b) Powder X-ray diffraction pattern obtained from ZnO nanoparticles.

The XRD spectrum in figure 3.3b shows the formation of crystalline ZnO, the positions of the diffraction lines indicate the formation of a wurtzite type ZnO crystal³¹. The spectrum shows great resemblance to the spectra obtained by Pacholski *et al.* for spherical 5 nm sized particles²¹. Using the Scherrer formula³² an estimated diameter of 10 ± 2.5 nm is obtained, which is higher than expected based on the TEM and UV results. It is possible that removal of the high-boiling chlorobenzene for the preparation of the ZnO powder leads to a growth of the particles.

X-ray photoelectron spectroscopy (XPS) has been used to confirm the presence of ZnO. The XPS spectrum (figure 3.4a) shows the Zn 2p^{3/2} peak at a binding energy of 1022.8 eV and the Zn 2p^{1/2} at 1046.0 eV as expected for ZnO^{33,34}. Two O 1s peaks are visible in figure 3.4b, at binding energies of 530.1 and 531.8 eV. The peak at higher binding energy has been attributed to Zn-OH species on the surface of the nanoparticle³⁵.

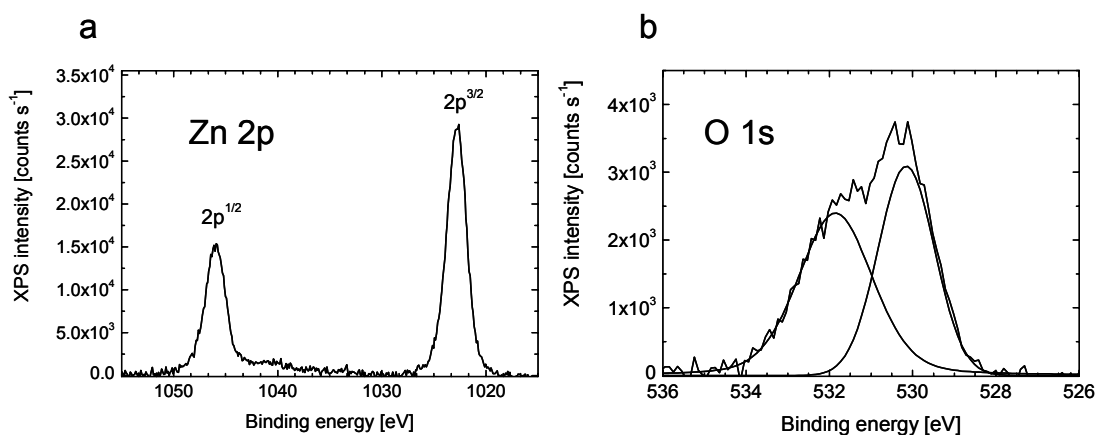


Figure 3.4 XPS spectra of ZnO nanoparticles, showing the Zn 2p peaks at 1022.8 eV and 1046.0 eV (a) and two O 1s peaks at 530.1eV and 531.8 eV (b).

Comparing the area of the Zn 2p^{3/2} peak with the O 1s peak and correcting for the atomic sensitivity factors^{33,36} gives a Zn/O ratio of 1.2. Because the Zn-OH O1s signal is included in this calculation the ratio is higher than expected. Formation of such high amount of hydroxyl species as indicated in figure 3.4b implies a correct Zn/O ratio of 0.72. Atomic sensitivity data are recorded for bulk materials and do not take into account compositional gradients in depth of the material. The presence of hydroxyl groups at the surface of the ZnO nanoparticles might lead to an overestimation of the sensitivity factor for the oxide O1s peak at 530.1 eV. This might explain the low oxygen contents calculated when intensity correction is performed using the bulk material based correction factors. The removal of K⁺ species by the washing procedure, as described in the experimental section, is very effective because no K 2p peaks are detected around 293.11 eV³⁷. Carbon can be observed in XPS (up to 10% compared to Zn), this stems from adsorbed carbon from the atmosphere, and from residual acetate groups on the surface of the particle. Weak signals from these acetate groups have also been detected by FT-IR.

3.3.2 Photo-physical characterization of ZnO nanoparticles

The visible photoluminescence of ZnO nanoparticles depends on the size of the nanocrystal^{38,39}. The observed maximum wavelength of the visible photoluminescence at 565 nm (2.2 eV) corresponds well to the emission reported for 4.4 nm sized TOPO (trioctylphosphineoxide) capped ZnO nanoparticles made by Shim and Guyot-Sionnest³⁹. The first trace in figure 3.5a shows the photoluminescence of a solution of ZnO nanoparticles in a chlorobenzene:methanol mixture (v:v = 80:20). After degassing the solution with argon, the photoluminescence drops when exposed to the excitation beam ($\lambda = 350$ nm) in the photoluminescence spectrometer (trace 2). After exposure to a bright xenon arc light source, with a significant amount of UV emission, the photoluminescence (trace 3) is completely quenched. An almost full recovery of the initial photoluminescence has been achieved by exposure to air, see the last trace in figure 3.5a.

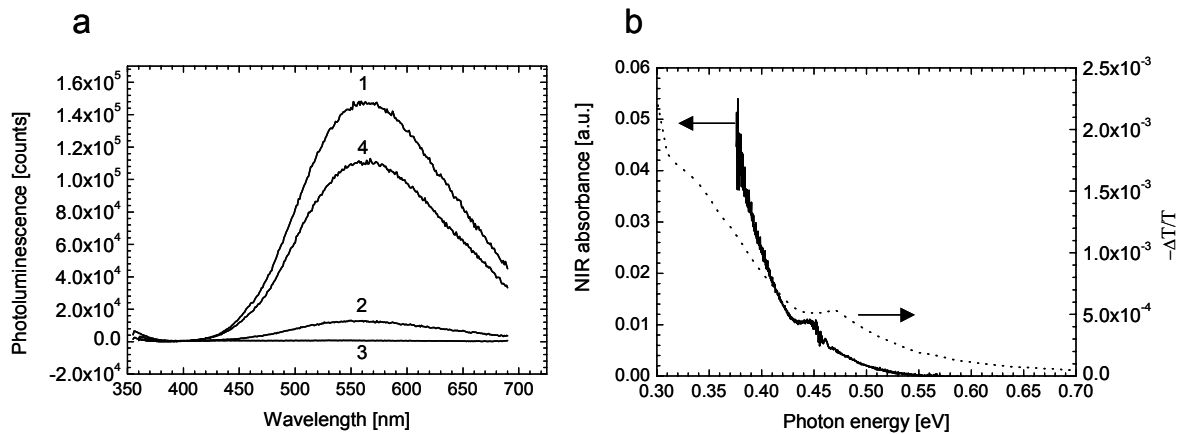


Figure 3.5 a) Photoluminescence spectra of ZnO nanoparticles in a chlorobenzene:methanol mixture (v:v = 80:20). Excitation wavelength was at 350 nm. Trace 1 shows the photoluminescence before degassing, trace 2 after degassing, the intensity drops during measurement, *i.e.* exposure to UV light in the excitation beam. Trace 3 is after exposure for 5 minutes to a Xe lamp. Trace 4 is after exposure to air, the response is immediate. b) NIR absorbance (left axis) and photoinduced absorption (right axis) spectra of a ZnO nanoparticulate film deposited on quartz. The NIR signal was obtained after exposure to a Xe lamp. The strong PIA signal was obtained by excitation the ZnO film with 350 nm and 363 nm, at 298 K exposed to air.

Van Dijken *et al.* identified the transition responsible for the visible emission in ZnO nanoparticles³⁸ as a transition of an electron from the conduction band to a deep trap level, where the electron combines with a deeply trapped hole. This hole is trapped at oxygen deficiency centers in the bulk of the nanoparticle³⁸, approximately 2.2 eV below the conduction band level, see figure 3.6a. The quenching of the emission by UV irradiation is due to the formation of n-type ZnO nanoparticles. Shim and Guyot-Sionnest³⁹ observed the formation of n-type ZnO nanoparticles upon chemical electron doping and UV illumination. In the non-degassed ZnO nanoparticle solution both methanol

and oxygen are present. After UV excitation the methanol is oxidized by the photoinduced hole, and the electron is scavenged by oxygen (figure 3.6a).

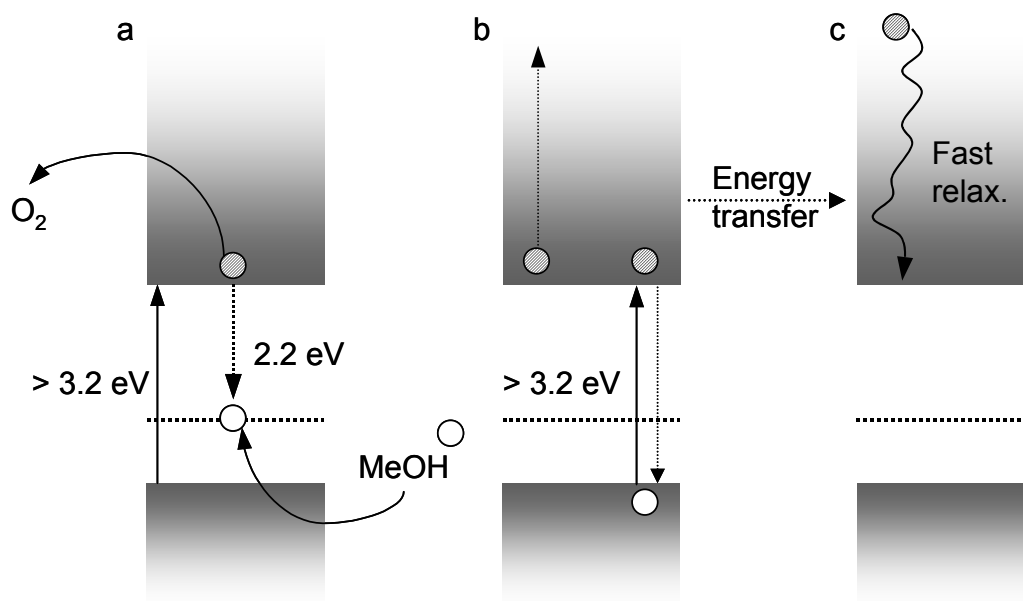


Figure 3.6 Processes occurring after UV excitation of ZnO nanoparticles in solution. a) Excitation of ZnO with UV light (> 3.2 eV) leads to trapping of the photoinduced hole at a level approximately 2.2 eV below the conduction level. When O_2 is present, the electron in the conduction band is scavenged; methanol present in the solution can be oxidized by the hole. b) If no O_2 is present the hole can still be scavenged by the methanol but the electron remains on the nanoparticle. The energy of a second excitation of this nanoparticle by UV light is immediately transferred to the electron in the conduction band. The electron-hole pair recombines without emission, a so-called Auger recombination. c) The result is a non radiative decay of this excited electron back to the lower level of the conduction band.

When the oxygen is removed, the hole can still be transferred to methanol, but the electron remains in the conduction band of the nanoparticle (figure 3.6b). The presence of this electron increases the possibility of fast Auger recombination. Upon excitation of the electron-doped nanoparticle, the energy of the exciton is immediately transferred to the free electron in the conduction band. The exciton recombination is non-radiative because the energy is transferred; as a result the photoluminescence is quenched. The excited electron in the conduction band of the ZnO nanoparticle (figure 3.6c) loses its excess energy by fast (non-radiative) vibronic relaxation. Because almost no photoluminescence remains (figure 3.5a), Auger recombination seems very effective. Removing the electrons from the conduction band by the addition of oxygen indeed leads to a restoration of the photoluminescence. The formation of n-type ZnO is confirmed by the near-infrared (NIR) and photoinduced absorption (PIA) experiments see figure 3.5b. Both are performed on ZnO films on quartz. The weak NIR absorption was observed after exposure of the film to a Xe lamp⁴⁰. Katoh *et al.*⁴¹ observed the same NIR absorbance of ZnO nanocrystalline films, after electron injection by

sensitizers or UV exposure. The NIR signal is stable for minutes indicating the long lifetime of the electrons in the ZnO conduction band. The photoinduced absorption signal was obtained after excitation of the ZnO nanoparticulate film with a modulated UV light probe beam. The strong PIA signal is only observed after exposure to oxygen (by exposure to air); without oxygen there is no transient signal. These experiments indicate that the injected electron in ZnO has a long lifetime when the hole is trapped, either by the methanol in solution or by deep trap levels in the nanoparticulate films. The result is an n-type doped ZnO nanoparticle.

3.3.3 Cyclic voltammetry and current-voltage measurements

Electron doping of ZnO nanoparticles has also been observed in cyclic voltammetry. A film of ZnO nanoparticles on the Pt working electrode is immersed in THF and measured against an Ag/AgCl reference electrode. The cyclic voltammogram (figure 3.7a) shows the reduction onset at -1.4 eV against Fc/Fc^+ (measured simultaneously). From the oxidation potential of ferrocene at + 0.63 vs NHE⁴² a reduction potential for ZnO nanoparticles at -3.8 eV is estimated⁴³. This value is higher than the value reported in table 3.1 (-4.4 eV). Using cyclic voltammetry gives a rough estimate for determination of the conduction band level, and the value is only an indication.

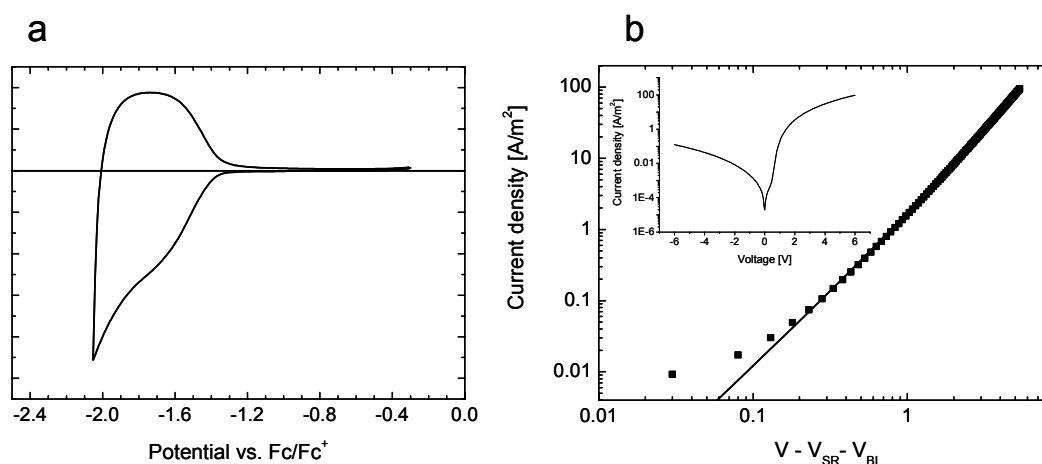


Figure 3.7 a) A cyclic voltammogram of a ZnO nanoparticulate film deposited on the Pt working electrode immersed in THF. The potential is reported against Fc/Fc^+ which was measured simultaneously. b) J - V characteristics of a ZnO:polystyrene blend containing 8 vol.-% ZnO. The voltage is corrected for the voltage drop (V_{SR}) due to a series resistance over the ITO and PEDOT:PSS layers (34Ω), and for the build-in potential (V_{BI}) of 0.62 V. The squares are the experimental data the solid line the fit according to equation 1. The inset shows a semilogarithmic plot of the current density (J) versus the non-corrected voltage.

The values for the electron-mobility reported in the introduction were measured from electrochemical experiments on ZnO films immersed in an electrolyte solution. One other way of calculating the mobility in a ZnO nanocrystalline film is to investigate the current density voltage characteristics. A film of the ZnO nanoparticles in-between PEDOT:PSS and aluminum did not show

a good diode behavior, but indicated the formation of an Ohmic layer between the aluminum and the PEDOT:PSS. A 250 nm thick film of polystyrene with 8 vol.-% ZnO nanoparticles gives a nice diode behavior, with a build-in voltage of 0.62 V, see the inset of figure 3.7b. As hole transport in this film is highly unlikely, the J - V characteristics of this film can give an indication of the electron mobility in the blend⁴⁴. Assuming the validity of a space-charge-limited model with a field dependent electron mobility, the J - V characteristic are approximately given by⁴⁵:

$$J = \frac{9}{8} \varepsilon_r \varepsilon_0 \mu_0 \frac{V^2}{L^3} \exp\left(0.89 \beta \sqrt{\frac{V}{L}}\right) \quad (1)$$

The static dielectric constant (ε_r) was taken as 8.7 for ZnO and 2.7 for polystyrene, for the blend a volume based average of $\varepsilon_r = 3.2$ has been obtained. The film thickness L and the dielectric constant have been set as fixed parameters to fit the above expression in the J - V curve as shown in figure 3.7b. A good fit has been obtained using $\mu_0 = 5.2 \times 10^{-6} \text{ cm}^2 \text{ V}^{-1} \text{ s}^{-1}$ for the zero field mobility, and $2.8 \times 10^{-4} \text{ m}^{1/2} \text{ V}^{-1/2}$ for the prefactor β . The obtained mobility is low compared to the value given for ZnO particulate films as shown in the introduction. Because the ZnO is diluted with polystyrene this result is not surprising. Increasing the amount of ZnO to 15 vol.-% leads to a lower build-in voltage of 0.37 V with worse diode characteristics. The calculated zero field mobility $\mu_0 = 8.2 \times 10^{-5} \text{ cm}^2 \text{ V}^{-1} \text{ s}^{-1}$ is higher in this case.

3.4 Conclusions

ZnO is a versatile material with promising electrical properties. The low temperature, and facile conversion into crystalline material, is a certain advantage of ZnO over TiO₂. ZnO nanoparticles of 5 nm in size can be obtained using a simple wet-chemical procedure. For the dispersion of these nanoparticles no surfactants are needed. From XPS it is clear ZnO has been formed, without potassium impurities. From the measured non-stoichiometric Zn/O ratio it might be concluded the ZnO is oxygen deficient. The visible photoluminescence of the nanoparticles also indicates the presence of oxygen defects. ZnO nanoparticles can be n-type doped by UV exposure, leading to the formation of a long-lived electron in the conduction band of the nanoparticle. Due to the presence of this electron, the photoluminescence of the nanoparticle is completely quenched as a result of fast Auger recombination. The presence of this photoinduced electron in the conduction band of ZnO nanoparticles is observed with PIA and NIR absorption spectroscopy. Charging of these nanoparticles can also be performed electrochemically, giving a rough estimate of the reduction potential of these nanoparticles of -3.8 eV vs. vacuum. The high mobility of ZnO nanocrystalline electrodes as reported in the introduction could not be measured, because a pure ZnO nanoparticulate film did not display a good diode behavior. A zero-field electron mobility of $5.2 \times 10^{-6} \text{ cm}^2 \text{ V}^{-1} \text{ s}^{-1}$ has been measured in blends of polystyrene with small amounts of ZnO. This shows the possibility of electron transport in blends, one requirement for application in photovoltaic devices.

3.5 Experimental

ZnO nanoparticles synthesis: ZnO nanoparticles were prepared using an adapted procedure based on the work of Pacholski *et al.*²¹ The general procedure used for the preparation of nanoparticles was as follows: zinc acetate dihydrate (Acros, >98%, 2.95 g, 13.4 mmol) was dissolved in methanol (125 mL) at 60 °C, a solution of KOH (Merck, 87%, 1.48 g, 23 mmol) in methanol (65 mL) was added in 10 min. to the zinc acetate dihydrate solution under vigorous stirring. Zinc-hydroxides precipitated but dissolved again. After 5 min. the solution became translucent and remained translucent, after 1.5 h the nanoparticles started to precipitate and the solution became turbid. After 2 h and 15 min., the heater and stirrer were removed and the nanoparticles were allowed to precipitate out of solution for an additional 2 h. Precipitate and mother-liquor were separated and the precipitate was washed twice with methanol (50 mL). After the washing steps (5 min.) the suspension was left unstirred for a minimum of 1 h to reach full precipitation. The washed precipitate was treated with chloroform or chlorobenzene (10 mL) to dissolve the nanoparticles. This solution was only slightly translucent, almost transparent and was stable for more than two weeks. The amount of methanol in the resulting

solution was determined with H^1 -NMR. Replacing the last washing step with a centrifugation step (4300 rpm, 5 min.) decreased the amount of methanol with a factor 2.

ZnO nanorods synthesis: The synthesis for the nanoparticles was followed up to the point of the precipitation step. After the reaction for 2 h and 15 min., the reaction mixture was concentrated 10 times by solvent evaporation at 30 °C. The precipitate dissolved again, and the clear solution was heated at 60 °C for 15 or 20 h. During heat treatment the nanorods started to precipitate. After the heat treatment, methanol (50 mL) was added and the ZnO rods were allowed to precipitate. This precipitate was washed as mentioned above. Stable solutions of nanorods were obtained after addition of a chloroform:*n*-propylamine mixture (10 mL, 2 vol.-% *n*-propylamine).

Transmission electron microscopy: A 1000x diluted solution of the nanoparticles or rods in dichloromethane was drop cast on a carbon-coated copper TEM grid. The TEM observations were conducted on a JEOL JEM-2000FX transmission electron microscope operated at an acceleration voltage of 200 kV.

Near steady-state photoinduced absorption (PIA) spectra were recorded between 0.25 and 1 eV by exciting a ZnO nanoparticulate film on quartz with a mechanically modulated (33 Hz) Ar-ion laser (Spectra Physics 2025) pump beam tuned to 355 and 363 nm (50 mW, beam diameter of 2 mm) and monitoring the resulting change in transmission (ΔT) of a tungsten-halogen white-light probe beam after dispersion by a triple grating monochromator, using Si, InGaAs, and (cooled) InSb detectors. This experiment was performed in air at 298 K.

UV and NIR: Absorption spectra were recorded on a Perkin-Elmer Lambda 900 spectrophotometer. The nanoparticles were measured in a solution of chloroform:methanol (v:v = 90:10) solution. The near infrared absorption was measured on a ZnO nanoparticulate film on quartz.

Photoluminescence: Spectra were recorded on an Edinburgh Instruments FS920 double-monochromator spectrometer with a Peltier-cooled red-sensitive photomultiplier. A 3 mL quartz photoluminescence cell containing a solution of as prepared nanoparticles in a chlorobenzene:methanol (v:v = 80:20) mixture was measured. Degassing was performed by bubbling the solution for a few minutes with argon. UV excitation was done by illumination with a 50 W xenon lamp for 5 minutes.

Current density voltage measurements: A chlorobenzene:methanol solution (v:v = 95:5) of 20 mg mL⁻¹ polystyrene and 10 mg mL⁻¹ ZnO nanoparticles was spin cast on top of a ITO patterned glass substrate covered with a poly(3,4-ethylenedioxythiophene):poly(styrenesulfonate) (PEDOT:PSS, Bayer AG) film. Aluminum (wire 99.999%, Engelhard-Clal.) layers were deposited by thermal evaporation in vacuum (5×10^{-6} mbar). *J-V* measurements were performed in a N₂ atmosphere at room temperature. In forward bias the ITO electrode was positively biased. *J-V* characteristics were measured with a Keithley 2400 source meter.

Cyclic voltammetry: Scans were performed on an μ Autolab type II with a PGSTAT30 potentiostat. Scan speed was 100 mV s⁻¹. A film of ZnO nanoparticles was drop cast on the Pt working electrode and immersed in a 0.1 M TBAH (tetrabutylammonium hexfluorophosphate) solution in THF. All potentials were measured against an Ag/AgCl electrode. Fc/Fc⁺ was added as an internal reference.

X-ray powder diffraction: Measurements were performed on a Rigaku Geigerflex with a Cu K α X-ray source operating at a tube voltage of 40 kV and a current of 30 mA.

X-ray photoelectron spectroscopy: XPS spectra were recorded using a VG Scientific Escalab 200 MKII utilizing a twin Al K α X-ray source. The powder sample was deposited on a carbon tape.

- 1 O'Regan, B; Grätzel, M. *Nature* **1991**, 353, 737.
- 2 Balzani, V. *Electron transfer in chemistry* Wiley, Weinheim, **2001** Vol. 5 *Molecular level electronics, imaging and information, energy and environment*. p. 613, Figure 6.
- 3 Barbé, C. J.; Arendse, F.; Comte, P.; Jirousek, M.; Lenzenmann, F. Shklover, V.; Grätzel, M. *J. Am. Ceram. Soc.* **1997**, 12, 3157.
- 4 Salafsky, J. S.; Lubberhuizen, W. H.; Schropp, R. E. I. *Chem. Phys. Lett.* **1998**, 290, 297.
- 5 Kwong, C. Y.; Djurišić, A. B.; Chui, P. C.; Cheng, K. W.; Chan, W. K. *Chem. Phys. Lett.* **2004**, 384, 372.
- 6 Scolan, E.; Sanchez, C. *Chem. Mater.* **1998**, 10, 3217.
- 7 Wu, X; Wang, D.; Yang, S. *J. Colloid Interface Sci.* **2000**, 222, 37.
- 8 Cozzoli, P. D.; Kornowski, A.; Weller, H. *J. Am. Chem. Soc.* **2003**, 125, 14539.
- 9 Greenham, N. C.; Peng, X.; Alivisatos, A. P. *Phys. Rev. B.* **1996**, 54, 17628.
- 10 Huynh, W. U.; Dittmer, J. J.; Alivisatos, A. P. *Science* **2002**, 295, 2425.
- 11 Sun, B.; Marx, E.; Greenham, N. C. *Nano Lett.* **2003**, 3, 961.
- 12 Pearton, S. J.; Norton, D. P.; Ip, K.; Heo, Y. W.; Steiner, T. *J. Vac. Sci. Technol. B.* **2004**, 22, 932.
- 13 Meulenkamp, E. A. *J. Phys. Chem. B.* **1998**, 102, 5566.
- 14 Hagfeldt, A.; Grätzel, M. *Chem. Rev.* **1995**, 95, 49.
- 15 Hutson, A. R. *Phys. Rev.* **1957**, 108, 222.
- 16 Hunger, R; Iwata, K; Fons, P; Yamada, A.; Matsubara, K.; Niki, S.; Nakahara, K.; Takasui, H. *Mat. Res. Soc. Symp. Proc.* **2001**, 668, H2.8.1.
- 17 Keis, K.; Magnusson, E.; Lindström, H.; Lindquist, S. E.; Hagfeldt, A. *Sol. Energy Mat. Sol. Cells.* **2002**, 73, 51.
- 18 Meulenkamp, E. A. *J. Phys. Chem. B.* **1999**, 103, 7831.
- 19 Noack, V.; Weller, H.; Eychmüller, A. *J. Phys. Chem. B.* **2002**, 106, 8514.
- 20 Roest, A. L.; Kelly, J. J.; Vanmaekelbergh, D.; Meulenkamp, E.A. *Phys. Rev. Lett.* **2002**, 89, 036801-1.
- 21 Pacholski, C.; Kornowski, A.; Weller, H. *Angew. Chem. Int. Ed.* **2002**, 41, 1188.
- 22 Wang, Z. L. *Mater. Today* **2004**, 7, 26.
- 23 Reprinted from: *Materials Today*, Vol 7, Z. L. Wang, Nanostructures of ZnO, pp 26-33, 2004, with permission from Elsevier.
- 24 Vayssieres, L. *Adv. Mater.* **2003**, 15, 464.
- 25 Greene, L.; Law, M.; Goldberger, J.; Kim, F.; Johnson, J. C.; Zhang, Y.; Saykally, R. J.; Yang, P. *Angew. Chem. Int. Ed.* **2003**, 42, 3031.
- 26 Haase, M.; Weller, H; Henglein, A. *J. Phys. Chem.* **1988**, 92, 482.
- 27 Thesis, Claudia Pacholski, Hamburg University, July 2002.
- 28 The precise role of *n*-propylamine is not known but it is reasonable to assume that it coordinates to cationic sites on the ZnO surface, thereby shielding the surface from the apolar solvent.

- 29 $\lambda_{1/2}$ is defined as the wavelength at which the absorption was 50% of that at the shoulder (exitonic peak) shown in figure 3.3a.
- 30 Using: $1240/\lambda_{1/2} = 3.301 + 294/D^2 + 1.09/D$, $\lambda_{1/2} = 360$ nm (see figure 3.3a)
- 31 The correct positions (in 2θ) for the peaks are: 31.8° (100), 34.5° (002), 36.3° (101), 47.5° (102), 56.6° (110), and 62.9° for the (103) diffraction line. Calculated using the ICSD database <http://www.cmbi.kun.nl/icsd> Albertsson, J.; Abrahams, S. C.; Kvik, A. *Acta Cryst. B.* **1983**, *45*, 34.
- 32 $D = 0.9*\lambda/(\beta\cos\theta)$, $\lambda = 1.54$ Å, $\beta = \text{FWHM}$ (in radians), $\theta = \text{diffraction angle}$, the diameter was averaged on all diffraction peaks.
- 33 Wagner C. D.; Riggs, W. M.; Davis, L. E.; Moulder, J. F.; Muilenburg, G. E. *Handbook of X-ray photoelectron spectroscopy*, Perkin Elmer, Minnesota, **1979**.
- 34 Wagner, C. D.; Davis, L. E.; Zeller, M. V.; Taylor, J. A.; Raymond R. M.; Gale L. H. *Surf. Interface Anal.* **1981**, *3*, 211.
- 35 Asakuma, N; Hirashima, H.; Imai, H.; Fukui, T.; Maruta, A.; Toki, M. *J. Appl. Phys.* **2002**, *92*, 5707.
- 36 The atomic sensitivity factors are 3.73 for the Zn $2p^{3/2}$ peak, 0.711 for the O1s peak, and 0.296 for the C1s peak. The measured XPS peak areas have been normalized by these sensitivity factors.
- 37 One previous XPS measurement on a single sample did report the presence of small amounts of potassium impurities. The experiment reported in this chapter is performed on a mixed sample from 10 batches of ZnO nanoparticles and does not show a contribution of potassium impurities.
- 38 Van Dijken, A.; Meulenkaamp, E. A.; Vanmaekelbergh, D.; Meijerink, A. *J. Lumin.* **2000**, *90*, 123.
- 39 Shim, M.; Guyot-Sionnest, P *J. Am. Chem. Soc.* **2001**, *123*, 11651.
- 40 The ZnO nanoparticulate film was deposited at the inside of a quartz NIR cell and sealed in a glovebox, to remove the oxygen.
- 41 Katoh, R.; Furube, A.; Hara, K.; Murata, S.; Sugihara, H.; Arakawa, H.; Tachiya, M. *J. Phys. Chem. B.* **2002**, *106*, 12957.
- 42 Pavlishchuk, V. V.; Addison, A. W. *Inorg. Chim. Acta* **2000**, *298*, 97.
- 43 Using a NHE level relative to vacuum of -4.6 eV.
- 44 The 8 vol.-% ZnO in the blends is below the theoretical percolation threshold, however due to phase separation percolating pathways might form. The observation of high currents in forward bias is evidence for the presence of percolating pathways of ZnO nanoparticles.
- 45 Manabe, K.; Hu, W.; Matsumura, M.; Naito, H. *J. Appl. Phys.* **2003**, *94*, 2024.

Chapter 4

Photovoltaic devices from zinc oxide nanoparticles and conjugated polymers

Abstract

This chapter describes bulk heterojunction type photovoltaic devices from blends of ZnO nanoparticles and conjugated polymers. The photovoltaic effect of these devices depends on the choice of solvent, the amount of ZnO, and the thickness of the active blend layer. Optimized solar cells have an estimated AM1.5 performance of 1.6%, close to the performance reported in literature for a similar hybrid polymer solar cell based on CdSe nanorods. Incident photon to current conversion efficiencies (IPCE) show that up to 40% of the incident photons can be collected as charges. Incident light power measurements indicate a small deviation from a linear relationship between the short circuit current and the illumination intensity, showing that non-geminate recombination is not the major loss process in this type of solar cells. At high light intensities the performance of the cell drops, due to a decreasing fill factor (FF). Attempts to improve the photovoltaic effect have been performed by investigating the effect of regio-regular poly(3-hexylthiophene) and ZnO nanorods.

4.1 Introduction

The concept of bulk heterojunction photovoltaic devices has proven to be useful, as explained in chapter 1. It is a relative simple concept and promising AM1.5 efficiencies up to 4% have been achieved for a combination of a methanofullerene (PCBM) and regio-regular polyalkylthiophenes¹. In a bulk heterojunction solar cell (see figure 4.1a) excitons are created close to an interface between phase separated p- and n-type materials. At the interface charge separation takes place, and the electrons are transported to the metal electrode (often aluminum) and the holes are transported through the p-type material to the transparent conducting electrode (often indium tin oxide). The challenge in making bulk heterojunction type of solar cells is to find a balance between a high interface area for effective photogeneration of charges, and phase separation into continuous p- and n-type domains for an effective transport of charges towards the electrodes. This chapter combines the n-type properties of ZnO nanoparticles with the light absorbing and p-type properties of conjugated polymers.

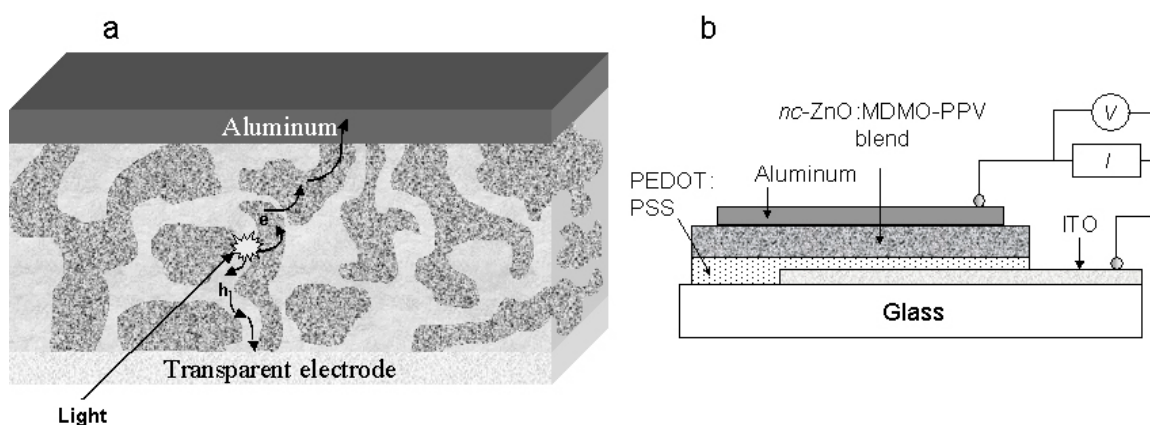


Figure 4.1 a) Visualization of the working principle of a bulk heterojunction solar cell, showing the excitation by light and the transport of holes and electrons to opposite electrodes. b) Schematic drawing of the design of a bulk heterojunction solar cell: the active blend layer of *nc*-ZnO:MDMO-PPV is sandwiched between two electrodes. For current-voltage measurements the aluminum and the ITO electrode are contacted.

The expectation that ZnO nanoparticles will work in bulk heterojunction type solar cells is based on the work performed on CdSe nanorods in combination with conjugated polymers². In contrast to CdSe, ZnO does not absorb light in the visible region of the solar emission spectrum, and therefore cannot play a role in harvesting the solar emission. However, unlike CdSe, ZnO is non-toxic. For this reason, ZnO can be used in the construction of environmental-friendly, “green” photovoltaic devices.

ZnO offers an additional advantage over CdSe. An effective photoinduced electron transfer from the polymer to trioctylphosphineoxide (TOPO) coated CdSe nanorods only occurs after removal of the TOPO ligand³. This ligand can be exchanged for pyridine by washing with methanol, dissolving in pyridine, and precipitation in hexanes⁴. Successful blending of pyridine coated nanorods requires chloroform:pyridine solvent mixtures⁵. In contrast, ZnO nanoparticles, synthesized as described in

chapter 3, can be processed from organic solvents in combination with polymers without the need of surfactants. To improve solubility of the ZnO nanoparticles in organic apolar solvents, only a small amount (< 5 vol.-%) of methanol is necessary.

This chapter shows that the conjugated polymer and the ZnO nanoparticles can be processed from a common solvent mixture and used to construct solar cells with efficiencies similar to those obtained using CdSe.

The design of this bulk heterojunction solar cell is shown in figure 4.1b. A mixture of crystalline ZnO nanoparticles and a conjugated polymer like MDMO-PPV (*nc*-ZnO:MDMO-PPV), is spin cast on a poly(3,4-ethylenedioxythiophene):poly(styrenesulfonate) (PEDOT:PSS) film on a UV-ozone cleaned indium tin oxide (ITO) coated glass substrate. The ITO-PEDOT:PSS combination serves as the transparent conducting electrode (TCO). The solar cell is completed by thermal vacuum evaporation of an aluminium electrode. The working-principle of such a device is shown in figure 4.2. The energy levels relative to vacuum show the HOMO (5.3 eV) and LUMO (3.0 eV) levels of MDMO-PPV⁶ and the valence (7.6 eV) and conduction (4.4 eV) bands of ZnO⁷. The work function (versus vacuum) of the ITO-PEDOT:PSS combination has been determined to be approximately 5.0 eV⁸, and 4.3 eV has been taken for the aluminum top electrode⁹.

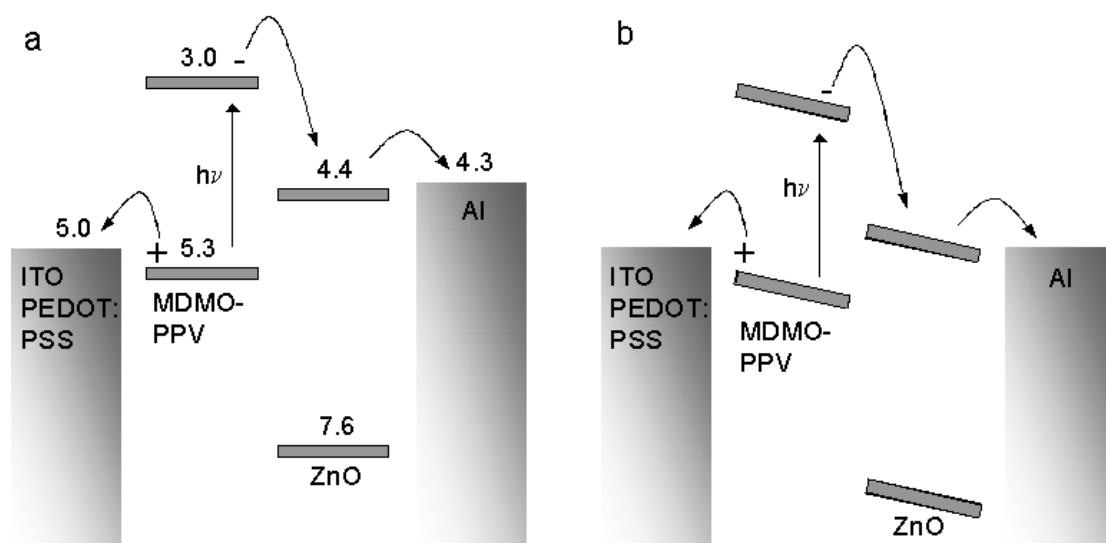


Figure 4.2 Simplified band diagrams showing a) The energy levels (in eV) relative to vacuum, under open circuit conditions. b) Under short circuit conditions the alignment of the energy levels of aluminum and the ITO-PEDOT:PSS creates an internal field.

The conduction band level of ZnO is capable of accepting electrons from the LUMO of MDMO-PPV, and the holes on MDMO-PPV can be injected into the ITO-PEDOT:PSS, see figure 4.2a (open circuit condition). Under short circuit conditions (figure 4.2b) the internal field, created by the alignment of the energy levels of the metal top electrode and the ITO-PEDOT:PSS, assists in separation and transport of charges towards the opposite electrodes.

4.2 Characterization of the solar cell performance

When a photovoltaic device is measured by sweeping the voltage and reading out the current, under illumination a typical current density (J) – voltage (V) curve is obtained as is shown in figure 4.3a.

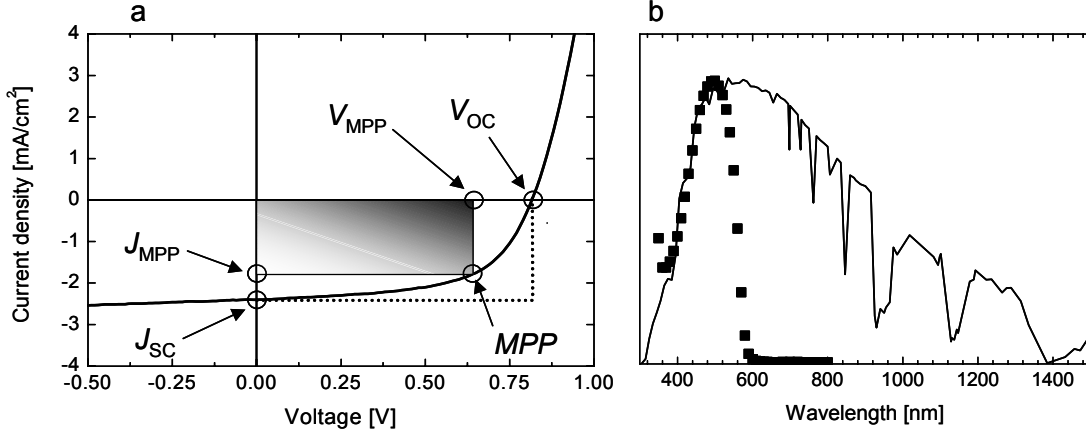


Figure 4.3 a) Current density – voltage plots of a photovoltaic device under illumination, indicating several parameters that are important to characterize the photovoltaic effect. b) AM1.5(G) solar emission spectrum (solid curve), co-plotted with an absorption spectrum of MDMO-PPV (■).

Several characteristic parameters for the performance can be observed in such a J - V plot. The intersection of the curve with the vertical axis gives the short-circuit current density (J_{SC}), the intersection with the horizontal axis gives the open-circuit voltage (V_{OC}). At one point between $V = 0$ and $V = V_{OC}$, the electrical power, or product $J \times V$ is maximal. This is the so-called maximum power point (MPP). The MPP in figure 4.3a is displayed by the lower right corner of the shaded area. The fill factor (FF) is defined as:

$$FF = \frac{J_{MPP} \times V_{MPP}}{J_{SC} \times V_{OC}} \quad (1)$$

This fill factor is the ratio of the shaded area over the one bounded by J_{SC} and V_{OC} , indicated by the dotted line. The efficiency (η) of the device is calculated using:

$$\eta = 100 \times \frac{P_{out}}{P_{incident}} = 100 \times \frac{FF \times J_{SC} \times V_{OC}}{P_{incident}} \quad (2)$$

$P_{incident}$ is the power of the incident light expressed in mW cm^{-2} , and the current density J_{SC} is expressed in mA cm^{-2} . If the incident power of the light source is known, the efficiency can be calculated. This however is not a relevant number as the only meaningful light source for a solar cell would be the sun itself. The emission from the sun is standardized within the so-called AM1.5 emission spectrum, see figure 4.3b. The AM1.5 (Air mass 1.5) spectrum is defined as the emission at the Earth's surface with the sun at an angle of 41.8° above the horizon. The standard intensity is set as 100 mW cm^{-2} . Accurate determination of the standard AM1.5 efficiency requires an AM1.5 solar simulator, and a calibrated photodiode as a reference cell. A correction is needed for the spectral

mismatches between the reference cell, the device under observation, the emission spectrum of the simulator and the AM1.5 spectrum. This elaborate procedure has been described in the literature for polymer-organic photovoltaic devices¹⁰. An alternative procedure, used in this thesis, is to evaluate the AM1.5 current of the solar cell under investigation, by measuring the incident photon to current conversion efficiencies (IPCE) of the solar cell. These IPCE values are the monochromatic efficiencies of the cell, showing the ratio of collected electrons in the external circuit over the number of incident photons per wavelength measured under short circuit conditions:

$$IPCE(\lambda) = \frac{n_{electrons}}{n_{photons}} \Big|_{\lambda} \times 100\% = 1240 \times \frac{J_{SC}(\lambda)}{P(\lambda) \times \lambda} \times 100\% \quad (3)$$

J_{SC} is the current density (mA cm^{-2}) of the device under illumination with light of wavelength λ , $P(\lambda)$, is the power (mW cm^{-2}) of the monochromatic light. The ratio $J_{SC}(\lambda)/P(\lambda)$, is often called the spectral response (A W^{-1}) of the solar cell. Figure 4.3b also shows the absorption spectrum of MDMO-PPV. Few things are immediately striking: this type of conjugated polymer only harvests a small fraction of the solar emission. For this reason the maximum performance that can be obtained under solar illumination is rather low. The mismatch between the solar emission spectrum and the absorption spectrum of MDMO-PPV makes these cells difficult to compare when using different light sources. By choosing a light source with an emission maximum close to 500 nm this solar cell would operate quite efficiently.

In an attempt to simplify the method for efficiency calculation but still reach reliable values, the current density of this solar cell under AM1.5 conditions (J_{SC} at 1 sun intensity), can be obtained from the integration of the spectral response with the AM1.5 solar emission spectrum:

$$J_{SC}(1 \text{ sun}) = \int \frac{J_{SC}(\lambda)}{P(\lambda)} (A/W) \times E_{AM1.5}(W/cm^2 \text{ nm}) d\lambda \quad (4)$$

The ‘equivalent AM1.5 intensity’ of the light source that has been used to obtain the J - V characteristics as shown in figure 4.3a can be calculated using the measured J_{SC} of the device under this light source. This ‘equivalent AM1.5 intensity’ equals: $I = I(1 \text{ sun}) \times [J_{SC}/J_{SC}(1 \text{ sun})]^{1/n}$, where $I(1 \text{ sun})$ is the standard intensity for AM1.5 conditions (100 mW cm^{-2}). With $n = 1$ no correction for the sub-linear response of the short circuit current density to the light intensity is performed. A correction for the sub-linear response of the short-circuit current density to the light intensity can be performed; this procedure is followed in section 4.7. Without correction, this leads to a small underestimation of the intensity of the light source, and therefore to a small overestimation of the efficiency of the device. Provided that the J - V characteristics shown in figure 4.3a are measured close to the 1 sun equivalent intensity the measured FF and V_{OC} can be combined with the calculated intensity of the light source (I) to obtain a close estimate of the AM1.5 efficiency, using $\eta = 100 \times (J_{SC} \times V_{OC} \times FF)/I$.

4.3 Observation of a photovoltaic effect in bulk heterojunction solar cells from ZnO nanoparticles and MDMO-PPV

MDMO-PPV is very well soluble in chloroform and a blend of this conjugated polymer with ZnO nanoparticles can be prepared. The procedure followed for the synthesis of blends from ZnO nanoparticles and MDMO-PPV is described in detail in the experimental section. The volume percentage of ZnO in the blend is calculated using a relative density of 5.6 g cm^{-3} for the ZnO and 0.91 g cm^{-3} for the MDMO-PPV¹¹. A device as shown in figure 4.1b has been constructed using an *nc*-ZnO:MDMO-PPV blend (35 vol.-% ZnO) as the photoactive layer. This blend has been cast from a chloroform solution with a small amount of methanol to stabilize the ZnO nanoparticles. The J - V characteristic of this device, under illumination and in the dark is shown in figure 4.4. A significant photovoltaic effect is observed, this shows that the application of ZnO and MDMO-PPV in photovoltaic devices is interesting to investigate.

In the following sections, a detailed analysis of photovoltaic devices based on *nc*-ZnO:MDMO-PPV blends will be discussed after an initial screening of relevant parameters. An optimized *nc*-ZnO:MDMO-PPV hybrid polymer solar cell is described and characterized in section 4.7. The application of ZnO nanorods is explored in section 4.9, and replacing the MDMO-PPV with regio-regular poly(3-hexylthiophene) is explored section 4.10.

4.4 Initial screening of relevant parameters

This section deals with the identification of the relevant parameters, like the choice of solvent and the amount of ZnO. The initial results on solar cells made using chloroform as the solvent (with a small fraction of methanol) are shown in table 4.1. Increasing the amount of ZnO in the blend from 15 to 35 vol.-% led to an improvement of the short circuit current and FF , but to a loss in V_{OC} . The reproducibility of these results was however not acceptable. Due to this solvent's high volatility, spin casting of *nc*-ZnO:MDMO-PPV blends from chloroform into smooth, homogeneous films was rather challenging.

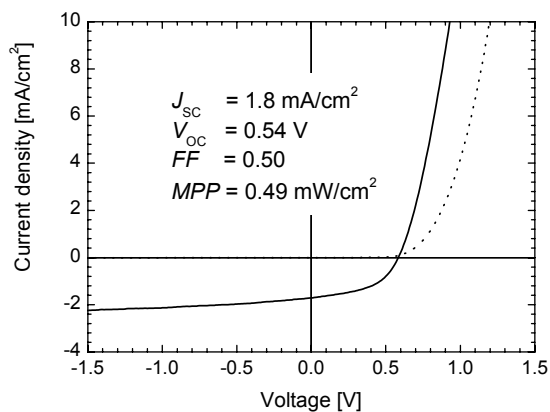


Figure 4.4 An early example of a hybrid polymer solar cell constructed from MDMO-PPV and *nc*-ZnO (35 vol.-%), the solid curve has been measured under illumination, the dotted curve in the dark.

Table 4.1 Initial results exploring the effect of solvent and the LiF interfacial layer. Solvents used: CB = chlorobenzene, CHCl₃ = chloroform

Nr.	Solvent	Vol.- % ZnO	<i>L</i> [nm]	LiF	<i>J</i> _{sc} [mA cm ⁻²]	<i>V</i> _{oc} [V]	<i>FF</i>	<i>MPP</i> [mW cm ⁻²]
1	CHCl ₃	15	70	yes	0.67	0.84	0.41	0.23
2	CHCl ₃	26	100	yes	1.39	0.72	0.46	0.46
3	CHCl ₃	35	130	yes	1.78	0.59	0.49	0.51
4	CHCl ₃	42	125	yes	1.64	0.55	0.48	0.43
5	CHCl ₃	47	180	yes	0.89	0.34	0.43	0.15
6	CB	35	300	no	2.66	0.66	0.43	0.75
7	CB	35	125	no	2.51	0.65	0.54	0.88
8	CHCl ₃	35		yes	1 - 1.8	0.2 - 0.6	~ 0.50	0.1 - 0.5
9	CHCl ₃	35		no	1.3 - 1.8	> 0.5	> 0.50	0.3 - 0.5
10	CB	35	> 125	yes	2 - 2.25	~ 0.71	~ 0.40	0.6
11	CB	35	> 125	no	~ 2.1	~ 0.77	~ 0.41	0.7

Changing the solvent to chlorobenzene, led to devices with higher short circuit currents and open-circuit voltages. In general, spin casting from chlorobenzene also improved the reproducibility of the photovoltaic effect. Even very thick blend layers showed a nice photovoltaic response, see entry 6, but these films were very inhomogeneous, and the results were difficult to reproduce. The effect of a thin (1 nm) layer of LiF in-between the active blend layer and the Al top electrode has also been tested, because in bulk heterojunction PCBM:MDMO-PPV solar cells a LiF layer improves the performance¹². Cells made using chloroform as solvent, with an added LiF layer, showed a wide variation of open-circuit voltages. Without LiF the reproducibility of these solar cells seemed better. Cells from chlorobenzene with an additional LiF layer showed a less pronounced effect of the LiF. Simultaneous experiments performed on these cells (shown in entries 10 and 11) gave a slightly higher open circuit voltage without LiF.

The higher photovoltaic effect that has been found when using chlorobenzene as solvent, combined with the improved reproducibility shows that chlorobenzene is the best choice for optimization of the photovoltaic effect. The effect of LiF is not clear, but at least the irreproducibility of the chloroform-based solar cells partially can be attributed to the LiF. The LiF effect on the chlorobenzene-based cells is less pronounced. Because no real improvement has been observed, the LiF layer has not been used in further explorations of the photovoltaic effect of this hybrid type of solar cell. When considering injection barriers, an effect of LiF is also not expected. The conduction band level for ZnO at 4.4 eV, likely leads to an Ohmic contact with aluminum, which has a workfunction of 4.3 eV.

4.5 Effect of the layer thickness and vol.-% ZnO on the photovoltaic performance

Photovoltaic devices have been investigated recording the J - V characteristics of nc -ZnO:MDMO-PPV hybrid solar cells, as a function of the amount of ZnO and the thickness of the active blend layer. The experiments have been performed in a short period of time to rule out variations in performance, due to changes in the surrounding atmosphere¹³. The effect of the vol.-% ZnO and the layer thickness on the maximum power point (MPP) is shown in figure 4.5. This MPP has been measured under illumination from a 100 W tungsten-halogen lamp filtered by a Schott KG01 and GG420 filter. The maximum performance has been observed for devices containing 26 to 35 vol.-% ZnO, and having a thickness between 100 and 150 nm. Devices containing higher amounts of ZnO (47 vol.-%) appear to have their optimal performance at higher layer thickness.

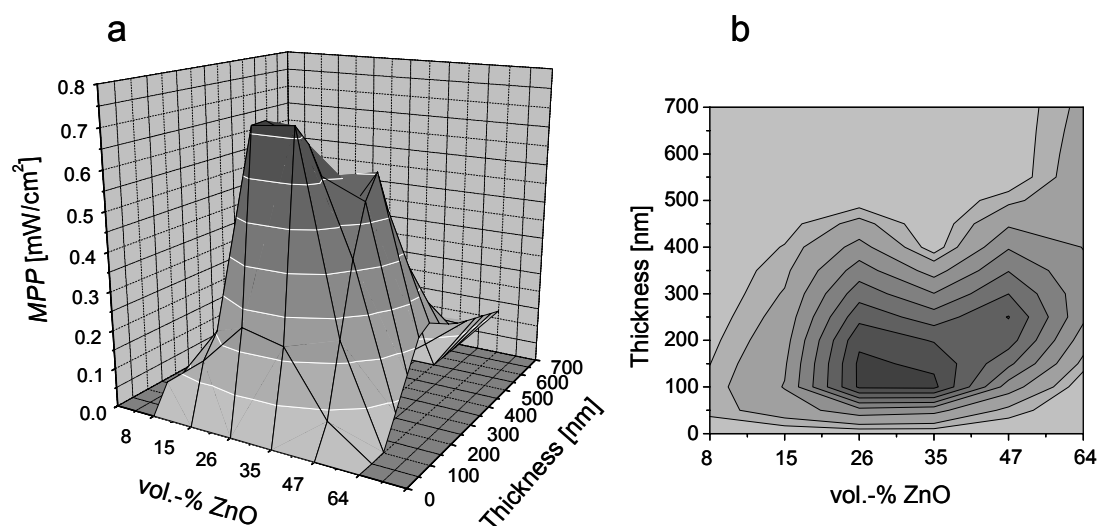


Figure 4.5 The maximum power point (MPP) of nc -ZnO:MDMO-PPV solar cells, as a function of vol.-% ZnO and the thickness of the active layer. a) Shows a 3 dimensional representation and (b) a top view of the same image.

For a relevant comparison the J - V characteristics of solar cells with the same layer thickness should be compared, see figure 4.6. This figure shows the J - V characteristics for devices having different vol.-% of ZnO but with a layer thickness of approximately 100 nm. From figure 4.6a it is clear that V_{OC} drops with increasing amounts of ZnO. This might be related to the formation of shunts; relative conducting pathways of ZnO particles from electrode to electrode, whose likelihood increases when the amount of ZnO increases. It is indeed observed (data are not shown) that with the same amount of ZnO in the blend, an increase in the layer thickness results in an increase of V_{OC} . This is attributed to a higher shunt resistance within thicker active layers. The short circuit current initially increases when the amount of ZnO in the blend has been increased. This trend is due to an increased formation of photoseparated charges, as is inferred from the photoluminescence quenching observed in these

blends (see chapter 5). An additional effect is the formation of ZnO rich domains that improve the transport of electrons throughout the device, therefore also increasing the observed photocurrent. Keeping the layer thickness constant, but increasing the amount of ZnO leads to a decrease of the effective MDMO-PPV absorption. This explains the decrease of the short circuit current at higher vol.-% of ZnO nanoparticles.

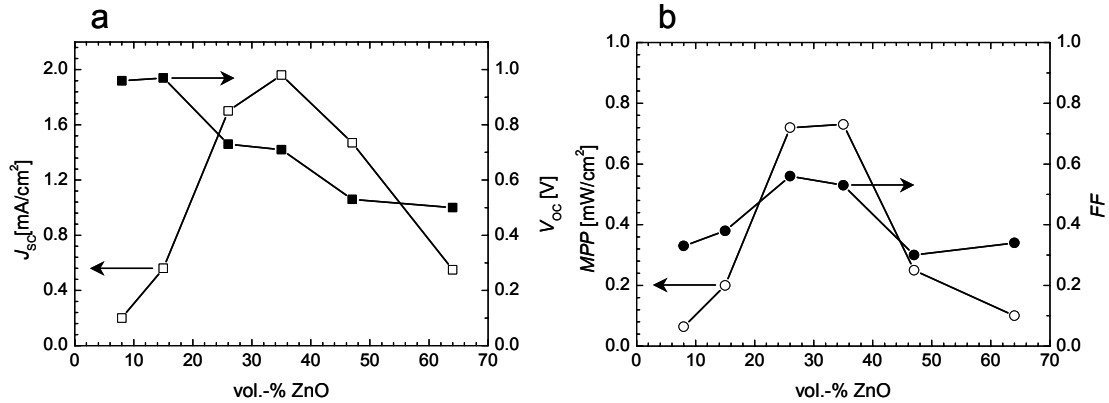


Figure 4.6 J - V characteristics from nc -ZnO:MDMO-PPV solar cells with an active layer thickness of 100 nm, showing the trends for J_{sc} and V_{oc} (a) and for the MPP and FF (b)

The FF ranges from 0.3 to 0.6 depending on the amount of ZnO in the blend. The observed maximum can be explained by reasoning that the FF is a measure for the balance between hole and electron transport. At low ZnO concentrations electron transport is poor, at high ZnO concentration the polymer phase is highly diluted and hole transport is poor. The low FF at a high vol.-% of ZnO can also be related to a low shunt resistance, which was also used to explain the trend in V_{oc} . When devices with the same vol.-% of ZnO, but varying layer thickness are compared the average trend is that the FF drops with increasing layer thickness. This trend can be related to a decrease of the internal field in the device that assists in the harvesting of charges. Close to the V_{oc} of the device, where the internal field is approximately zero, the effect of film thickness is more pronounced. In thick films a larger deviation of the applied voltage from V_{oc} is required to create an internal field that can assist in the collection of the photogenerated charges. However the internal fields in solar cells are rather low, which means that separation and transport of charges are almost independent of the applied field. More important is that in thicker films the likelihood for recombination increases, because the time for photogenerated electrons and holes to reach the electrodes increases with film thickness ($t = L^2/\mu V$). This increase in recombination leads to a lower FF .

The overall trend, when all is combined in the MPP , is that there is an optimal amount of ZnO of approximately 30 vol.-%, or 70 wt.-% ZnO. This amount is less than the optimal amounts mentioned for PCBM in PCBM:MDMO-PPV blends¹⁴ (80 wt.-%) and 90 wt.-% for CdSe nanoparticles and rods^{2,3} blended with rr -P3HT and MDMO-PPV.

4.6 Incident light power dependency measurements

The light intensity dependence of the J_{SC} , V_{OC} , FF , and efficiency have been determined for a series of nc -ZnO:MDMO-PPV (35 vol.-% ZnO) solar cells, having different layer thickness. The illumination intensity of the light source has been calculated from the IPCE of the solar cells using the procedure described in section 4.2.

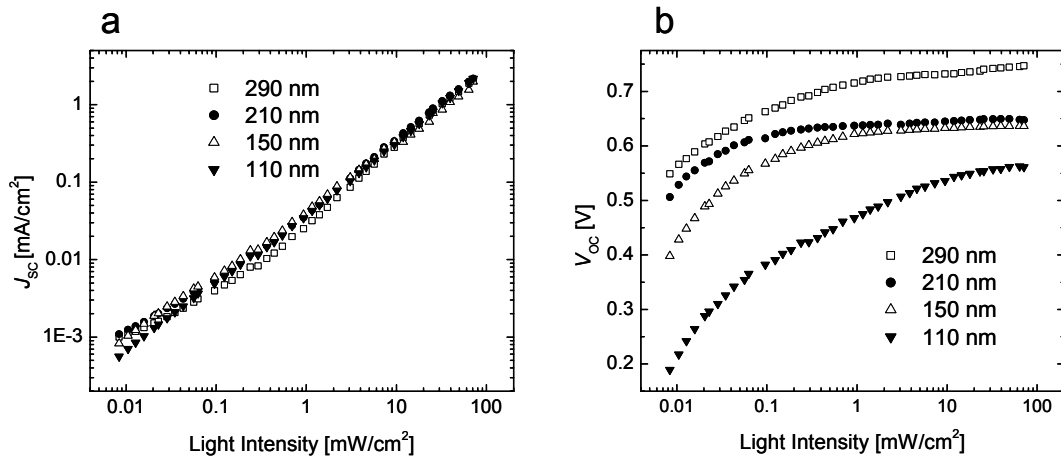


Figure 4.7 Incident light power dependence measurements performed on a nc -ZnO:MDMO-PPV device with 35 vol.-% of ZnO. Incident light power dependence of a) J_{SC} and b) V_{OC} , as a function of the active layer thickness.

The relation between the short circuit current and the light intensity (see figure 4.7a) is slightly sub-linear, $J_{SC} \propto I^n$, with the exponent $n = 0.9-0.92$. A linear relation would imply $n = 1$. This near linear relation implies that non-geminate recombination occurs to a minor extent in these photovoltaic devices¹⁵. V_{OC} (figure 4.7b) is dependent on the light intensity and on the layer thickness. The initial fast growth of the V_{OC} is due to the dark current. A small photocurrent in competition with a small dark current leads to a lower observed V_{OC} . For thicker layers, the saturation of V_{OC} seems to appear at lower light intensities. Because the dark currents are also smaller, the difference between the photocurrent and dark current for these thick films is larger at low intensities. Thin layers show a lower V_{OC} than thick films, possibly because the likelihood of shunts is higher.

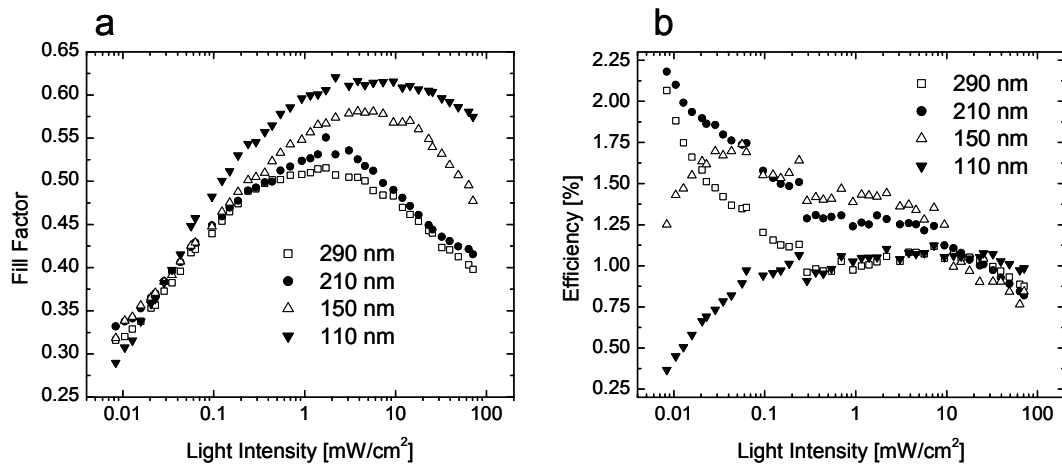


Figure 4.8 Incident light power dependence of a) FF and b) efficiency, as a function of the active layer thickness. The efficiency has been estimated from the incident light power, which has been calculated from the integration of the IPCE with the AM1.5 emission spectrum.

The trends observed for FF (figure 4.8a) show an initial increase of FF followed by a loss, which is more pronounced for thicker layers. Similar to the increase in V_{OC} , the initial increase of FF is explained by a larger difference between the photocurrent and the dark current. When thick active layers have been used in these solar cells, the loss in FF at high light intensities is detrimental for their energy conversion efficiency under ‘1 sun’ conditions (approximately 100 mW cm⁻²). As argued before, thicker films give devices with lower fill factors. The steep drop of the fill factor with light intensity observed for the thick devices is difficult to explain. One explanation might be an increase in the photoconductivity, which has also been observed for CdSe devices¹⁶. Upon increasing the thickness of *nc*-ZnO:MDMO-PPV active layer, at high illumination intensities, both a steeper J - V curve below the V_{OC} and above the V_{OC} have been observed. The effect of the photoconductivity below the V_{OC} might explain the drop in fill factor. In the thinner devices, the observed drop of the FF with increasing light intensity is not as pronounced as has been reported for CdSe nanorods based devices¹⁶. For the CdSe based photovoltaic devices the loss of the FF near AM1.5 conditions is detrimental for their photovoltaic effect. Using ZnO nanoparticles the drop in FF is only detrimental for the thick devices. The V_{OC} of the device with the thinnest active layer is lower than has in general been found for similar devices; the reported efficiency is therefore often higher than the ones observed in figure 4.8b.

4.7 Calculation of the AM1.5 performance of the optimized solar cell

From figure 4.4 it can be observed that the optimal performance appears around 30 vol.-% of ZnO in the active layer. The actual optimal ZnO content in most experiments appears to be 26 vol.-%, and the optimal thickness of the layer appears between 80 and 100 nm. The optimum amount of ZnO and the optimal layer thickness vary with processing conditions; temperature and humidity seem to have a profound effect on the film thickness and quality of the active layer. This section shows an optimized solar cell using 26 vol.-% of ZnO in a blend with MDMO-PPV. The film thickness was measured to be 80 nm.

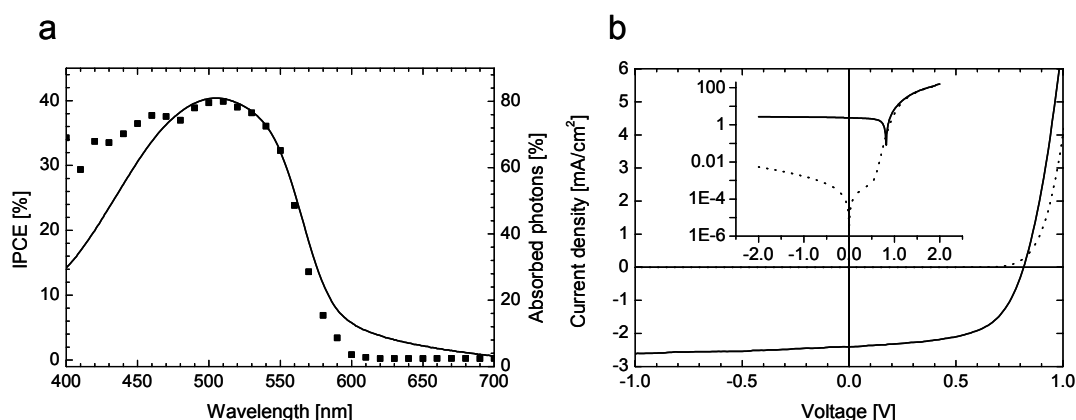


Figure 4.9 a) IPCE as function of the wavelength of monochromatic irradiation (■), co-plotted with the percentage of photons absorbed by the blend (solid curve). b) Current density voltage (J - V) characteristic of a nc -ZnO:MDMO-PPV blend (with 26 vol.-% ZnO). The dotted line is measured in the dark, the solid line under illumination with white light from a tungsten halogen lamp estimated at 0.71 sun equivalent intensity by integration of the quantum efficiency data shown in (a) with the AM1.5 solar emission spectrum. The inset shows the same data in a semi-logarithmic plot.

The incident photon to current conversion efficiencies of this solar cell (figure 4.9a) have been measured with white light bias illumination to create conditions resembling operation under solar illumination. The IPCE spectrum closely resembles the absorption spectrum of the nc -ZnO:MDMO-PPV layer on glass, and reaches a value of 40% at the absorption maximum of MDMO-PPV. Integration of this spectral response with the solar spectrum (AM1.5, normalized to 100 mW cm⁻²) affords an estimate of the short-circuit current density of $J_{SC} = 3.3 \text{ mA cm}^{-2}$ under AM1.5 (1 sun) conditions.

J - V measurements (figure 4.9b), carried out in the dark reveal excellent diode behavior, with a rectification ratio of 3×10^4 at $\pm 2 \text{ V}$. The forward current density through the nc -ZnO:MDMO-PPV layer is considerably higher than for pure MDMO-PPV in a similar device configuration, demonstrating that the electron current is likely to dominate the current density in forward bias. This supports the presence of a continuous pathway for electron transport through the nc -ZnO network.

The J - V curve, measured with white-light illumination using a tungsten-halogen lamp, is shown in figure 4.9b. Under these conditions $J_{SC} = 2.40 \text{ mA cm}^{-2}$ has been obtained, together with $V_{OC} = 814 \text{ mV}$ and $FF = 0.59$.

Light intensity dependent J - V measurements, using a tungsten halogen white-light lamp and a set of neutral density filters, show a sublinear relation between the light intensity (I) and J_{SC} : $J_{SC} \propto I^n$, with $n = 0.93$ (figure 4.10). This near linear relation implies only minor bulk (non geminate) charge carrier

recombination occurs in these photovoltaic devices. Upon increasing the illumination power, the open-circuit voltage (V_{OC}) continuously improves, ultimately reaching values over 800 mV, while the fill factor (FF) increases up to values close to 0.6. At the highest light intensities measured, FF begins to decrease slowly, due to increasing resistive losses.

The efficiency of this device under ‘1 sun’ conditions is estimated using the procedure described in section 4.2. The intensity of the light source (I) is calculated using the formula: $I = I(1 \text{ sun}) \times [J_{SC}/J_{SC}(1 \text{ sun})]^{1/n}$ with $n = 0.93$. $J_{SC}(1 \text{ sun})$ is the current density under 1 sun conditions (3.3 mA cm^{-2}), and J_{SC} the obtained current density under the light source. This way the intensity of the light source is corrected for the small nonlinearity of the intensity dependence. The calculated intensity is 0.71 sun equivalents (equivalent to 71 mW cm^{-2}), for this combination of active material and light source. Using this intensity, an overall power conversion efficiency (η) of 1.6% has been estimated. At 1 sun equivalent no dramatic decrease of this efficiency is expected, in view of the evolution of the photovoltaic parameters with increasing light power. Confirmation has been obtained by a single measurement at 1.7 sun equivalent ($J_{SC} = 5.40 \text{ mA cm}^{-2}$; $V_{OC} = 844 \text{ mV}$; $FF = 0.53$; $\eta = 1.4\%$). The lower fill factor is partly compensated by an increased open circuit voltage. An estimation for the maximum power conversion of a *nc*-ZnO:MDMO-PPV device can be obtained following a theoretical calculation as has been performed by Coakley and McGehee^{17,18}. Using an organic LUMO - acceptor level energy difference of 1.4 eV (as for MDMO-PPV and ZnO), and a bandgap of 2.3 eV (MDMO-PPV) a maximum power conversion efficiency of approximately 7% can be obtained. The actual maximum efficiency is likely much lower because FF and V_{OC} in this case were assumed to be 1 and 0.9 V respectively. Correcting for the actually measured FF and V_{OC} gives an upper limit of 3.7% for

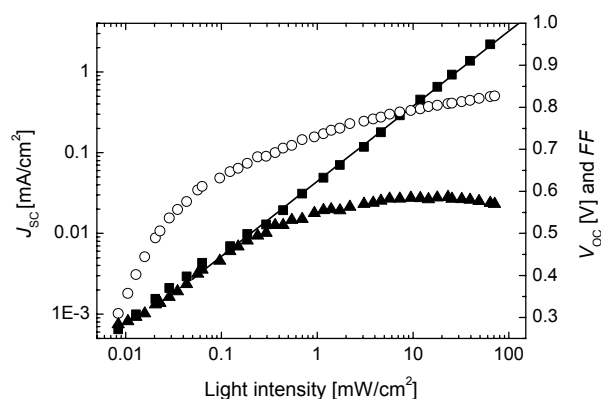


Figure 4.10 Evolution of short circuit current density (J_{SC} , squares) with least-squares fit of power-law behavior (solid line), open circuit voltage (V_{OC} , open circles), and fill factor (FF , triangles) as a function of light intensity.

the maximum power conversion of this solar cell. A rough estimate of the internal quantum efficiency (IQE, showing the number of collected electrons per absorbed photons) of this device is approximately 50% see figure 4.9a. This corresponds well to the difference between the maximum theoretical efficiency (3.7%, assuming IQE = 100%) and the measured efficiency of 1.6%. The estimated efficiency of approximately 1.6% is comparable to the highest efficiency reported for a hybrid-conjugated polymer device. CdSe tetrapods, i.e. branched nanorods, mixed with MDMO-PPV have shown a measured 1.8% AM1.5 efficiency, see table 4.2.

Table 4.2 Comparison of the photovoltaic performance of the *nc*-ZnO:MDMO-PPV device with relevant other polymer based bulk heterojunction solar cells. The IPCE maximum for all devices has been observed at a monochromatic illumination with a wavelength of approximately 500 nm.

	J_{SC} (mA cm ⁻²)	V_{OC} (V)	FF	η AM1.5 (%)	IPCE max (%)
<i>nc</i> -ZnO:MDMO-PPV	3.3	0.81	0.59	1.6	40
TiO ₂ : <i>rr</i> -P3HT ¹⁹	2.8	0.44	0.36	0.4	15
CdSe rods: <i>rr</i> -P3HT ²	5.7	0.70	0.40	1.7	55
CdSe tetrapods:MDMO-PPV ²⁰	7.3	0.65	0.35	1.8	44
C ₆₀ PCBM:MDMO-PPV ¹⁰	4.9	0.87	0.60	2.6	50
C ₇₀ PCBM:MDMO-PPV ²¹	7.6	0.77	0.51	3.0	65
C ₆₀ PCBM: <i>rr</i> -P3HT ¹	15.0	0.55	0.47	3.9	75

The *nc*-ZnO:MDMO-PPV devices outperform all other hybrid devices in terms of their FF and V_{OC} . The challenge still remains to improve the J_{SC} , because compared to the devices made from CdSe and fullerenes the obtained J_{SC} is rather low. Because the CdSe rods and tetrapods show a high J_{SC} that is much higher than has been reported for CdSe nanoparticles, the application of ZnO nanorods seems a logical step towards an improvement of the photovoltaic effect. In general the application of rods is thought to lead to an improved transport of electrons through the nanoparticulate network, because less electron hopping between individual nanoparticles is needed to bridge the distance to the collecting electrode.

4.8 Investigation of surfactant effects and application of ZnO nanorods

As explained in chapter 3, addition of a small amount of amines led to very stable solutions of ZnO nanoparticles in organic solvents. Even very small molecules like *n*-propylamine appear very effective. In general, application of surfactants in photovoltaic devices based on nanoparticles is unfavorable because they hamper the electron transfer process over the interface between the nanoparticle and the polymer, and the conductivity of the percolating nanoparticle network. Because *n*-propylamine is such a small molecule, effects like these may be negligible. The homogeneity of *nc*-ZnO:MDMO-PPV blends is often limited and very sensitive to the conditions during spincoating. After addition of *n*-propylamine to the nanoparticle solution, films made from these mixtures appear completely smooth by eye. This major improvement of film quality and reproducibility might result in better photovoltaic devices. Table 4.3 summarizes experiments performed on several cells made using *n*-propylamine (entries 1-5).

Table 4.3 Summarized results on solar cells made using *n*-propylamine (PA), ZnO nanoparticles and nanorods. Solvents used: CB = chlorobenzene, CHCl₃ = chloroform. The vol.-% *n*-propylamine is the amount added to the stock ZnO nanoparticle solution.

Nr.	Solvent	Spin Speed (rpm)	Vol.-% ZnO		Vol.-% PA	J_{sc} [mA cm ⁻²]	V_{oc} [V]	FF	MPP [mW cm ⁻²]
1	CB	1500	26		0	2.46	0.78	0.58	1.1
2	CB	1500	26		0.5	2.1 - 2.2	0.6 - 0.7	0.50	0.7
3	CB	1500	8		2	1.1	0.78	0.48	0.4
4	CB	1500	26		2	1.5 - 1.6	0.6 - 0.7	0.59	0.6
5	CB	1500	35		2	1.9 - 2.1	0.64	0.55	0.7
6	CB	1000	26	rods	4	1.4	0.54	0.58	0.4
7	CB	1500	26	rods	4	1.1	0.52	0.62	0.4
8	CB	1000	35	rods	4	1.6	0.50	0.59	0.5
9	CB	1500	35	rods	4	1.2	0.47	0.61	0.3
10	CHCl ₃	1500	26		2	1.6	0.65	0.52	0.5
11	CHCl ₃	2000	26		2	1.3	0.64	0.51	0.4
12	CHCl ₃	1500	26	rods	2	1.7	0.56	0.53	0.5
13	CHCl ₃	2000	26	rods	2	1.6	0.56	0.53	0.5

J_{sc} and V_{oc} of the solar cells decrease when the amount of *n*-propylamine in the ZnO sol is increased from 0.5 to 2 vol.-%. The short circuit current can be slightly restored by increasing the amount of ZnO. Unfortunately, the addition of more ZnO leads to a lower V_{oc} . Even though addition of *n*-propylamine improves the film forming properties of the blend, it does not lead to an improved performance of the solar cell. The effect on the current density indicates that charge separation might be hampered by the introduction of *n*-propylamine.

As discussed in chapter 3, ZnO nanorods of approximately 25 nm in length, can be prepared by heating a concentrated ZnO nanoparticle solution for 15 hours. For longer-term stability of these rods in organic solvents some *n*-propylamine is necessarily. Even with 4 vol.-% of *n*-propylamine these rods give barely stable solutions in chlorobenzene. Solar cells made from these rods (entries 6-9, table 4.3), do give a photovoltaic effect, but the J_{SC} and V_{OC} are reduced compared to the best nanoparticle based devices. Solubility of ZnO nanorods in chloroform can be achieved with smaller amounts of *n*-propylamine and the solutions show an improved long-term stability. Photovoltaic devices, prepared from rod and nanoparticle solutions in chloroform with the same amount of *n*-propylamine, have been compared to investigate the influence of the shape of the particle. Table 4.3 (entries 10-13), reveals only minor differences in the performance of photovoltaic devices made using rods and nanoparticles. In conclusion, photovoltaic devices with ZnO nanorods can be prepared, but for a full utilization of the advantages of these rods, solubility in organic solvents without the application of surfactants is demanded.

For the *nc*-ZnO:MDMO-PPV solar cells ZnO nanoparticles have been used that were synthesized as described in chapter 3, using a $Zn^{2+}:OH^{-}$ ratio of 1:1.7. A few solar cells have been made with smaller nanoparticles made using a ratio of 1:1.85, *i.e.* decreasing the size of the ZnO nanoparticles. The size of these nanoparticles as determined from their UV absorbance was 3.7 nm. TEM explorations of their size were inconclusive, only indicating very small, but not nicely monodisperse particles have been formed. Surprisingly, when introduced in MDMO-PPV, these nanoparticles gave very nice photovoltaic devices. IPCE values up to 50% (at 520 nm) have been measured. Using the IPCE a 1 sun equivalent short circuit current density of 3.9 mA cm^{-2} has been obtained, combined with the V_{OC} and FF of 0.8 and 0.5 (measured at 0.78 sun equivalents) this leads to a photovoltaic device with an efficiency of 1.56%. The remarkable high current indicates that the size of the nanoparticles might be important for further optimization of the solar cell performance. Increasing the size of the nanoparticles, or the application of nanorods might not necessarily be the only way to improve charge transport.

4.9 Degradation of the *nc*-ZnO:MDMO-PPV solar cell performance by UV illumination

One potential drawback of this material combination in a hybrid solar cell is its sensitivity towards UV illumination. For stable J - V measurements a 420 nm cutoff filter has to be placed between the cell and the light source. If only a 380 nm filter is used to eliminate UV illumination from the halogen light source (figure 4.11a), the open circuit voltage drops in consecutive measurements. Longer illumination times, even with small amounts of UV light, lead to a complete loss of V_{OC} .

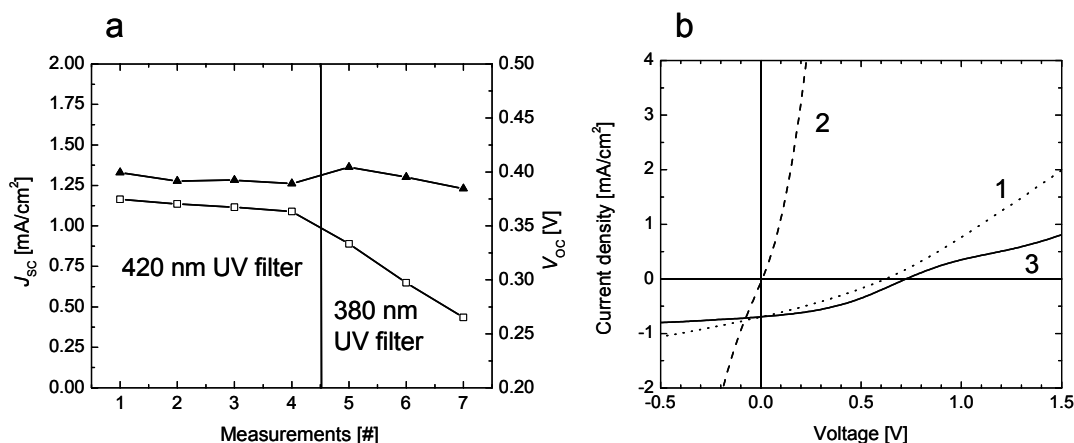


Figure 4.11 The effect of UV illumination on the performance of *nc*-ZnO:MDMO-PPV solar cells. a) *nc*-ZnO:MDMO-PPV solar cell spin cast from chloroform as solvent, with 35 vol.-% ZnO, indicating the effect of consecutive measurements on the short circuit current (▲, left axis) and open circuit voltage (□, right axis). b) An *nc*-ZnO:MDMO-PPV solar cell with a 600 nm thick active layer containing 64 vol.-% ZnO in MDMO-PPV. Curve 1 shows the initial solar cell performance. Curve 2 shows the same cell after short time UV illumination, and curve 3 after exposure to air for 1 minute.

The effect of UV illumination has been investigated for a device containing a thick layer of a blend with 64 vol.-% ZnO in MDMO-PPV (figure 4.11b). The J - V characteristics before UV exposure (curve 1) indicate a J_{SC} and a V_{OC} of 0.7 mA cm⁻² and 0.62 V for this device. Illumination using a halogen light source without any UV filter leads within seconds to a complete loss of the V_{OC} , J_{SC} , and the diode behavior. Instead, the layer acts as a conductor. Exposing this solar cell to air for one minute restores J_{SC} and even slightly improves V_{OC} . This remarkable recovery effect can be related to the observations for ZnO nanoparticles in chapter 3. By UV illumination of the ZnO nanoparticles these are directly excited across the band gap. For ZnO this produces a mobile electron in the conduction band and a deeply trapped hole. As a result, the dark conductivity increases dramatically and the photovoltaic effect is lost. Exposure to oxygen removes the electrons from the conduction band, and restores the semiconducting properties of the material.

4.10 Application of regio-regular poly(3-hexylthiophene) in hybrid solar cells.

Regio-regular poly(3-hexylthiophene) (*rr*-P3HT) has some advantages over MDMO-PPV for application in photovoltaic devices. Due to their regio-regularity, stacking of chains in solid state is possible. This stacking has a profound effect on their electrical and optical properties. High hole mobilities of $0.1 \text{ cm}^2 \text{ V}^{-1} \text{ s}^{-1}$ have been observed in highly ordered poly(3-hexylthiophene)²². The enhanced planarity in stacks of *rr*-P3HT increases the effective conjugation length of the π -electron system. This leads to a profound shift of the absorption towards the red part of the solar emission spectrum, *i.e.* the material acts as a lower-bandgap absorber. Regio-regular poly(3-hexylthiophene) has been used in this study because it shows high solubility in organic solvents, which makes this material suitable for solution casting. Photovoltaic devices can be prepared using chloroform as solvent for both the *rr*-P3HT and the ZnO nanoparticles. The improvement observed for MDMO-PPV by the introduction of chlorobenzene does not apply to *rr*-P3HT, no working solar cells could be made using chlorobenzene as solvent. Compared to chloroform, the high boiling chlorobenzene slows down the film-forming process. This leaves more time for the ZnO nanoparticles and the *rr*-P3HT to phase separate, leading to very coarse, and shunted films. However, also solar cells made using chloroform as solvent show large fluctuations in the observed photovoltaic effect. The more volatile chloroform makes spin casting from this solvent difficult and not very reproducible. The amount of methanol in the solution is critical because too high amounts induce precipitation of *rr*-P3HT.

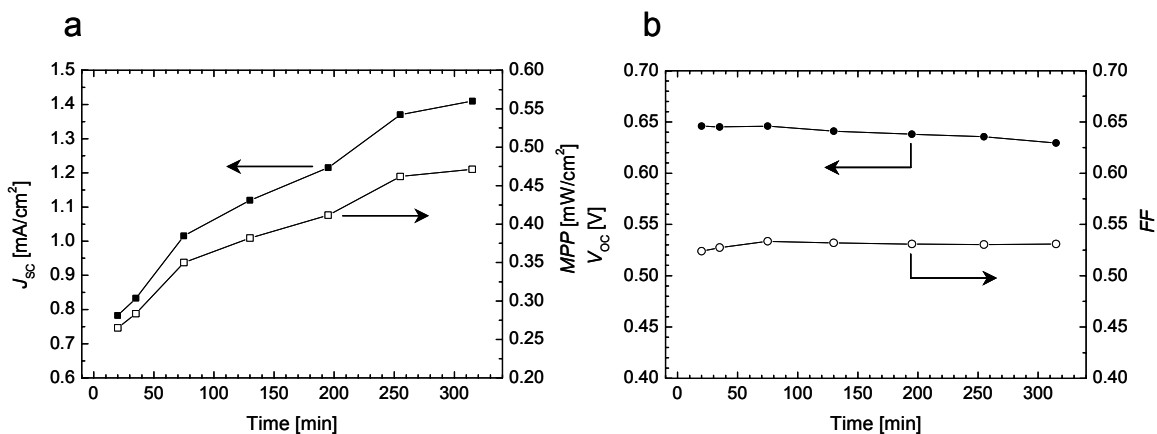


Figure 4.12 Time dependence of the photovoltaic effect of a *nc*-ZnO:*rr*-P3HT device with 35 vol.-% ZnO and a 150 nm thick active layer. a) Shows the time dependence of J_{sc} (left axis) and the MPP (right axis). b) shows the time dependence of V_{oc} (left axis) and the FF (right axis).

Solar cells made using chloroform show an evolution of the photovoltaic effect with time (figure 4.12). The short circuit current increases, while the V_{oc} and FF remain approximately constant. After 1 day both the short circuit current and the efficiency double. Morphology changes or a better stacking of the P3HT chains are likely responsible for this effect. The trends shown in figure 4.12 were not always this pronounced. In a few occasions, J_{sc} is directly after evaporation of the top metal

at its higher value without a significant evolution with time. There appears to exist an equilibrium state for the morphology the *nc-ZnO:rr-P3HT* blend. Due to the fast evaporation of the solvent (chloroform) this equilibrium is in most cases not immediately reached and a time effect can be observed.

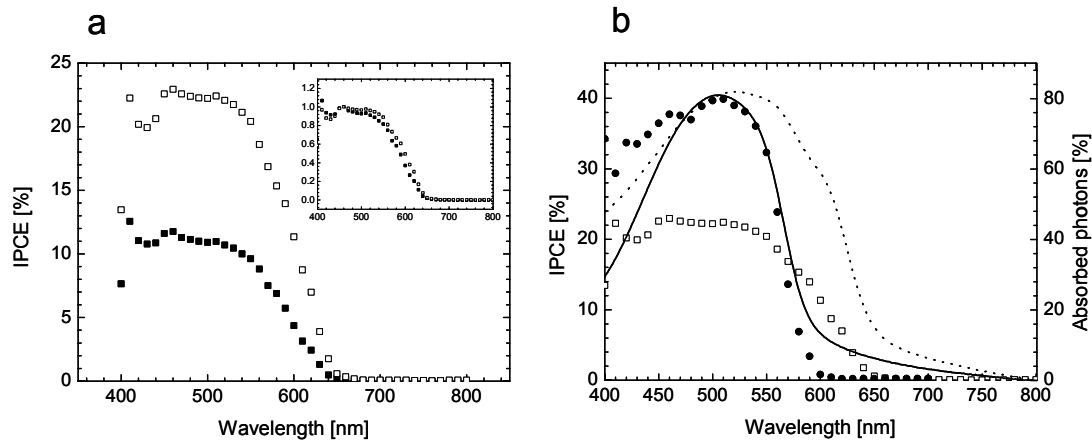


Figure 4.13 a) IPCE as function of the wavelength of monochromatic irradiation for a *nc-ZnO:rr-P3HT* device with 26 vol.-% ZnO. The lower curve is the IPCE spectrum of the un-annealed cell, the upper curve after annealing at 80 °C for 1 minute. The inset shows the normalized spectra. b) IPCE spectra of a 150 nm thick *nc-ZnO:rr-P3HT* device (\square) and an 80 nm thick *nc-ZnO:MDMO-PPV* device (\bullet), both with 26 vol.-% ZnO, co-plotted with the percentage of photons absorbed by the *nc-ZnO:rr-P3HT* device (dotted curve) and *nc-ZnO:MDMO-PPV* device (solid curve).

IPCE spectra of an optimized *nc-ZnO:rr-P3HT* solar cell are shown in figure 4.13a. A 150 nm thick photoactive blend with 26 vol.-% ZnO in *rr-P3HT* has been sandwiched between PEDOT:PSS and aluminum electrodes. Initially this leads to solar cells with $J_{SC} = 1.1 \text{ mA cm}^{-2}$, $V_{OC} = 0.69 \text{ V}$ and $FF = 0.54$, under a estimated 1.07 sun equivalents. The intensity of the light source has been estimated from the IPCE spectrum. The lower spectrum shown in figure 4.13a is the IPCE of an as-made cell, which has been measured directly after electrode evaporation. The evolution with time as shown in figure 4.12 also occurs when this cell is heated for 1 minute at 80 °C. The IPCE values double due to this annealing step, leading to the upper spectrum shown in figure 4.13a. The inset shows normalized spectra, indicating that the increase in current is not due to a change in absorption onset. This implies that a better stacking of the P3HT chains, often observed after annealing of P3HT films, is not likely the cause for this increase in current. By annealing, the short circuit current density increases to 2.76 mA cm^{-2} , and $V_{OC} = 0.69 \text{ V}$ and $FF = 0.54$ are obtained. Integration of the IPCE spectrum with the AM1.5 emission spectrum gives a J_{SC} at 1 sun of 2.58 mA cm^{-2} and an estimated AM1.5 efficiency of 1%. Figure 4.13b compares the IPCE of a cell made from *rr-P3HT* and MDMO-PPV. The advantage of *rr-P3HT* over MDMO-PPV is the gain of absorption at wavelengths higher than 600 nm. Comparison of the absorption spectra of the solar cells (figure 4.13b) reveals that at the absorption

maximum approximately 80% of the incident photons have been absorbed in both materials²³. In a first approximation, the IPCE values can be converted into internal quantum efficiencies (IQE) by dividing by the percentage of absorbed photons. In this approximation, the IQE of a *nc*-ZnO:MDMO-PPV solar cell is 50% and that of *nc*-ZnO:*rr*-P3HT is 25%. The advantage of the more red-shifted absorption of the *rr*-P3HT is lost by the lower IQE.

4.11 Charge carrier transport in *nc*-ZnO:MDMO-PPV blends

In order to obtain an indication of the electron mobility in the *nc*-ZnO:MDMO-PPV solar cells, their *J-V* characteristics have been measured in the dark. Measurement of the electron mobility from the *J-V* curves can only be performed when a few conditions are fulfilled. First, the observed current must be dominated by the electron current through the device. Second, the assumption of space charge limited current must hold.

A double logarithmic *J-V* plot of a 230 nm thick *nc*-ZnO:MDMO-PPV blend (26 vol.-% ZnO) is shown in figure 4.14. The voltage over the device has been corrected for the built-in voltage (V_{BI}) and for a voltage loss over the series resistance (V_{SR}) caused by the ITO and PEDOT:PSS layers. In these solar cells the aluminum top electrode, with a work function of 4.3 eV, allows injection of electrons into the conduction band of the ZnO, see figure 4.2a. The current shown in figure 4.14 drops by two decades when instead of aluminum, palladium is used as top electrode²⁴. Palladium, with a work function of 5.2 eV⁹, induces a barrier for electron injection into ZnO, but does not block the

hole transport through the device. The much higher dark current observed for aluminum top electrodes gives evidence that the current in figure 4.14 is indeed dominated by electron transport. Space charge limited (SCL) currents are expected when bulk mobilities are low, and minor injection barriers are present at the electrodes. As can be seen in figure 4.2, the contacts at the aluminum and PEDOT:PSS interface are almost Ohmic. For a space charge limited current the slope of the current density versus voltage in a double logarithmic plot (figure 4.14) should be 2. The found value of 3.5

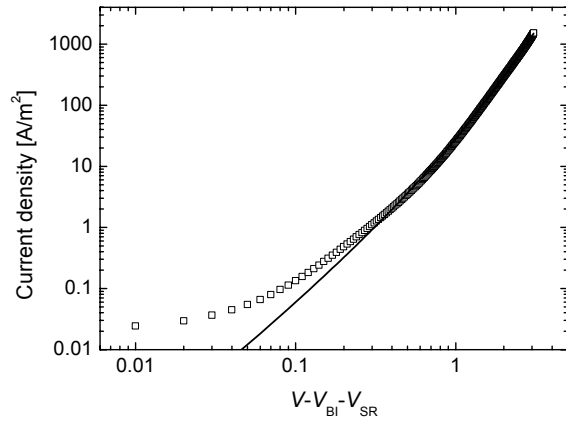


Figure 4.14 Current density-voltage plot of a *nc*-ZnO:MDMO-PPV device (26 vol.-% ZnO) in forward bias measured in the dark. Layer thickness was 230 nm, $\epsilon_r = 3.79$, $V_{BI} = 0.73$ V $V_{SR} = R \times I$, $R = 34$ Ω . The solid line shows a fit using equation 5, $R^2 = 0.99991$ resulting in: $\mu_0 = 9.4 \times 10^{-10}$ m² V⁻¹ s⁻¹, $\beta = 1.2 \times 10^{-3}$ m^{1/2} V^{-1/2}.

implies that the current is not purely space charge limited. Therefore an SCL model with a field dependent mobility has been used to describe the J - V characteristics²⁵:

$$J = \frac{9}{8} \varepsilon_r \varepsilon_0 \mu_0 \frac{V^2}{L^3} \exp\left(0.89 \beta \sqrt{\frac{V}{L}}\right) \quad (5)$$

The film thickness (L) and the dielectric constant (ε_r) have been taken as fixed parameters to fit the above expression in the J - V curve as shown in figure 4.14. For a nc -ZnO:MDMO-PPV blend with 26 vol.-% of ZnO an ε_r of 3.79 has been used²⁶. The voltage (V) in this formula is the corrected voltage as shown in figure 4.14. Table 4.4 shows the results on cells with different active layer thickness. V_{BI} has been determined from the J - V plot and $V_{SR} = R \times I$ with $R = 34 \Omega$ and I the current.

Table 4.4 Fitting results for nc -ZnO:MDMO-PPV devices with 26 vol.-% ZnO, using equation 5.

Nr.	L [nm]	V_{BI} [V]	μ_0 [m ² V ⁻¹ s ⁻¹]	β [m ^{1/2} V ^{-1/2}]
1	230	0.73	9.4×10^{-10}	1.23×10^{-3}
2	175	0.78	2.1×10^{-9}	1.40×10^{-3}
3	170	0.76	6.3×10^{-10}	1.70×10^{-3}
4	120	0.76	2.4×10^{-10}	1.60×10^{-3}
5	110	0.77	6.9×10^{-10}	1.44×10^{-3}
6	95	0.63	7.3×10^{-10}	2.10×10^{-3}
7	50	0.62	5.0×10^{-10}	1.40×10^{-3}
8	40	0.54	3.7×10^{-10}	1.30×10^{-3}
Av.			7.8×10^{-10}	1.52×10^{-3}

The zero-field mobility ranges over one decade while the prefactor (β), which shows the field dependency of the mobility, remains almost constant. In theory, both should be independent from the layer thickness, and indeed no clear dependency has been observed. The variation might be due to errors in the measured layer thickness or the determination of the series resistance. The average value for the zero-field mobility ($\sim 7.8 \times 10^{-10} \text{ m}^2 \text{ V}^{-1} \text{ s}^{-2}$) is similar to the mobility of $2 \times 10^{-10} \text{ m}^2 \text{ V}^{-1} \text{ s}^{-1}$ measured in CdSe-nanocrystal:MEH-PPV blends²⁷. The electron mobility in these nc -ZnO:MDMO-PPV blends is a factor 10 higher than the hole mobility observed for pure MDMO-PPV^{28,29}. Like has been shown for blends of MDMO-PPV and PCBM³⁰, the hole mobility of MDMO-PPV in a blend can be enhanced relative to the mobility in pristine MDMO-PPV. Values for this hole mobility up to $2 \times 10^{-8} \text{ m}^2 \text{ V}^{-1} \text{ s}^{-2}$ have been observed. This indicates we have to be very cautious when interpreting the above results.

4.12 Conclusions

Blends of crystalline ZnO nanoparticles and conjugated polymers like MDMO-PPV and P3HT, have been used as the active layer in bulk heterojunction type photovoltaic devices. Sandwiched between a transparent electrode (PEDOT:PSS on ITO) and a reflecting metal electrode (aluminum), these blends show a similar photovoltaic effect as has been observed for the best hybrid-polymer solar cell reported in literature. The performance of these *nc*-ZnO:MDMO-PPV solar cells depends on the amount of ZnO and the thickness of the active layer. The maximum performance is found for an active blend with a ZnO volume percent of approximately 30% and a layer thickness of approximately 100 nm. For an optimized *nc*-ZnO:MDMO-PPV solar cell the estimated AM1.5 efficiency is 1.6%. Light intensity dependency measurements give insight in the evolution of the performance of these cells with the illumination intensity. Only minor bulk charge carrier recombination occurs in these photovoltaic devices. The efficiency of the device is slightly limited by a drop in *FF* near 1 sun light intensities. The estimated efficiency of *nc*-ZnO:*rr*-P3HT bulk heterojunction solar cells is only 1%. The expected improvement of the photovoltaic effect due to a higher hole mobility in the *rr*-P3HT compared to MDMO-PPV could not be observed. Improving solubility, and stability of the nanoparticles by the addition of *n*-propylamine does not lead to an improvement of the photovoltaic effect. Also, exchanging the nanoparticles with nanorods does not lead to an enhanced performance. ZnO rods are more difficult to disperse in organics apolar solvents and therefore require the addition of *n*-propylamine. Illumination of *nc*-ZnO:MDMO-PPV devices with small amounts of UV light, leads to a complete degradation of the photovoltaic effect. Formation of n-type doped ZnO nanoparticles by direct band gap excitation is responsible for this effect. The long-lived electrons in the conduction band of the nanoparticles can be removed by exposure to oxygen, which restores the photovoltaic effect. Electrons in the ZnO nanoparticle appear to have a mobility of approximately $8 \times 10^{-10} \text{ m}^2 \text{ V}^{-1} \text{ s}^{-1}$ similar to the mobility reported for CdSe nanoparticles.

4.13 Experimental

Materials: The materials used were poly[2-methoxy-5-(3',7'-dimethyloctyloxy)-1,4-phenylenevinylene] (MDMO-PPV) synthesized via the Gilch-route^{31,32}. MDMO-PPV has $M_w = \sim 1 \times 10^6 \text{ g mol}^{-1}$ and a polydispersity of about 7 as determined by size exclusion chromatography (SEC), calibrated against polystyrene. Regio-regular poly(3-hexylthiophene) (*rr*-P3HT, Aldrich) was purified following reduction with hydrazine. Purification was performed by precipitation in methanol, and subsequent Soxhlet extraction in dichloromethane (CH_2Cl_2) and chloroform (CHCl_3). The chloroform fraction ($M_w = 170.000 \text{ g mol}^{-1}$, yield 74%) was used for solar cell preparation. Poly(3,4-ethylenedioxythiophene):poly(styrenesulfonate) (PEDOT:PSS) was purchased from Bayer AG (Baytron P VPAI 4083), and aluminum wire (99.999%) from Engelhard-Clal. ZnO nanoparticles were

prepared as was described in chapter 3. Blends from MDMO-PPV and ZnO in chlorobenzene were prepared starting by dissolving MDMO-PPV in chlorobenzene. The exact amount of the ZnO nanoparticle stock solution needed to reach the desired amounts of ZnO in the blends was determined from the ZnO concentration in the sol. This ZnO concentration was determined from the solid residue after solvent evaporation. The ZnO solution was used within three day after synthesis, as this led to the best cells with the highest reproducibility. On average a ZnO concentration of 65 mg mL^{-1} was obtained. In a typical procedure MDMO-PPV (3 mg) was dissolved in chlorobenzene (0.5 mL). For a 26 vol.-% ZnO:MDMO-PPV blend (an MDMO-PPV:ZnO mass ratio of 1:2), 410 μL of a chlorobenzene:methanol mixture (v:v = 95:5) was added, followed by 90 μL of the ZnO solution. The solution for spin coating contained approximately 4 vol.-% methanol, calculated using a 20 vol.-% methanol concentration for the ZnO solution. This procedure was followed because it led to a better dispersion of the ZnO in the polymer:chlorobenzene solution. Without the addition of methanol, prior to the addition of the ZnO solution, the nanoparticles could partially precipitate. When using *rr*-P3HT, the added amount of methanol was critical. The methanol was necessarily to keep the ZnO particles dissolved, but in time caused precipitation of the *rr*-P3HT. The amount of methanol in the ZnO solution could be decreased down to 10% by centrifugation (when the amount of solvent added after centrifugation was kept constant to 10 mL). The solar cells based on poly(3-hexylthiophene) characterized in this chapter were prepared using a centrifugation step to synthesize the ZnO nanoparticle sol, but decreasing the amount of chloroform down to 5 mL. This way a stable solution of approximately 140 mg mL^{-1} ZnO with 20 vol.-% methanol could be obtained. Using the same procedure for *rr*-P3HT as described for MDMO-PPV, led to 5-6 vol.-% methanol in the solution used for spin casting (in a typical procedure 6 mg *rr*-P3HT was used). Using a centrifugation step leads 3-4 vol.-% methanol in the solution used for spin casting. A further lowering of the amount of methanol led to unstable solutions because the ZnO nanoparticles precipitated.

Photovoltaic cell: Glass plates covered with patterned ITO resulting in 4 different device areas (0.095, 0.116, 0.37, 1.02 cm^2) were used for device preparation. Photovoltaic devices were fabricated by spin casting a solution of the *nc*-ZnO:conjugated polymer mixture onto a poly(3,4-ethylenedioxythiophene):poly(styrenesulfonate) (PEDOT:PSS, Bayer AG) film on a UV-ozone cleaned indium tin oxide (ITO) coated glass substrate. Chlorobenzene based *nc*-ZnO:MDMO-PPV films were spin cast, depending on the film thickness, between 500 and 3000 rpm for 2 minutes. All cast films were additionally dried at 2500 rpm for one minute. Chloroform based blends were spin cast for 1 minute. The back electrode, consisting of 100 nm Al, was evaporated in high vacuum. Film thickness measurements were performed with a Tencor P10 surface profiler.

Current-voltage measurements: J - V measurements were performed in a N_2 atmosphere at room temperature. In forward bias the ITO electrode was positively biased. The devices were illuminated at the transparent ITO anode. J - V characteristics were measured with a computer-controlled Keithley 2400 Source Meter in the dark or under $\sim 85 \text{ mW cm}^{-2}$ illumination from a 100 W tungsten-halogen lamp filtered by a Schott KG01 and GG420 filter resulting in a spectral range of 420-900 nm.

Incident photon to current conversion efficiencies (IPCE): Measurements were performed on a homebuilt set-up, utilizing a xenon lamp and a Spex minimate monochromator. The monochromatic light was focused on a diaphragm (2 mm in diameter) to create a small light spot for solar cell illumination. Light power intensity at 500 nm was 1 mW cm^{-2} as determined with a calibrated Melles-Griot silicon diode. Currents were recorded using a Keithley 2400 Source Meter. Light intensity modulated data were recorded with a chopper at 80 Hz using a lock-in amplifier. Experiments with backlight were recorded by illumination of the solar cell with a continuous backlight of 30 mW cm^{-2} and intensity modulated monochromatic light. The IPCE measurements on *nc-ZnO:rr*-P3HT cells were performed without backlight illumination using monochromatic light power intensity at 500 nm of 1.6 mW cm^{-2} .

- 1 Brabec, C. J. *Sol. Energy Mater. Sol. Cells* **2004**, *83*, 273.
- 2 Huynh, W. U.; Dittmer, J. J.; Alivisatos, A. P. *Science* **2002**, *295*, 2425.
- 3 Greenham, N. C.; Peng, X.; Alivisatos, A. P. *Phys. Rev. B*. **1996**, *54*, 17628.
- 4 Huynh, W. U.; Peng, X.; Alivisatos, A. P. *Adv. Mater.* **1999**, *11*, 923.
- 5 Huynh, W. U.; Dittmer, J. J.; Libby, W. C.; Whiting, G. L.; Alivisatos, A. P. *Adv. Funct. Mater.* **2003**, *13*, 73.
- 6 Campbell, I. H.; Hagler, T. W.; Smith, D. L.; Ferraris, J. P. *Phys. Rev. Lett.* **1996**, *76*, 1900.
- 7 Hagfeldt, A.; Grätzel, M. *Chem. Rev.* **1995**, *95*, 49.
- 8 Brown, T. M.; Kim, J. S.; Friend, R. H.; Cacialia F.; Daik R.; Feast W. J. *Appl. Phys. Lett.* **1999**, *75*, 1679.
- 9 Michaelson, H. B. *J. Appl. Phys.* **1977**, *48*, 4729.
- 10 Kroon J. M.; Wienk M. M.; Verhees W. J. H.; Hummelen J. C. *Thin Solid Films* **2002**, *403-404*, 223.
- 11 Bulle-Lieuwma, C. W. T.; Van Gennip, W. J. H.; Van Duren, J. K. J.; Honkheijm, P.; Janssen, R. A. J.; Niemantsverdriet, J. W. *Appl. Surf. Sci.* **2003**, *203-204*, 547.
- 12 Brabec, C. J.; Shaheen, S. E.; Winder, C.; Sariciftci, S.; Denk, P. *Appl. Phys. Lett.* **2002**, *80*, 1288.
- 13 The relative humidity of the surrounding atmosphere during spin coating seemed to influence the film thickness and the solar cell performance. These effects have not been investigated in great detail but films cast at high humidity (e.g. in summer) appeared 40 nm thinner than those cast at low humidity (e.g. in winter).
- 14 Shaheen, S. E.; Brabec, C. J.; Padinger, F.; Fromherz, T.; Hummelen, J. C.; Sariciftci, N. S. *Appl. Phys. Lett.* **2001**, *78*, 841.
- 15 A linear relation between the current density and the incident light power is also expected when the ZnO nanoparticles are highly doped with electrons. The recombination rate will then be proportional to the hole density alone and therefore also linear with light intensity, even if non-geminate recombination is common. The fact that the J - V curves fit to an SCLC model (section 4.11), and that n-type doping by UV light exposure (section 4.9) leads to a huge increase of dark conductivity, is evidence for a low initial electron doping of the ZnO nanoparticles. The observed photoluminescence (section 3.3.2) from these nanoparticles also indicates that the initial doping is small or these particles are undoped; because electron doped nanoparticles do not show a visible photoluminescence.
- 16 Huynh, W. U.; Dittmer, J. J.; Tecler, N.; Milliron, D. J.; Alivisatos, A. P.; Barnham, K. W. J. *Phys. Rev. B*. **2003**, *67*, 115326-1.
- 17 Coakley, K. M.; McGehee M. D. *Chem. Mater.* **2004**, *16*, 4533.
- 18 The maximum photon current is calculated, assuming that for the organic semiconductor for wavelengths above the bandgap, the EQE is 100%, leading to an estimate of 8 mA cm⁻² under AM1.5G illumination. From the energy diagram in figure 4.2a a maximum V_{OC} of 0.9 V has been estimated. While assuming the maximum FF is 1, this leads to an efficiency of 7%.

- 19 Kwong, C. Y.; Djurišić, A. B.; Chui, P. C.; Cheng, K. W.; Chan, W. K. *Chem. Phys. Lett.* **2004**, *384*, 372.
- 20 Sun, B.; Marx, E.; Greenham, N. C. *Nano Lett.* **2003**, *3*, 961.
- 21 Wienk, M. M.; Kroon, J. M.; Verhees, W. J. H.; Knol, J.; Hummelen, J. C.; Van Hal, P. A.; Janssen, R. A. J. *Angew. Chem. Int. Ed.* **2003**, *42*, 3371.
- 22 Siringhaus, H.; Brown, P. J.; Friend, R. H.; Nielsen, M. M.; Bechgaard, K.; Langeveld-Voss, B. M. W.; Spiering, A. J. H.; Janssen, R. A. J.; Meijer, E. W.; Herwig, P. T.; de Leeuw, D. M. *Nature* **1999**, *401*, 685.
- 23 The amount of absorbed photons has been estimated from the optical density (OD) of the solar cells, correcting for the reflecting back electrode. % absorbed photons = $(1 - 10^{-2 \times OD}) \times 100\%$. This rough estimate is not taking into account any reflection losses, but is sufficient for comparing two different solar cells from MDMO-PPV and *rr*-P3HT.
- 24 L. J. A. Koster, University of Groningen, replaced the Al with a Pd electrode and measured a 100 fold lower current in forward bias. Further explorations on electron and hole mobility in these devices are under investigation.
- 25 Manabe, K.; Hu, W.; Matsumura, M.; Naito, H. *J. Appl. Phys.* **2003**, *94*, 2024.
- 26 This is a volume averaged ϵ_r , using $\epsilon_r = 2.1$ for MDMO-PPV and $\epsilon_r = 8.6$ for ZnO.
- 27 Ginger, D. S.; Greenham, N. C. *Synth. Met.* **2001**, *124*, 117.
- 28 Mihaletchi, V. D.; Van Duren, J. K. J.; Blom, P. W. M.; Hummelen, J. C.; Janssen, R. A. J.; Kroon, J. M.; Rispen, M. T.; Verhees, W. J. H.; Wienk, M. M. *Adv. Funct. Mater.* **2003**, *13*, 43.
- 29 Simulations were performed of the dark current in forward bias by L. J. A. Koster, University of Groningen. Simulating a 10 fold higher electron than hole mobility, like is estimated in these solar cells, gives similar dark currents compared to a simulation using a 100 fold difference. This implies that even a 10 higher mobility still gives electron-dominated devices.
- 30 Melzer, C.; Koop, E. J.; Mihaletchi, V. D.; Blom, P. W. M. *Adv. Funct. Mater.* **2004**, *14*, 865.
- 31 Martens, H. C. F.; Blom, P. W. M.; Schoo, H. F. M., *Phys. Rev. B.* **2000**, *61*, 7489.
- 32 MDMO-PPV was generously provided by Philips Research Laboratories Eindhoven.

Chapter 5

Characterization of *nc*-ZnO:conjugated polymer bulk heterojunctions

Abstract

Chapter 4 shows that bulk heterojunction solar cells can be made from blends of nanocrystalline ZnO and conjugated polymers. The properties of these blends have been characterized in this chapter. Photoluminescence quenching experiments together with photoinduced absorption spectroscopy confirm that photoinduced charge separation occurs. The kinetics of this photoinduced charge transfer is studied with time-resolved pump-probe spectroscopy. Flash-photolysis time-resolved microwave conductivity (FP-TRMC) has been used to gain insight into the relation between the amount of ZnO in the blend and the mobility of photoinduced charges. As is shown in chapter 4, the composition of the bulk heterojunction has a major effect on the performance of the solar cell. Atomic force microscopy (AFM) and transmission electron microscopy (TEM) have been used to gain insight into the morphology of these blends, both the morphology, and their performance in a photovoltaic device show a clear dependency on the ZnO content.

5.1 Introduction

The optical and electrical properties of blends of inorganic and organic materials are often complex, and rarely a simple superposition of the properties of the individual components. One major factor that influences their properties is the morphology of these blends. For example, both enhanced^{1,2} and decreased³ current densities have been observed through blends of inorganic nanoparticles and conjugated polymers. The current increase observed in a light-emitting diode made from a SiO₂:PPV nanocomposite, has been interpreted by Blom *et al.*¹ by a decrease of the effective film thickness. To explain similar observations in blends of SiO₂ and TiO₂ nanoparticles in MEH-PPV, Bozano *et al.*⁴ assume a higher effective field over the blend. Carter *et al.*², explain the current increase by a more effective injection of charges due to an increase in surface roughness. Ho and Friend³ argue that the high currents observed in these composites can be explained by assuming that the nanoparticles form large aggregates. These aggregates aid in the alignment of the polymer chains in the direction of the electrodes. In their paper, lower currents and a lower mobility of the hole on the PPV have been reported upon blending with SiO₂ nanoparticles. Blending PPV with small SiO₂ particles leads to very homogeneous blends, and no large aggregates can be observed. These particles induce more disorder in the polymer phase and therefore lower the hole mobility. According to Carter *et al.*², blending of TiO₂ nanoparticles with MEH-PPV leads to an increase of the electroluminescence compared to pure MEH-PPV based LEDs. Even laser action has been observed in blends from 270 nm sized TiO₂ particles and MEH-PPV⁵. In contrast to this, other researchers, *e.g.* Salafsky⁶ and Petrella *et al.*⁷, have observed a significant quenching of the polymer photoluminescence in similar blends from TiO₂ nanoparticles and PPV.

These controversies are likely due to the complex and diverse morphology of these hybrid systems. The length scale of phase separation, the distribution of the nanoparticles, and the size and nature of the particles itself, all contribute to this complex picture. For photovoltaic devices the morphology is important, because phase separation plays a major role in their performance. For efficient polymer bulk heterojunction solar cells, a balance exists between sufficiently large and continuous domains needed for an efficient transport of charges, and a short length scale of phase separation for an efficient photoinduced charge separation. This delicate balance has nicely been observed for PCBM:MDMO-PPV bulk heterojunction solar cells^{8,9}. For hybrid CdSe-nanorod:rr-P3HT polymer solar cells the morphology and the photovoltaic effect are strongly related to the exact solvent mixture¹⁰. A similar strong solvent dependency has been observed for *nc*-TiO₂:rr-P3HT polymer solar cells¹¹.

Determining the nanoscale morphology of bulk heterojunction solar cells is important for a proper understanding of the macroscopic device characteristics, and might help in improving their performance. However, not one single technique is sufficient in describing the morphology

completely. Atomic force microscopy can be used to study the surface of a blend, but hardly gives insight into the interior of these blends. Transmission electron microscopy is capable of giving information about spatial distributions of materials in thin films of the blends, but only gives a transmission image. Combining these methods with different optical and spectroscopic techniques like fluorescence spectroscopy, transient absorption spectroscopy, and microwave conductivity, gives strong tools that can help to gain more insight into these solar cells. This is the subject of this chapter.

5.2 Photo-physical characterization of *nc*-ZnO:conjugated polymer composites

5.2.1 UV-vis absorption spectroscopy

Ultraviolet and visible absorption spectra have been recorded to investigate the relation between the amount of ZnO added to the solution used for spin coating and the amount of ZnO in the spin cast film. Upon addition of the ZnO nanoparticles the UV-vis absorption spectra of the blends (figure 5.1a) show a gradual increase of the ZnO contribution (below 400 nm) relative to the MDMO-PPV absorption ($\lambda_{\max} = 505$ nm). The MDMO-PPV absorption spectrum does not change, the optical density at the maximum stays roughly the same because in this experiment a constant amount of MDMO-PPV has been used, and the amount of ZnO has been increased.

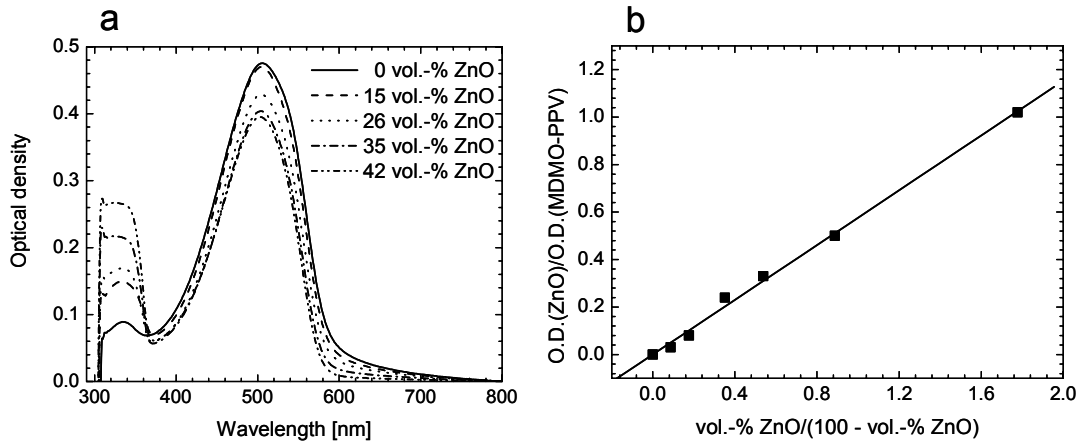


Figure 5.1 a) UV-vis spectra of spin cast films of *nc*-ZnO:MDMO-PPV (3 mg mL^{-1} MDMO-PPV) blends cast at 1500 rpm on PEDOT:PSS covered ITO substrates. b) Ratios of the optical density of ZnO (335 nm) and MDMO-PPV (505 nm) as function of the ratio of the vol.-% ZnO.

In a first approximation, the relation between the amount of ZnO in the blend and the ratio of the optical density of ZnO over the optical density of the MDMO-PPV is given by:

$$\frac{OD_{ZnO}}{OD_{PPV}} = \frac{\alpha_{ZnO} \times L_{ZnO}^{eff}}{\alpha_{PPV} \times L_{PPV}^{eff}} \sim \frac{\text{vol.} - \% \text{ ZnO}}{100 - (\text{vol.} - \% \text{ ZnO})} \quad (1)$$

Where L^{eff} is the effective path length, α the absorption coefficient, and vol.-% ZnO is the volume percentage of ZnO in the film¹². The experimental data in figure 5.1b reveal that there exists a good

correlation between the amount of ZnO in the solution used for spin casting and the amount of ZnO in the film. Using the absorption coefficient of MDMO-PPV ($1.3 \times 10^7 \text{ m}^{-1}$)¹³, and the slope of the plot in figure 5.1b ($\alpha_{\text{ZnO}}/\alpha_{\text{MDMO-PPV}} = 0.58$), an estimate of $7 \times 10^6 \text{ m}^{-1}$ for the absorption coefficient of the ZnO nanoparticles is obtained. The calculated absorption coefficient is higher than the value reported for ZnO crystals ($\alpha_{\text{ZnO}} \sim 1 \times 10^6 \text{ m}^{-1}$)¹⁴, in accordance with the fact that for quantum confined nanoparticles the absorption coefficient shows a strong increase compared to its bulk value¹⁵.

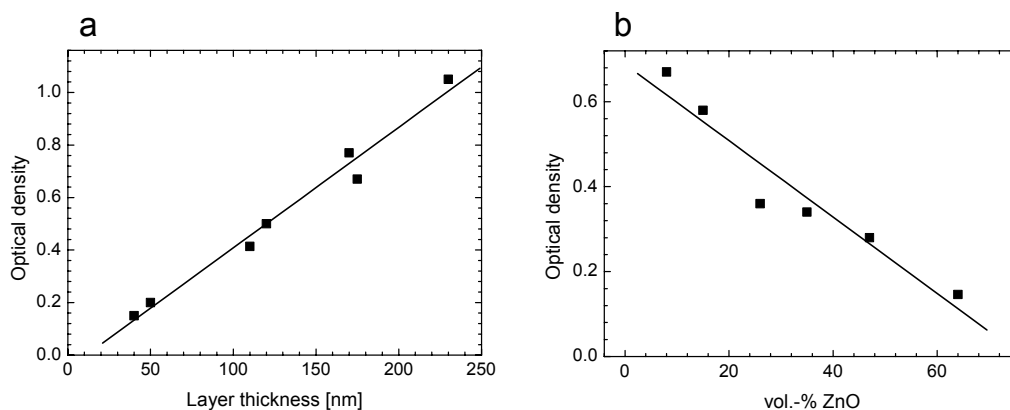


Figure 5.2 a) Optical density of MDMO-PPV at $\lambda = 505 \text{ nm}$ as a function of layer thickness for blends having 26 vol.-% ZnO. b) Optical density as a function of the vol.-% ZnO in the blend for approximately 100 nm thick *nc*-ZnO:MDMO-PPV layers.

As expected, the optical density at 505 nm (for MDMO-PPV) scales linearly with the layer thickness for blends having the same amount of ZnO (figure 5.2a). For approximately 100 nm thick *nc*-ZnO:MDMO-PPV layers (see figure 5.2b), the optical density of MDMO-PPV at 505 nm drops with increasing amount of ZnO in the blend. This demonstrates that the absorption properties of the *nc*-ZnO:MDMO-PPV blends can be treated as a linear combination of the optical properties of the absorption spectra of the components. This allows accessing the actual composition of the films by measuring UV spectra.

5.2.2 Photoluminescence spectroscopy

Mixing conjugated polymers with electron accepting materials generally leads to a quenching of the photoluminescence of the conjugated polymer. The quenching of the photoluminescence is often used as a first indication that electron transfer occurs in these donor-acceptor systems.

A quenching of the photoluminescence of conjugated polymers upon addition of metal oxide nanoparticles has been observed for TiO_2 . Salafsky⁶ observed a complete quenching of the photoluminescence of PPV after addition of 40 wt.-% TiO_2 (15 vol.-%). The blends have been made from mixtures of TiO_2 nanoparticles and a precursor for PPV in methanol. After spin casting, the film has been treated at high temperatures under argon flow to convert the precursor into PPV. Kwong *et al.* have reported the only bulk heterojunction hybrid polymer- TiO_2 solar cell that shows a reasonable

photovoltaic effect. They succeeded in mixing the nanoparticles with regio-regular P3HT in non-polar organic solvents.¹¹ The photoluminescence of the P3HT has been reported to decrease upon mixing with TiO₂ nanoparticles¹⁶. Petrella *et al.*⁷ have been able to synthesize organic capped TiO₂ nanorods that in combination with MEH-PPV could be dissolved in chloroform. Quite surprisingly, capping with oleic acid (C₁₈H₃₃CO₂H) does not prohibit the electron transfer process from the polymer to the nanoparticle: after addition of 20 vol.-% of TiO₂, the MEH-PPV photoluminescence is completely quenched.

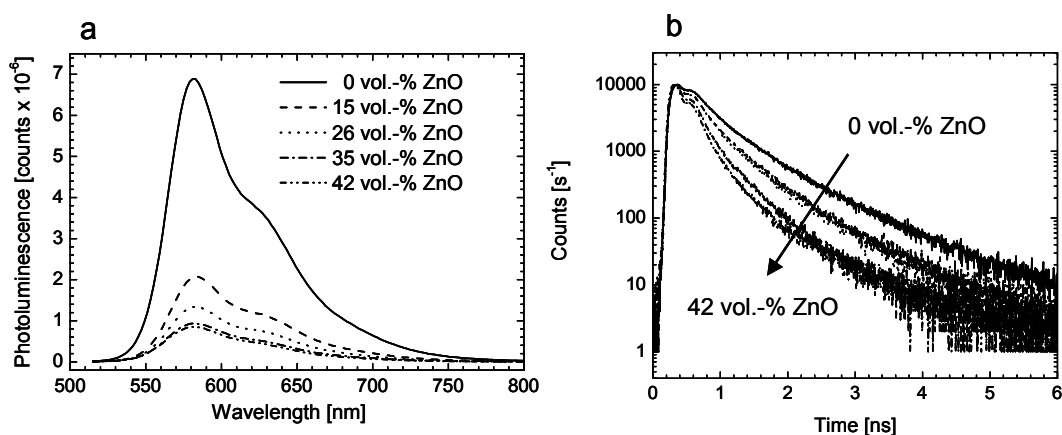


Figure 5.3 a) Photoluminescence spectra of *nc*-ZnO:MDMO-PPV blends, excitation performed at 505 nm, the intensities are corrected for the optical density of the films. b) Time-resolved photoluminescence traces of the emission at 580 nm recorded after excitation at 400 nm. The data have been normalized at 10.000 counts.

In accordance with the relative position of the energy levels (figure 4.2), the photoluminescence of MDMO-PPV is quenched upon addition of ZnO (figure 5.3a). After addition of 35 vol.-% ZnO, 85% of the original MDMO-PPV photoluminescence is quenched, *i.e.* at least 85% of the absorbed photons lead to charge separation. Addition of more ZnO does not lead to a further quenching of the photoluminescence. The residual photoluminescence is consistent with phase separation between the MDMO-PPV and the ZnO on a length scale bigger than the exciton diffusion length (approximately 10 nm for MDMO-PPV). The time-resolved photoluminescence traces (figure 5.3b) show a decrease of the lifetime of the MDMO-PPV photoluminescence. This indicates that a fast electron transfer process occurs in competition with the photoluminescence.

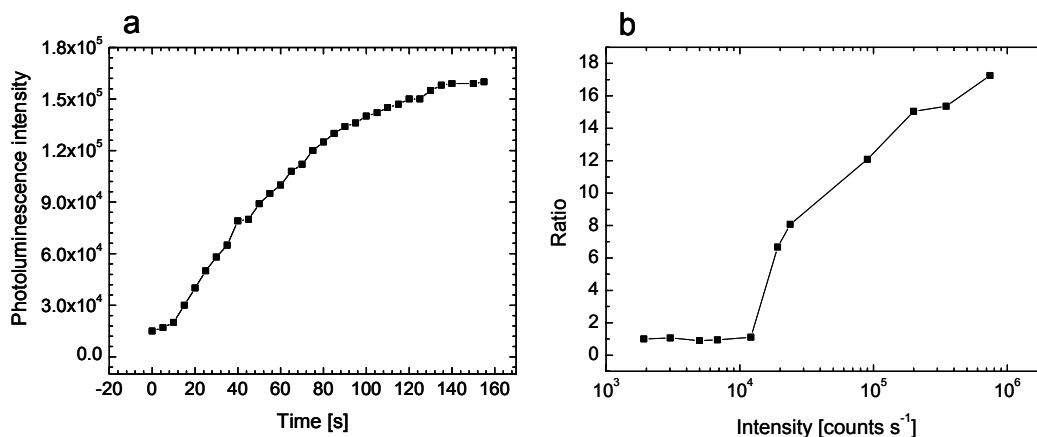


Figure 5.4 Light induced fluorescence enhancement effect observed in *nc-ZnO:rr*-P3HT blends (47 vol.-% ZnO). a) Increase of the fluorescence with illumination time, recorded at 630 nm after excitation at 550 nm. b) Dependency of the ratio of the fluorescence limit over the starting fluorescence. The intensity was recorded by a reference silicon photodiode.

The photoluminescence of a *nc-ZnO:rr*-P3HT blend hardly differs from a pristine P3HT film, no clear photoluminescence quenching has been observed. In these *nc-ZnO:rr*-P3HT blends a curious phenomenon has been observed which has been called a ‘light-induced fluorescence enhancement’ effect (see figure 5.4). The photoluminescence of a *nc-ZnO:rr*-P3HT blend (with 47 vol.-% ZnO) increases in time when exposed to the excitation beam. This increase is much less in blends that contain lower amounts of ZnO nanoparticles. Initially the photoluminescence is similar to a P3HT film without ZnO, but it increases by approximately a factor 10 after exposure to the excitation beam for 2 minutes. The shape of the photoluminescence spectrum does not change, but the fluorescence maximum shifts slightly from 630 nm to 638 nm. The photoluminescence ultimately reaches a constant intensity; the ratio of this value and the initial photoluminescence intensity depends on the illumination intensity (figure 5.4b). The ‘light-induced fluorescence enhancement’ effect seems to require a certain threshold intensity, after which the ratio of the constant fluorescence intensity over the starting fluorescence intensity increases steeply. The time required to reach the constant fluorescence intensity is long (minutes) at low intensities, and short (seconds) at high intensities. The whole process is completely reversible, after storing the films in the dark for a few minutes the photoluminescence returns to its original value. Interpretation of photoluminescence quenching experiments on *rr*-P3HT samples is rather difficult. In the solid state, due to stacking of their π -systems, regio-regular polythiophenes show a significant self-quenching of their photoluminescence. Addition of particles that disrupt the stacking of chains can therefore cause an increase of the photoluminescence. One explanation for this phenomenon might be the formation of long-lived electrons in the conduction band of the ZnO nanoparticles. The presence of this electron blocks further electron transfer processes to the nanoparticle, which causes an increase of the

photoluminescence. The issue remains what happens to the photogenerated holes on the P3HT and why these holes apparently do not quench the exciton emission. The intensity dependence of this effect can be explained. At low intensities only a small amount of electrons are present on the nanoparticles. At high illumination intensities all, or a large fraction of the nanoparticles are rapidly charged and block further electron transfer. When the light is turned off the residual holes and electrons recombine, this takes a few minutes for completion. The long lifetime of these photoinduced charges has also been observed in chapter 3. The increase of the photoluminescence intensity above the value of a pristine *rr*-P3HT film indicates that in the vicinity of the ZnO nanoparticles the stacking of the polythiophenes has been disrupted. The irregularly stacked chains have a much higher photoluminescence quantum yield than the stacked chains in bulk regio-regular polythiophenes. Upon charging of the nanoparticles, the photoluminescence of these irregularly stacked chains is no longer quenched. In a recent paper such an enhancement of the photoluminescence of a thin film of polyhexylthiophenes near the surface of a TiO₂ layer has been observed¹⁷.

5.2.3 Photoinduced absorption spectroscopy

The photoluminescence quenching experiments for *nc*-ZnO:MDMO-PPV strongly suggest electron transfer occurs, whereas for *nc*-ZnO:*rr*-P3HT there is only an indication that electron transfer occurs. Photoinduced absorption spectroscopy (PIA, figure 5.5) is used, to prove that in both cases electron transfer occurs from the polymer to the nanoparticle.

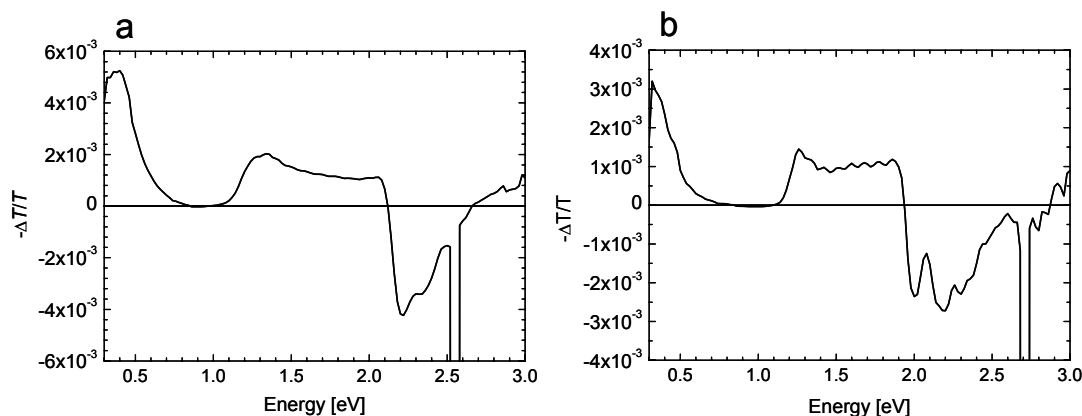


Figure 5.5 Near-steady state photoinduced absorption (PIA) spectra of: a) *nc*-ZnO:MDMO-PPV blend (35 vol.-% ZnO) on quartz, measured at 80 K with modulated (275 Hz) excitation at 2.54 eV (488 nm). The pump power was 25 mW with a beam diameter of 2 mm. b) *rr*-P3HT: *nc*-ZnO blend (35 vol.-% ZnO) on quartz, measured at 80 K with modulated (275 Hz) excitation at 2.71 eV (458 nm).

Laser excitation of the *nc*-ZnO:MDMO-PPV blend at 488 nm affords a PIA spectrum with a photobleaching band of the neutral MDMO-PPV at 2.2 eV and the characteristic absorption bands of the polymer radical cation around 0.4 eV and 1.3 eV.¹⁸ The intensity ratio of these bands is different from usual, and we attribute the higher intensity of the 0.4 eV band to electrons injected into the ZnO,

which also give rise to an absorption in this region.^{19, chapter 3} These results correspond well to the PIA and NIR spectra of the injected electron in ZnO nanoparticles shown in figure 3.5b. The PIA spectrum shows remarkable resemblance to spectra from InP:MDMO-PPV and CdSe:MDMO-PPV blends observed by Pientka *et al.* in these spectra the low energy absorption band has been attributed to absorption from injected electrons in the nanocrystals.^{20,21} After mixing ZnO nanoparticles with *rr*-P3HT, charge separation also occurs and the PIA spectrum is similar to the one observed for MDMO-PPV. Both *nc*-ZnO:MDMO-PPV and *nc*-ZnO:*rr*-P3HT blends show photoinduced charge separation and the formation of long lived charges. The formation of long-lived charges is essential to obtain a photovoltaic effect as has been observed for these blends in chapter 4.

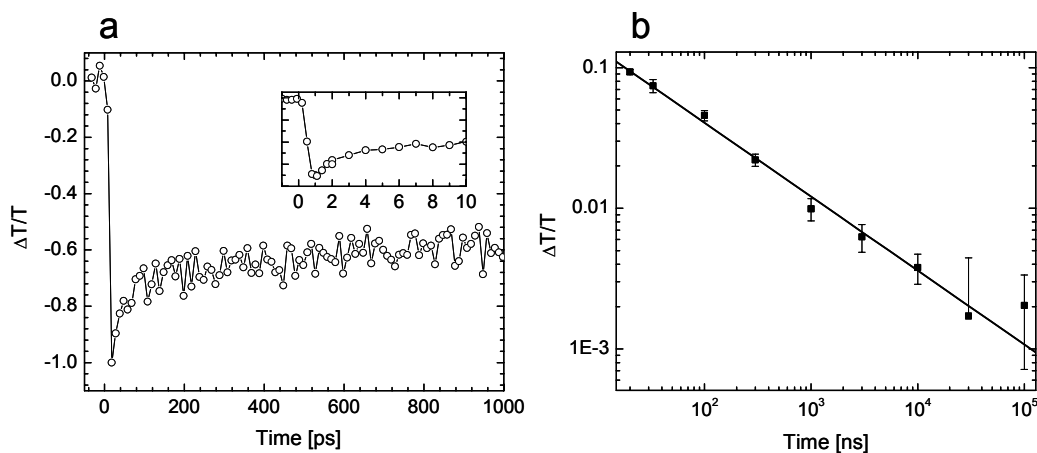


Figure 5.6 a) Time resolved pump-probe spectroscopy measured at room temperature, monitoring the intensity of the radical cation band at 0.56 eV (2200 nm), after excitation at 2.43 eV (510 nm) with 200 fs pulses. The inset shows the transient absorption at short time delays. b) Decay of the depth of the spectral hole in an *nc*-ZnO:MDMO-PPV blend (26 vol.-% ZnO) as a function of time. Excitation 2.76 eV (450 nm), pump fluence 1 mJ cm⁻².

The kinetics of charge generation has been studied with pump-probe spectroscopy (figure 5.6a) by monitoring the intensity of the low energy radical cation absorption band at 2200 nm (0.56 eV). Upon excitation at 510 nm (2.43 eV) with 200 fs pulses, the PIA signal rises within one picosecond, demonstrating an ultra fast electron transfer. This is as fast as the electron injection times (< 300 fs) reported by Bauer *et al.*²² for Ru(dcbpy)₂(NSC)₂ dyes on nanoparticulate ZnO electrodes.

Hole-burning spectroscopy (nanosecond photoinduced spectroscopy, figure 5.6b) measurements on *nc*-ZnO:MDMO-PPV blends reveal that the recombination kinetics appear similar to the recombination kinetics in PCBM:MDMO-PPV blends²³. The intensity of the spectral hole decayed with time according to $I \propto t^{-0.53}$. For PCBM:MDMO-PPV blends it was shown that for this type of recombination the rate is limited by the detrapping of the cationic charge carriers in MDMO-PPV²³. This result indicates that on the ns time scale, the initial geminate recombination has already occurred.

5.2.4 Flash photolysis time-resolved microwave conductivity²⁴

In flash photolysis time-resolved microwave conductivity (FP-TRMC) measurements the sample is irradiated with pulsed laser light and analyzed with microwaves. When excitation of the sample leads to formation of mobile charges, changes in the (local) conductivity of the sample occur. Because mobile charges absorb microwave radiation, any photoinduced change in the conductance of the sample can be monitored as a change in the microwave reflectance. The change in conductance, normalized by the excitation intensity, can be expressed into several relevant parameters¹³:

$$\frac{\eta \Sigma \mu}{F_A} \quad (2)$$

Where F_A is the fraction of incident photons actually attenuated within the layer, η is the charge separation efficiency per incident photon, so η/F_A is the quantum yield per absorbed photon, and $\Sigma\mu$ is the sum of the charge carrier mobilities ($\Sigma\mu = \mu_{\text{hole}} + \mu_{\text{electron}}$).

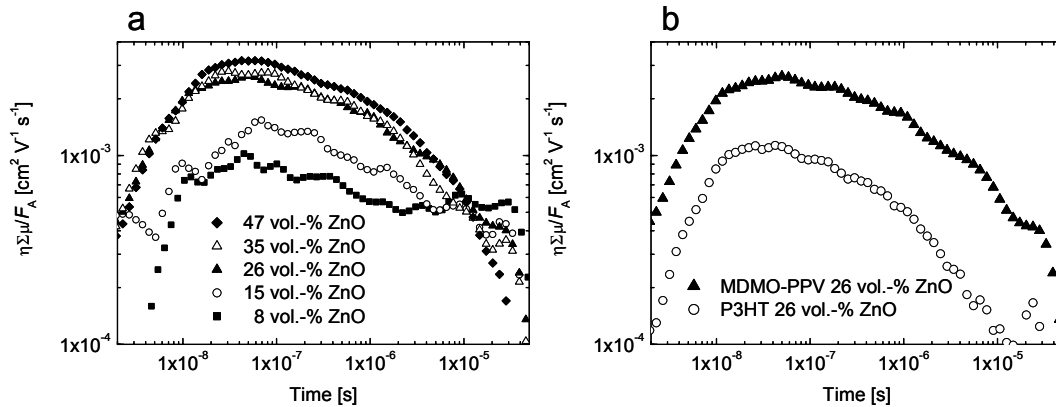


Figure 5.7 a) FP-TRMC transients of *nc*-ZnO:MDMO-PPV blends with different amounts of ZnO, excitation at 510 nm. b) Comparison of the FP-TRMC transients of *nc*-ZnO:MDMO-PPV and *nc*-ZnO:*rr*-P3HT blends with 26 vol.-% ZnO, excitation at 510 nm for the MDMO-PPV and 480 nm for the P3HT.

Photoexcitation of an *nc*-ZnO:MDMO-PPV blend at the absorption maximum of the MDMO-PPV results in transients as shown in figure 5.7a. Given the instrumental response time of 18 ns, it takes approximately 60 ns for the signal to reach its maximum value. It has been observed for PCBM:MDMO-PPV blends that due to the fast (within a few ns) initial geminate recombination, on the time scale of the TRMC measurements only approximately 30% of the initially formed charges are present¹³.

The change in microwave conductivity in both *nc*-ZnO:MDMO-PPV and *nc*-ZnO:*rr*-P3HT blends is observable up to micro- and even milliseconds; this confirms that the photoinduced charges are long-lived. The lifetime of the charges in *nc*-ZnO:*rr*-P3HT blends is slightly shorter than in *nc*-ZnO:MDMO-PPV blends. The maximum TRMC signal (figure 5.7b) is lower for the *nc*-ZnO:*rr*-P3HT blend compared to the *nc*-ZnO:MDMO-PPV blend. The dependence of the TRMC signal is

investigated as a function of the volume percent of ZnO in the blend. The maxima of the transients shown in figure 5.7a have been plotted in figure 5.8 versus the vol.-% ZnO for *nc*-ZnO:MDMO-PPV (figure 5.8a) and *nc*-ZnO:*rr*-P3HT (figure 5.8b) blends.

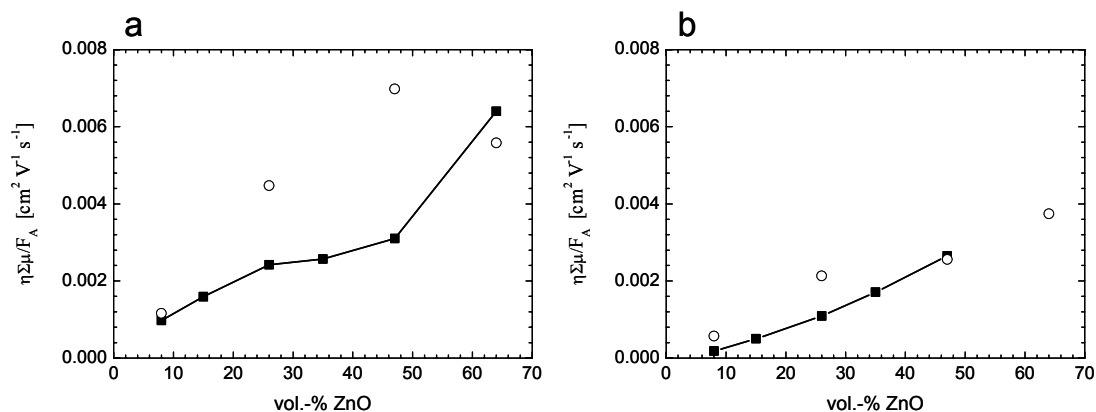


Figure 5.8 Maxima of the FP-TRMC transients as a function of the vol.-% ZnO in the blend. a) *nc*-ZnO:MDMO-PPV (510 nm) and b) *nc*-ZnO:*rr*-P3HT (480 nm). The solid squares show data recorded during a single experiment, the open circles indicate a control experiment.

Even though reproducibility of the data points is rather poor, the overall trend is clear. Upon raising the ZnO content, the TRMC signal increases both in MDMO-PPV and P3HT. Because the TRMC signal is a combination of the mobility and the amount of charges, the higher signal can be described with changes in both. The photoluminescence quenching experiments on *nc*-ZnO:MDMO-PPV blends indicate that up to 35 vol.-% ZnO the amount of photogenerated charges increase with increasing ZnO content. Up to 35 vol.-%, the trends in figure 5.8a can therefore be explained by an increase in the amount of photoinduced charges. The quantum yield of charge formation per absorbed photon for the *nc*-ZnO:MDMO-PPV blends can be estimated from the photoluminescence quenching experiments, $\eta/F_A \approx 0.85$. This leads to the sum of the mobilities being approximately $7 \times 10^{-3} \text{ cm}^2 \text{ V}^{-1} \text{ s}^{-1}$. This mobility is clearly higher than those reported for photoinduced holes on the MDMO-PPV and therefore is likely to be the mobility of the electron in the quantum confined ZnO nanoparticle²⁵. This value is much lower than the reported bulk values (chapter 3, table 1). In a small nanocrystal the mobility of an electron is restricted due to boundary effects; the electron does not freely move but bounces at the interface of the nanoparticle²⁶.

The increase in microwave conductivity found for *nc*-ZnO: *rr*-P3HT blends is lower than found for *nc*-ZnO:MDMO-PPV. Because the same ZnO nanoparticles have been used these lower values are not likely due to a lower mobility of the electron, the difference might be explained by a lower quantum yield per absorbed photon. A lower estimate for the internal quantum efficiency (IQE) has also been obtained for the *nc*-ZnO:*rr*-P3HT compared to the *nc*-ZnO:MDMO-PPV photovoltaic

devices, see figure 4.13b and corresponding discussion in chapter 4. This might indicate that the fast initial geminate recombination is higher in the P3HT than in the MDMO-PPV based blends.

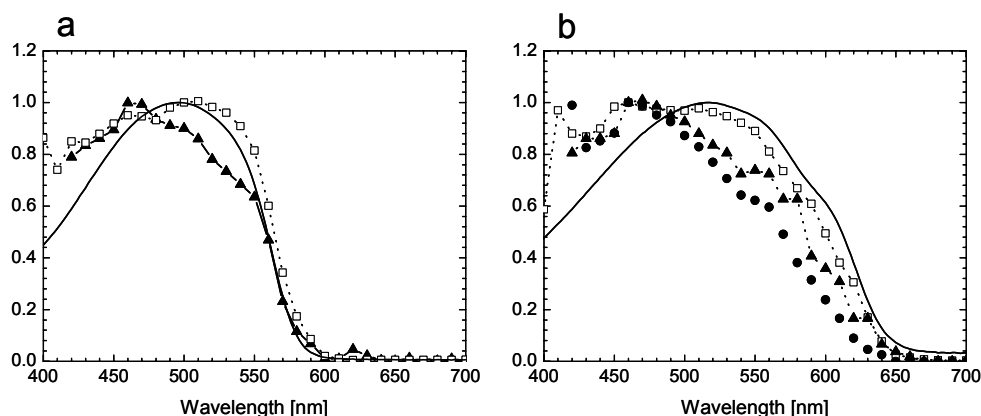


Figure 5.9 a) Comparison of the attenuation spectrum of the *nc*-ZnO:MDMO-PPV blend (solid curve), the IPCE spectrum of an *nc*-ZnO:MDMO-PPV blend (\square), and the TRMC action spectrum of an *nc*-ZnO:MDMO-PPV blend (\blacktriangle). b) Comparison of the attenuation spectrum of the *nc*-ZnO:rr-P3HT blend (solid curve), the IPCE spectrum of an annealed *nc*-ZnO:rr-P3HT blend (\square), the TRMC action spectrum of a un-annealed *nc*-ZnO:rr-P3HT blend (\bullet), and the TRMC action spectrum of an annealed *nc*-ZnO:rr-P3HT blend (\blacktriangle). All spectra have been normalized at their maximum.

The TRMC signals can also be recorded as a function of the excitation wavelength. For *nc*-ZnO:MDMO-PPV the onset observed in the action spectrum²⁷ is the same as found in the attenuation²⁷ and IPCE spectra of the blend (figure 5.9a). There exists a small discrepancy around λ_{\max} of the MDMO-PPV. In chapter 4, the IPCE spectrum *nc*-ZnO:rr-P3HT shows a small discrepancy with the absorption spectrum measured on a photovoltaic device. The discrepancy is less when the IPCE is compared to the attenuation spectrum of the blend (figure 5.9b), because the attenuation spectrum has been corrected for reflection losses. In the TRMC action spectrum the discrepancy is larger, compared to the attenuation spectrum the maximum of the action spectrum is shifted 50 nm to the blue (figure 5.9). After annealing the *nc*-ZnO:rr-P3HT blend the action spectrum shows a better resemblance to the IPCE spectrum. From the TRMC action spectrum it might be concluded that in the vicinity of the nanoparticles the P3HT chains are disordered, and annealing slightly improves the packing of these P3HT chains. After annealing the TRMC signal does not increase, only a longer lifetime of the signal is apparent. This longer lifetime of the photoinduced charges can explain the large increase in short circuit current observed after annealing *nc*-ZnO:rr-P3HT devices (chapter 4).

5.3 Morphology studies on *nc*-ZnO:MDMO-PPV composites

The morphology of the *nc*-ZnO:MDMO-PPV blends has been studied by transmission electron microscopy (TEM) and tapping mode atomic force microscopy (TM-AFM). The correlation between the amount of ZnO in the blend and the morphology is the main subject of this exploration.

5.3.1 Transmission electron microscopy²⁸

Thin (100 nm) layers of the *nc*-ZnO:MDMO-PPV blends have been investigated with TEM. The blend layers have been separated from the PEDOT:PSS underlayer by floatation on water.

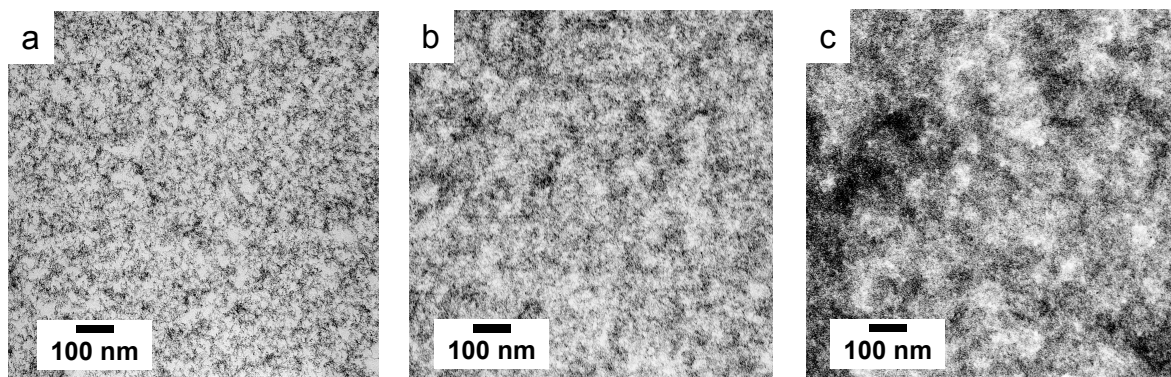


Figure 5.10 Transmission electron microscopy (TEM) photographs of thin (100 nm) films of *nc*-ZnO:MDMO-PPV blends having: a) 8 vol.-% ZnO, b) 26 vol.-% ZnO and c) 47 vol.-% ZnO.

The higher electron density of the ZnO nanoparticles compared to the MDMO-PPV gives rise to contrast in TEM images. The dark regions indicate the presence of ZnO nanoparticles. Films with a low amount of ZnO nanoparticles (8 vol.-%, see figure 5.10a) show a rather homogeneous mixture of ZnO nanoparticles and MDMO-PPV. Upon addition of more ZnO (figure 5.10b) the domain size of the ZnO rich and poor phases seems to increase slightly. A further increase of the amount of ZnO nanoparticles to 47 vol.-% (figure 5.10c) induces an even coarser phase separation. It appears as if these blends start rather homogeneously mixed and upon addition of more ZnO nanoparticles a coarser phase segregation sets in. One problem with interpreting these TEM images is that the obtained image is a transmission view of the film. This implies that contrast is not only determined by the composition but also by the thickness of the film. Only smooth thin films show a true composition image. The larger domain size observed in the image shown in figure 5.10c is likely partly due to an increase in surface roughness.

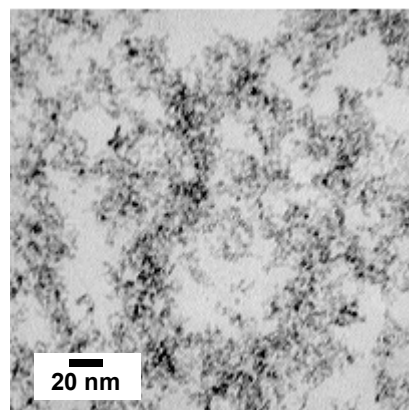


Figure 5.11 Transmission electron microscopy (TEM) photograph of a 50 nm thin film of a *nc*-ZnO:MDMO-PPV blend with 26 vol.-% ZnO.

To investigate the true lateral spatial distribution of ZnO, a thin film (50 nm) of the 26 vol.-% ZnO containing blend has been investigated. In thin films the transmission is less obscured by shadowing effects of ZnO nanoparticles. A TEM photograph of a small section of this film is shown in figure 5.11. A phase separation on a nanometer scale exists, because regions can be observed where no ZnO nanoparticles can be detected. The presence of these pure MDMO-PPV regions, some bigger than 10 nm (the approximate exciton diffusion length in PPV) explains the observation of some residual photoluminescence after addition of ZnO (figure 5.3a).

Compared to the very coarse phase separation observed by Zhang²⁹ it is clear that the nanoparticulate route gives more suitable morphologies than can be obtained by mixing alcohol based TiO₂ sols and precursor PPV solutions. Compared to the CdSe nanorod based solar cells the morphology based on the TEM pictures appears rather similar; in both cases well-mixed composites have been obtained¹⁰. Bulk heterojunction solar cells made from MDMO-PPV and PCBM show a very clear phase separation when investigated with TEM, clearly separated uniform PCBM rich domains have been observed that seem to be imbedded in a MDMO-PPV rich matrix⁹. In general, all working bulk heterojunction photovoltaic devices show a morphology that balances between a well-dispersed system and a phase separated one, leading to a phase separation on a nanometer scale.

5.3.2 Tapping-mode atomic force microscopy

The TEM images of *nc*-ZnO:MDMO-PPV blends seem to imply that the blends are phase segregated at a nanometer scale. Studying the surface morphology of thin films can reveal further information on the distribution of phases in a phase-segregated system. Tapping mode AFM (TM-AFM) can be a powerful tool in this respect. For example, phase separation in block copolymers has been studied widely with TM-AFM. Tapping mode AFM is a non-destructive mode tool for the study of soft materials, and can give information not only about the height differences but also the composition of the materials on the surface. When studying block copolymers with soft and hard blocks^{30,31}, TM-AFM allows discriminating between the two phase-separated blocks. However, interpretation of the height and phase images is challenging, because they can be significantly influenced by parameters like tapping force, the tip shape and quality, humidity, and the nature of the sample itself (hydrophobic, hydrophilic, tacky etc.)^{30,31,32}. There are only few examples of TM-AFM on blends from nanoparticles and (conjugated) polymers. One possible reason might be that in most mixed nanoparticle:polymer systems, mixing problems lead to very rough surfaces, which makes interpretation of phase images rather difficult³³. In theory, these hybrid mixtures would be ideal candidates to study with TM-AFM because the hard nanoparticles can easily be distinguished from the soft polymer. In one TM-AFM study on SiO₂ nanoparticles in a PVP (poly[n-vinyl-2-pyrrolidone]) film, it has been reported that it appears to be possible to detect SiO₂ particles 5-7 nm beneath the surface of the PVP film³⁴.

Performing TM-AFM on *nc*-ZnO:MDMO-PPV blends might give some insight into the relation between the amount of ZnO and the performance of the photovoltaic device. In chapter 4, a clear optimum of the photovoltaic effect around 30 vol.-% ZnO in the blend was demonstrated. Small amounts of ZnO in the blends do not lead to the generation of a sufficient amount of charges, as is apparent from the low short circuit currents of these devices and the low photoluminescence quenching observed for these blends.

TM-AFM recorded on blends with 8 vol.-% ZnO (figure 5.12) show a clear dependence on tapping force. The phase shift of the cantilever oscillation can be related to the power dissipated in a non-elastic tip-sample interaction^{35,36}. A hard material generally shows a positive phase shift with respect to a soft material, therefore the bright areas in figure 5.12 are interpreted as the harder materials, and the dark areas as the softer materials.

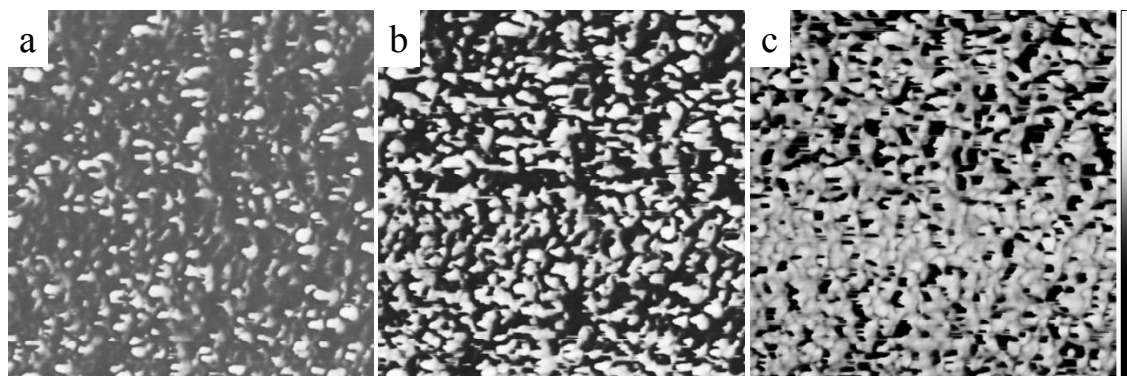


Figure 5.12 TM-AFM phase images (500 nm × 500 nm) of *nc*-ZnO:MDMO-PPV blends with 8 vol.-% ZnO bar 200°. The tapping force has been varied from (a) $I/I_0 = 0.6$ (lowest force) to (b) $I/I_0 = 0.5$ and (c) $I/I_0 = 0.45$ (highest force), where I_0 is the target amplitude and I the cantilever amplitude during image recording.

The TM-AFM phase images in figure 5.12 show the effect of the tapping force on the phase image. Soft tapping (image a) shows a mostly soft material. Upon increasing the tapping force (images b and c) more of a hard material is visible. The images can only be interpreted by assuming that there is a soft layer of MDMO-PPV on top of a harder material; this seems a rather homogeneous mixture of the hard ZnO nanoparticles and the MDMO-PPV. Upon increasing the tapping force this surface layer is penetrated and the harder underlying material is observed, as is reflected by a positive phase shift. These phase images are completely reversible by reversing the tapping force.

In the height images the ‘disappearance’ of the top layer by harder tapping can be observed, an example is shown in figure 5.13 for an *nc*-ZnO:MDMO-PPV blend having 4 vol.-% ZnO.

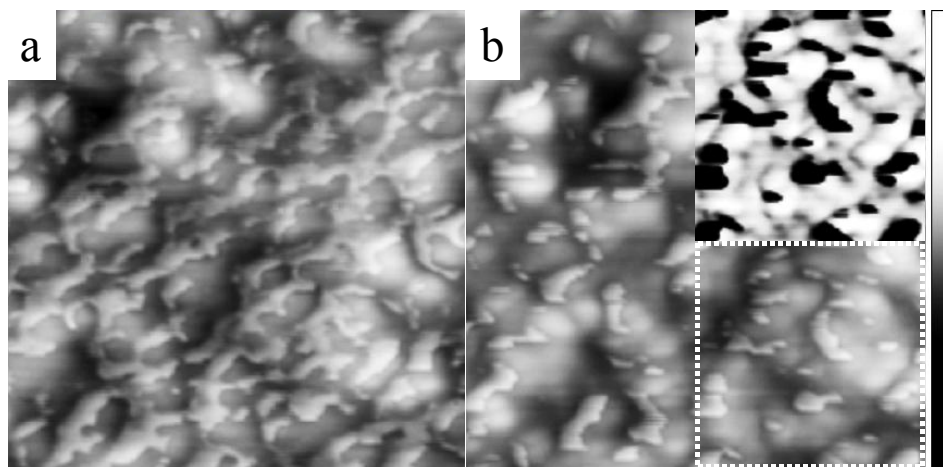


Figure 5.13 TM-AFM height images ($500 \text{ nm} \times 500 \text{ nm}$) of *nc*-ZnO:MDMO-PPV blends with 4 vol.-% ZnO, the bar indicates 40 nm. a) soft tapping, $I/I_0 = 0.6$ b) harder tapping, $I/I_0 = 0.4$. The inset shows a phase image of the section bound by the dotted line.

TM-AFM height images of *nc*-ZnO:MDMO-PPV blends containing 4 vol.-% of ZnO (figure 5.13) show a soft top layer of 1-2 nm in height (as estimated from the height cross-sections). This top layer has been observed in most samples but is the thickest in samples that contain a high amount of MDMO-PPV. This must be a pure MDMO-PPV film because the 5 nm sized ZnO nanoparticles can not be imbedded in this very thin film. In figure 5.13a a part of this top layer can be observed, the surface of the blend appears partially wetted with a thin film. After increasing the tapping force (see figure 5.13b) a part of this layer appears penetrated and is no longer visible in the height image. The part of the surface layer that remains visible in the height image, appears dark in the phase image (see the inset in figure 5.13b), *i.e.* this appears to be a soft material. This effect on the height and phase images is completely reversible; decreasing the tapping force shows a ‘restoration’ of this layer.

This surface layer appears to be more pronounced in the blends with large amounts of MDMO-PPV. This might add up to the observation that these blends show a smaller photovoltaic effect. The presence of a polymer layer between the active blend and the top electrode will act as a blocking layer for electron injection into this electrode, and therefore leads to lower currents under illumination. It has also been observed that the polymer layer increases in thickness when the blend is stored (in a glovebox), probably because of diffusion of the polymer towards the air interface.

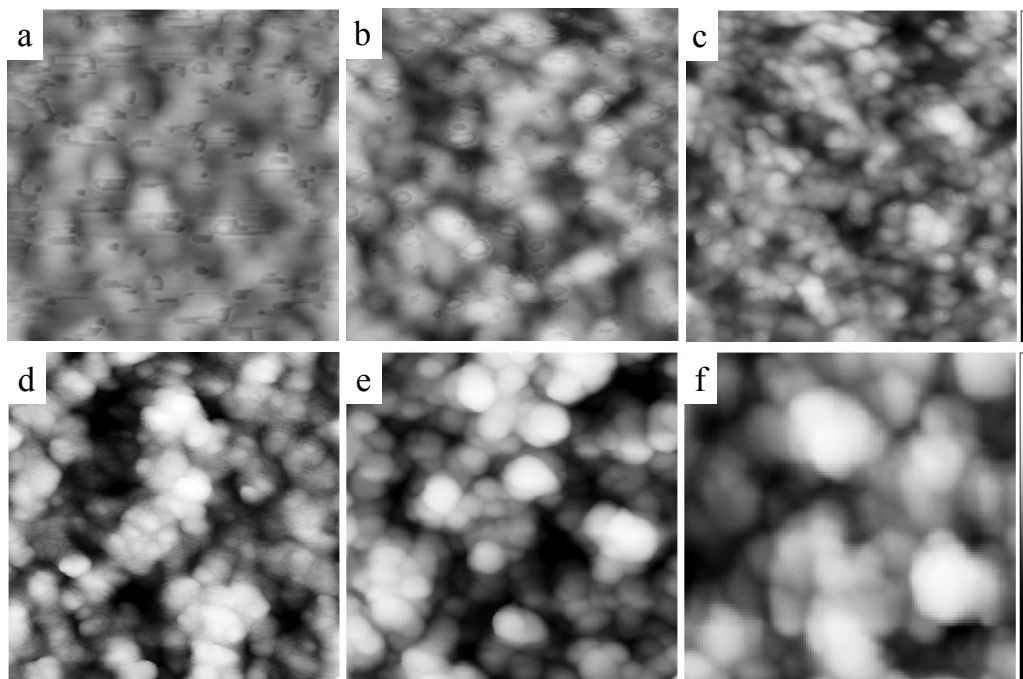


Figure 5.14 TM-AFM height images (500 nm \times 500 nm), a-c 50 nm height bar and d-f 100 nm height bar a) 8 vol.-% ZnO, 70 nm thick, 3 vol.-% MeOH; b) 15 vol.-% ZnO, 90 nm thick, 3 vol.-% MeOH; c) 26 vol.-% ZnO, 140 nm thick, 4 vol.-% MeOH; d) 42 vol.-% ZnO, 220 nm thick, 5 vol.-% MeOH; e) 49 vol.-% ZnO, 240 nm thick, 7 vol.-% MeOH; f) 64 vol.-% ZnO, 350 nm thick, 10 vol.-% MeOH.

Although intriguing, this surface layer makes interpretation of the phase images challenging. Soft tapping is required to get a proper view on the actual surface morphology of these blends, because the topology of the samples is in some cases disturbed when larger tapping forces have been applied. The effect of the ZnO content on the surface morphology of the blends is shown in figure 5.14. Only height images are shown because the phase images for a-d (under soft tapping conditions) do not reveal phase contrast other than due to the presence of the surface layer. In images e and f no surface layer has been observed, and the material appears to consist of a single homogeneous phase.

Images of blends with low amounts of ZnO (figure 5.14a, 8 vol.-%) show a smooth surface, with a faint appearance of spherical aggregates. Images b and c show that upon increasing the ZnO content these faint structures are replaced by more sphere-like structures. Increasing the ZnO content above 20 vol.-% results in coagulation, growth of the spherical structures, and a significant increase in surface roughness. The peak-to-peak Z-range and the RMS-roughness as function of the volume percent ZnO of the blends (figure 5.15), show that increasing the amount of ZnO over 26 vol.-% leads to a steep increase of the surface roughness. From the AFM surface topology for blends with more than 15 vol.-% ZnO the impression is that the film consists of an agglomerate of these spherical structures. It is possible that these have already been formed in solution prior to spin casting and that upon removal of the solvent the remaining polymer chains in solution adhere to the outside of the spherical aggregates.

Kwong *et al.*¹¹ have measured TM-AFM on blends from TiO₂ and *rr*-P3HT, these blends appeared extremely rough but also showed a sphere-like aggregate formation. Huynh *et al.*¹⁰, performing TM-AFM on CdSe:*rr*-P3HT blends, do not observe the formation of structures but observe a morphology effect (roughening) due to the amount of co-solvent (pyridine) present in the solution used for films preparation. There appears to be an optimal amount of pyridine to dissolve the nanoparticles together with the polythiophene in

chloroform. Too low and too high amounts of pyridine lead to rough surfaces and a poor photovoltaic effect. The effect of methanol, which serves a similar function in the *nc*-ZnO:MDMO-PPV blends as the pyridine in the CdSe:*rr*-P3HT blends, has not been investigated in great detail. However, the largest differences observed with TM-AFM on the morphology (surface roughness and aggregate formation) appear between 26 and 42 vol.-% ZnO (images c and d). The methanol content in solution increases from 4% to 5%, and is not likely responsible for the observed changes in morphology. Compared to regioregular polythiophenes, MDMO-PPV allows a much wider operating window in terms of the amount of methanol.

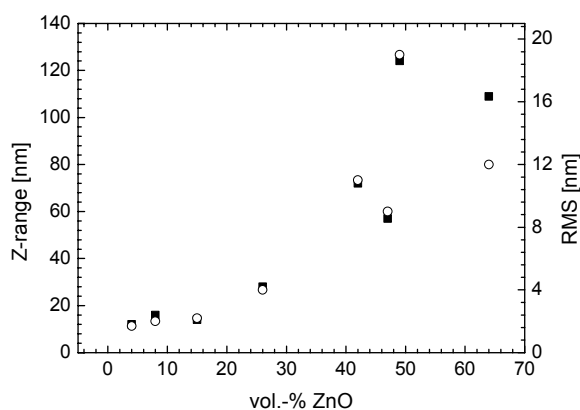


Figure 5.15 Z-range (■) and RMS roughness (○) as function of the vol.-% ZnO in *nc*-ZnO:MDMO-PPV blends.

5.4 Conclusions

The UV-vis measurements indicate that the optical absorption of the *nc*-ZnO:MDMO-PPV blends is a linear combination of the optical properties of the components. The amount of ZnO nanoparticles in the solution used for spin casting correlates with the amount actually observed in the blend. Upon addition of ZnO to MDMO-PPV, 85% of the photoluminescence of the latter is quenched. This quenching indicates an effective photoinduced charge separation. Photoinduced absorption spectroscopy performed on blends of MDMO-PPV or *rr*-P3HT with ZnO nanoparticles showed the formation of radical cations on the conjugated polymer and the presence of injected electrons in the ZnO nanoparticles. The kinetics of this charge separation has been studied with pump-probe spectroscopy. Charge separation occurs within 1 ps, illustrating an ultrafast electron transfer to the ZnO nanoparticle. As is apparent from the near steady-state PIA, the photoinduced charges live long, which is confirmed by hole burning spectroscopy and FP-TRMC measurements. FP-TRMC allows an evaluation of the transient microwave conductivity in these blends, which has been studied as a function of the amount of ZnO. It appears that the observed increase of the conductivity in the blends with increasing amounts of ZnO can be attributed to an increase of the amount of charge carriers. Addition of ZnO nanoparticles to regioregular polythiophene seems to create disorder in the polythiophene chains close to the ZnO nanoparticle. In solar cells made from *nc*-ZnO:*rr*-P3HT blends the fast geminate recombination is likely responsible for a lower effective charge generation compared to *nc*-ZnO:MDMO-PPV based solar cells. Annealing of the *nc*-ZnO:*rr*-P3HT blends leads to an improved photovoltaic effect, presumably due to an improved stacking of P3HT chains in the vicinity of the ZnO nanoparticles.

The morphology of the *nc*-ZnO:MDMO-PPV blends has been examined with TEM and TM-AFM. With TM-AFM a thin layer covering the surface has been identified as MDMO-PPV. It appears difficult to correlate the TM-AFM to the TEM pictures; the increase in surface roughness certainly implies that conclusions on the TEM must be drawn carefully. However the TEM image of a thin film clearly shows MDMO-PPV domains without ZnO. This phase-separated system cannot properly be observed with TM-AFM. The spherical aggregates observed with TM-AFM, cannot clearly be observed in the TEM pictures. Both the TEM and the TM-AFM show that small amounts of ZnO can be rather homogeneously blended with MDMO-PPV and that the size of the aggregates and the roughness of the films increase when the amount of ZnO in the blend has been raised. The trends observed in chapter 4 for the photovoltaic effect as a function of the vol.-% ZnO in the blend, can partially be described with the TM-AFM observations. In the initial homogeneous mixture (figure 5.14a, 8 vol.-% ZnO) the ZnO nanoparticles are apparently not agglomerated enough for a proper transport of electrons. According to the photoluminescence quenching experiments, such a low amount of ZnO also does not lead to the generation of a sufficient amount of charges. Upon addition

of more ZnO, clear spherical aggregates are formed and these appear interconnected. Increasing the ZnO amount further leads to rough films; the 64 vol.-% ZnO blend (350 nm thick) has a surface height difference of approximately 100 nm. Solar cells made from these films likely contain pinholes (shunts). This observation can be linked to the lowering of the V_{OC} when the amount of ZnO has been raised (chapter 4, figure 4.6). One other observation is, that the rough phase, being formed in blends with high amounts of ZnO, appears homogeneous because no phase contrast could be identified. This implies that within the spherical aggregates the MDMO-PPV is well mixed with the ZnO nanoparticles. MDMO-PPV therefore gets highly diluted when the amount of ZnO increases; this lowers the hole transport properties of these blends. A drop in the short circuit current of the corresponding solar cells indeed has been observed in chapter 4.

In summary, these results give a better understanding of the optical and electro-optical properties of *nc*-ZnO:conjugated polymer blends. A start has been made to understand the effects of the amount of ZnO on the properties of the composite. Photoluminescence spectroscopy, FP-TRMC, TEM and TM-AFM give insight in the complex interplay between inorganic nanoparticles and conjugated polymers. A deeper understanding of the complex morphology of these systems will certainly aid in improving the photovoltaic effect in further studies on this combination of materials.

5.5 Experimental

UV-vis absorption and photoluminescence spectroscopy: UV-vis spectra were recorded on a Perkin-Elmer Lambda 900 spectrophotometer. Photoluminescence spectra were recorded on an Edinburgh Instruments FS920 double-monochromator spectrometer with a Peltier-cooled red-sensitive photomultiplier. Time-correlated single photon counting photoluminescence studies were performed using an Edinburgh Instruments LifeSpec-PS consisting of a 400 nm picosecond (pulse width ~ 50 ps) laser (PicoQuant PDL 800B) operated at 2.5 MHz and a Peltier-cooled Hamamatsu micro-channel plate photomultiplier (R3809U-50). The *nc*-ZnO:MDMO-PPV blends from chlorobenzene solution (contained 3 mg mL^{-1} MDMO-PPV) were cast (at 1500 rpm) onto PEDOT:PSS covered ITO plates, for the UV-vis experiments, and on glass plates for the photoluminescence experiments. The F_A values that were used to correct the TRMC intensity were measured using a Perkin-Elmer Lambda 900 spectrophotometer with an integrating sphere, to measure the fraction of incident light reflected and transmitted by the sample.

Near steady-state photoinduced absorption (PIA): Spectra were recorded between 0.25 and 3 eV by exciting an *nc*-ZnO:MDMO-PPV film on quartz in an Oxford Optistat continuous flow cryostat at 80 K with a mechanically modulated (275 Hz) Ar-ion laser (Spectra Physics 2025) pump beam tuned to 488 nm (25 mW, beam diameter of 2 mm) and monitoring the resulting change in transmission (ΔT) of a tungsten-halogen white-light probe beam after dispersion by a triple grating monochromator, using Si, InGaAs, and (cooled) InSb detectors.

Pump-probe spectroscopy: The femtosecond laser system used for pump-probe experiments consisted of an amplified Ti/sapphire laser (Spectra Physics Hurricane), providing 150 fs pulses at 800 nm with an energy of 750 μJ and a repetition rate of 1 kHz. The pump pulses (510 nm) were created via optical parametric amplification (OPA) of the 800 nm and frequency doubling. The probe beam (2200 nm) was generated in a separate OPA. The pump beam was linearly polarized at the magic angle (54.7°) with respect to the probe beam, to cancel out orientation effects in the measured dynamics. The temporal evolution of the differential transmission was recorded using a cooled InSb detector by a standard lock-in technique at 500 Hz.

Hole-burning spectroscopy: Thin films of the *nc*-ZnO:MDMO-PPV composite material were obtained by spin coating from chlorobenzene solution on a quartz substrate. Transient hole burning spectra were recorded by exciting the sample with pulses at 450 nm (pulse width 4 ns, repetition rate 10 Hz) obtained from an optical parametric oscillator (OPO), pumped by the third harmonic of a Nd-YAG laser. The excited area was 1.8 mm^2 and the sample was held at 295 K in a flow cryostat in a N_2

atmosphere. An intensified CCD camera was used to record the transmission of a tungsten-halogen probe light through the sample after dispersion by a spectrograph. The signal acquisition by the camera was electronically gated. To obtain differential transmission spectra, the probe light was recorded at the delay time of interest and then the reference transmission at a 25 ms delay. For short acquisition delay times, the transmission spectra were corrected for a very small residual fluorescence.

FP-TRMC: Films of *nc*-ZnO:MDMO-PPV (from chlorobenzene) and *nc*-ZnO:*rr*-P3HT (from chloroform) were spin cast on quartz. The *nc*-ZnO:MDMO-PPV blends were cast at 1500 rpm for 2 minutes and 1 minutes at 2500 rpm. The *nc*-ZnO:*rr*-P3HT blends were cast at 1000 rpm for 1 minute. The samples were mounted in an X-band microwave cavity at a position corresponding to a maximum in the electric field strength of the standing wave pattern at resonance. The sample could be illuminated via a grating in the copper end plate of the cavity, which was covered and vacuum sealed with a quartz window. The iris-coupling hole of the cavity was sealed with a polyimide foil. The cavity was attached to a vacuum line and the air was replaced by a mixture of 10% SF₆ in CO₂ at atmospheric pressure to scavenge any free electrons which might be ejected from the film by photoelectron emission. For photoexcitation in the visible, the third harmonic of a Q-switched Nd:YAG (yttrium aluminum garnet) laser (“Infinity 15-30,” Coherent) was used to pump an optical parametric oscillator (OPO) yielding 3 ns full width at half maximum (FWHM) pulses continuously tunable from 420 to 700 nm. The beam was expanded using CaF₂ lenses to give a close to uniform intensity over a rectangular area of approximately 1 × 2 cm², close to the cross-sectional dimensions of the cavity and the sample. The integrated incident laser intensity, I_0 photons cm⁻² per pulse, was monitored by deflecting a small percentage of the light to the pyroelectric sensor of a Labmaster power meter.

TEM: Films for TEM were prepared by floatation onto the surface of deionized water and picked up by a 400 mesh copper grid. The TEM observations were conducted on a JEOL JEM-2000FX transmission electron microscope operated at an acceleration voltage of 80 kV.

TM-AFM: AFM tapping mode measurements were performed on a Veeco MultiMode with a NanoScope IV controller, using tapping-mode etched silicon probes. The film thickness was measured on a Tencor P-10 profilometer.

- 1 Blom, P. W. M.; Schoo, H. F. M.; Matters, M. *Appl. Phys. Lett.* **1998**, *73*, 3914.
- 2 Carter, S. A.; Scott, J. C.; Brock, P. J. *Appl. Phys. Lett.* **1997**, *71*, 1145.
- 3 Ho, P. K. H.; Friend, R. H. *J. Chem. Phys.* **2002**, *116*, 6782.
- 4 Bozano, L.; Tuttle, S. E.; Carter, S. A.; Brock, P. J. *Appl. Phys. Lett.* **1998**, *73*, 3911.
- 5 Hide, F.; Schwartz, B. J.; Díaz-García, M. A.; Heeger, A. J. *Chem. Phys. Lett.* **1996**, *256*, 424.
- 6 Salafsky, J. S. *Phys. Rev. B.* **1999**, *59*, 10885.
- 7 Petrella, A.; Tamborra, M.; Cozzoli, P. D.; Curri, M. L.; Striccoli, M.; Cosma, P.; Farinola, G. M. Babudri, F.; Naso, F. Agostiano, A. *Thin Solid Films* **2004**, *451-452*, 64.
- 8 Martens, T.; Munters, T.; Goris, L.; D'Hean, J.; Schouteden, K.; D'Olieslaeger, M.; Lutsen, L. Vanderzande, D.; Geens, W.; Poortmans, J.; De Schepper, L.; Manca, J. V. *Appl. Phys. A* **2004**, *79*, 27.
- 9 Van Duren, J. K. J.; Yang, X.; Loos, J.; Bulle-Lieuwma, C. W. T.; Sieval, A. B.; Hummelen, J. C.; Janssen, R. A. J. *Adv. Funct. Mater.* **2004**, *14*, 425.
- 10 Huynh, W. U.; Dittmer, J. J.; Libby, W. C.; Whiting, G. L.; Alivisatos, A. P. *Adv. Funct. Mater.* **2003**, *13*, 73.
- 11 Kwong, C. Y.; Djurišić, A. B.; Chui, P. C.; Cheng, K. W.; Chan, W. K. *Chem. Phys. Lett.* **2004**, *384*, 372.
- 12 The volume percent of ZnO has been determined from the amount of ZnO and MDMO-PPV in the solution, using the density of ZnO (5.6 mg mL⁻¹) and MDMO-PPV (0.91 mg mL⁻¹).
- 13 Savenije, T. J.; Kroeze, J. E.; Wienk, M. M.; Kroon, J. M.; Warman, J. M. *Phys. Rev. B.* **2004**, *69*, 155205.
- 14 Srikant, V.; Clarke, D. R. *J. Appl. Phys.* **1998**, *83*, 5447.
- 15 Vossmeier, T.; Katsikas, L.; Giersig, M.; Popovic, I. G.; Diesner, K.; Chemseddine, A.; Eychemüller, A.; Weller, H. *J. Phys. Chem.* **1994**, *98*, 7665.
- 16 Kwong, C. Y.; Choy, W. C. H.; Djurišić, A. B.; Chui, P. C.; Cheng, K. W.; Chan, W. K. *Nanotechnology* **2004**, *15*, 1156.
- 17 Van der Zanden, B.; Van de Knol, R.; Schoonman, J.; Goossens, A. *Appl. Phys. Lett.* **2004**, *84*, 2539.
- 18 Wei, X.; Vardeny, Z. V.; Sariciftci, N. S.; Heeger, A. J. *Phys. Rev. B.* **1996**, *53*, 2187.
- 19 Shim, M.; Guyot-Sionnest, P. *J. Am. Chem. Soc.* **2001**, *123*, 11651.
- 20 Pientka, M.; Wisch, J.; Böger, S.; Parisi, J.; Dyakonov, V.; Rogach, A.; Talapin, D.; Weller, H. *Thin Solid Films* **2004**, *451-452*, 48.
- 21 Pientka, M.; Dyakonov, V.; Meissner, D.; Rogach, A.; Talapin, D.; Weller, H.; Lutsen, L.; Vanderzande, D. *Nanotechnology* **2004**, *15*, 163.
- 22 Bauer, C.; Boschloo, G.; Mukhtar, E.; Hagfeldt A. *J. Phys. Chem. B.* **2001**, *105*, 5585.
- 23 Offermans, T.; Meskers, S. C. J.; Janssen, R. A. J. *J. Chem. Phys.* **2003**, *119*, 10924.
- 24 Experiments conducted at the Radiation Chemistry Department, IRI, Delft University of Technology, in cooperation with P. A. C. Quist and T. J. Savenije.

- 25 Given the frequency of the alternating microwave field (8.47 GHz) the electrons are swept by this alternating field over short distances, completely confined to the ZnO nanoparticle. Therefore the slow interparticle electron hopping process does not likely limit the measured mobility.
- 26 Calculations performed at the Radiation Chemistry Department, IRI, Delft University of Technology, show that when assuming a bulk electron mobility of $100 \text{ cm}^2 \text{ V}^{-1} \text{ s}^{-1}$, in a 5 nm sized ZnO nanocrystal a mobility of $10^{-3} - 10^{-4} \text{ cm}^2 \text{ V}^{-1} \text{ s}^{-1}$ can be expected.
- 27 A distinction has been made between the attenuation and absorption spectra of the blends. In contrast to the absorption spectra, the attenuation spectra have been corrected for reflection losses and are therefore a better approximation of the actual amount of photons attenuated in the film.
- 28 Transmission electron microscopy was performed by X. Yang, Polymer Technology, Department of Chemical Engineering and Chemistry, TU/e, and the Dutch Polymer Institute.
- 29 Zhang, J.; Wang, B.; Ju, X.; Liu, T.; Hu, T. *Polymer* **2001**, *42*, 3697.
- 30 Wang, Y.; Song, R.; Li, Y.; Shen, J. *Surf. Sci.* **2003**, *530*, 136.
- 31 Knoll, A.; Magerle, R.; Krausch, G. *Macromolecules* **2001**, *34*, 4159.
- 32 Basnar, B.; Friedbacher, G.; Brunner, H.; Vallant, T.; Mayer, U.; Hoffmann, H. *Appl. Surf. Sci.* **2001**, *171*, 213.
- 33 TM-AFM experiments on *nc*-ZnO:rr-P3HT blends actually showed a nice example of such a system: these blends appeared extremely rough, phase and even height images were difficult to interpret.
- 34 Feng, J.; Weng, L-T.; Chan, C-M.; Xhie, J.; Li, L. *Polymer* **2001**, *42*, 2259.
- 35 Cleveland, J. P.; Ancykowski, B.; Schmid, A. E.; Elings, V. B. *Appl. Phys. Lett.* **1998**, *72*, 2613.
- 36 Garcia, R.; Tamajo, J.; Calleja, M.; Garcia, F. *Appl. Phys. A* **1998**, *66*, S309.

Chapter 6

Hybrid ZnO:polymer bulk heterojunction solar cells from a ZnO precursor

Abstract

This chapter describes a simple and new method to create hybrid bulk heterojunction solar cells consisting of ZnO and conjugated polymers. A gel-forming ZnO precursor, blended with conjugated polymers, is converted into crystalline ZnO at temperatures as low as 110°C. In-situ formation of ZnO in MDMO-PPV leads to a quenching of the polymer photoluminescence. Positive charges on the MDMO-PPV are formed after photoexcitation, indicating electron transfer from the polymer to ZnO. Results without full optimization already give photovoltaic cells with an estimated performance over 1% under AM1.5 illumination. The large effect of the processing conditions on the photovoltaic effect of the solar cells, indicate that there are several parameters that require control. The choice of solvent, type of atmosphere, and the relative humidity during spin coating, are important for optimization of the photovoltaic effect. These solar cells are made from cheap materials, and via simple processing and can be regarded as promising for further research.

6.1 Introduction

Bulk heterojunction solar cells have been demonstrated using CdSe, TiO₂, or ZnO nanoparticles as the inorganic phase^{1,2,chapter 4}. Pre-synthesizing nanoparticles offers the advantage of tailoring size, shape, and crystallinity and therefore allowing control over the optical and electronic properties of the materials. However, a reasonable degree of solubility in a solvent suitable for both the nanoparticle and the conjugated polymer is required for successful blending. This often requires the use of special solvents, additives or surfactants, which limit the processing window. On the other hand, many molecular precursors for inorganic materials are soluble in organic solvents and miscible with polymers. Therefore the in-situ synthesis of inorganic materials by a precursor route is an interesting alternative to the pre-synthesized nanoparticle route. Previous work^{3,4,5} has been directed to the synthesis of TiO₂ networks in films from MDMO-PPV and P3OT, using Ti(*i*-PrO)₄ as a precursor. It has been shown that a network of TiO₂ inside the polymer is actually formed, and that this polymer:TiO₂ bulk heterojunction can be used as the active layer in a photovoltaic device. The maximum calculated AM1.5 efficiency was 0.22 % for the MDMO-PPV:TiO₂ combination. The TiO₂ network, formed at room temperature, consists of amorphous TiO₂ and further improvements can be expected when this would be converted into a crystalline phase. Crystallization of TiO₂ however requires very high temperatures, with a minimum of 350 °C⁶. These high temperatures make it virtually impossible to convert TiO₂ into crystalline material in the presence of polymeric materials.

On the other hand, ZnO crystals have been formed at temperatures as low as 4 °C⁷. Replacing TiO₂ with ZnO may lead to the combination of crystalline inorganic semiconductors and polymers and is expected to outperform the solar cells based on amorphous TiO₂ networks. The challenge is to find a precursor for ZnO that is miscible with conjugated polymers and that can be converted to crystalline ZnO. In this chapter such a ZnO precursor is presented that enables the creation of a novel bulk heterojunction polymer:ZnO solar cell by simple spin coating and thermal treatment. This way a well performing solar cell is developed without the mixing problems encountered with blends from pre-synthesized nanoparticles and conjugated polymers.

6.2 Sol-gel chemistry using ZnO precursors

The principle of the method used in this chapter to make crystalline ZnO from a precursor is based on common sol-gel chemistry, where a precursor for metal oxides is treated in a suitable solvent/stabilizer mixture. Addition of water, acids, or other compounds triggers a hydrolysis reaction. The stabilizer decreases the rate of hydrolysis compared to the rate of condensation. In a typical sol-gel process both hydrolysis and condensation take place, and their rates depend on the solvent, stabilizer, and temperature. When these two rates are well balanced, the material forms a stable gel during solvent evaporation. Commercial zinc-salts, e.g. Zn(CH₃COO)₂·2H₂O and Zn(NO₃)₂ are not

suitable as ZnO precursor because these stable salts do not dissolve in apolar solvents nor hydrolyze upon exposure to moisture. Conversion of these salts into ZnO will not take place at low temperatures. On the other hand, organozinc compounds like dimethylzinc (ZnMe_2) and diethylzinc (ZnEt_2) rapidly hydrolyze. These volatile and reactive compounds are mainly used in metal-organic chemical vapor deposition (MOCVD) techniques⁸. Tests performed on ZnMe_2 and ZnEt_2 confirmed that hydrolysis was too rapid for application. Attempts to make gels from the pure precursors failed as only very rough and scattering films were obtained. For application in a solar cell it is necessary to have a smooth film, *i.e.* not having aggregates bigger than the film thickness (~ 100 nm). Solar cells with such aggregates will likely show shunts and not have a good performance. Stabilization of toluene based ZnMe_2 and ZnEt_2 solutions, *i.e.* slowing down the rate of hydrolysis, can be performed by the addition of triethylamine⁹ (TEA) and acetylacetone. Addition of 1 equivalent of acetylacetone and 4 equivalents TEA indeed leads to the formation of a gel and a transparent film after solvent evaporation. Removing this strongly chelating acetylacetone after hydrolysis requires high temperatures, making this combination of stabilizers not suitable for in situ low temperature ZnO formation. Addition of tetrahydrofuran (THF) to toluene solutions of ZnMe_2 and ZnEt_2 appears sufficient to stabilize these precursors and to obtain smooth and transparent films. Stabilization of ZnO precursors with THF is a very simple procedure and is compatible with most conjugated polymers.

6.3 Conversion of the precursor into crystalline ZnO

Transparent spin cast films of ZnMe_2 from toluene-THF mixtures exposed to moisture from ambient air do not show the formation of ZnO as inferred from the lack of absorption above 250 nm in the UV part of the absorption spectrum shown in figure 6.1. Molecular orbital calculations on the formation of ZnO from ZnEt_2 during chemical vapor deposition have shown that hydrolysis into zinc hydroxide is facile but the condensation step into ZnO is endothermic¹⁰. Hence, the rate of condensation is expected to be slow compared to the rate of hydrolysis, but can be increased by raising the

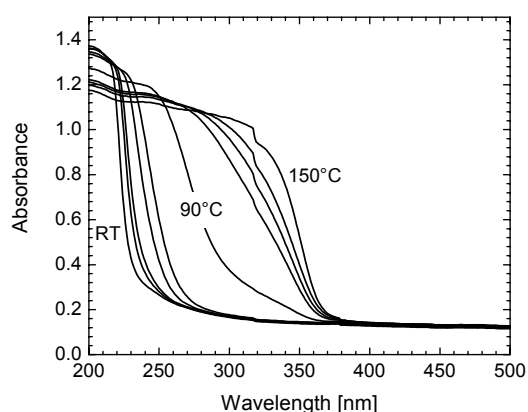


Figure 6.1 UV-vis spectra of a film prepared by spin casting a solution of ZnMe_2 in toluene:THF ($v:v = 1:5$) and, conversion of the hydroxide, formed upon exposure of the stabilized precursor to moisture, into ZnO by thermal treatment.

temperature. Condensation of the hydroxide, formed after exposure of ZnMe_2 to moisture, into ZnO by thermal treatment has been monitored with UV-vis spectroscopy as is shown in figure 6.1.

At room temperature only absorption below 250 nm is visible, attributed to Zn(OH)_2 and its condensation products. However, at temperatures as low as 90 °C the hydroxide is further condensed into ZnO , as is apparent from the shift of the onset of absorption. These relatively low temperatures are compatible with the conversion of this precursor in the presence of conjugated polymer.

After hydrolysis and condensation of the ZnMe_2 or ZnEt_2 at 110 °C, a crystalline material corresponding to wurtzite type ZnO is detected with XRD¹¹. Figure 6.2 shows the diffraction peaks, which appear significantly broadened. Using the Scherrer formula¹² an estimated size of the ZnO crystals of 6 ± 1 nm is obtained.

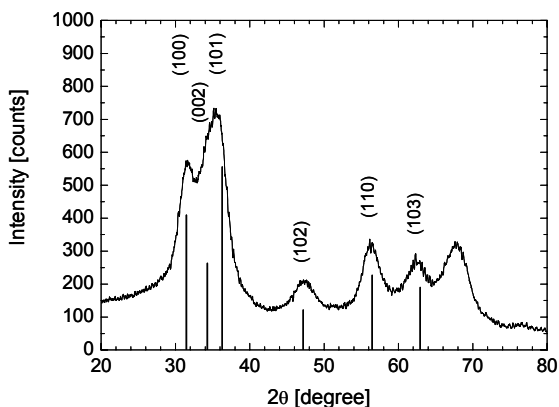


Figure 6.2 XRD spectrum of ZnO prepared from ZnMe_2 from a toluene:THF (v:v =1:5) solution, annealed in air at 110°C.

6.4 ZnO precursor : MDMO-PPV blends

Spin coating ZnMe_2 :MDMO-PPV mixtures gave poor reproducibility and only led to small amounts of ZnO after conversion. This is believed to be due to evaporation of the highly volatile ZnMe_2 during the spin coat step. Evaporation could be prevented using the less volatile ZnEt_2 . Blends of MDMO-PPV and ZnEt_2 (from hereon called *prec-ZnO*:MDMO-PPV blends) have been prepared using the procedure described in the experimental section. The relative amounts of chlorobenzene, tetrahydrofuran (THF), and toluene in the solutions that are used for spin coating are indicated in table 6.1. These amounts depend on the amount of ZnEt_2 added. The volume percentage of ZnO in the blend has been calculated from the amount of ZnEt_2 , assuming full conversion and a relative density of 5.6 g cm^{-3} for the ZnO and 0.91 g cm^{-3} for the polymer¹³. The MDMO-PPV concentration in the solution is kept constant.

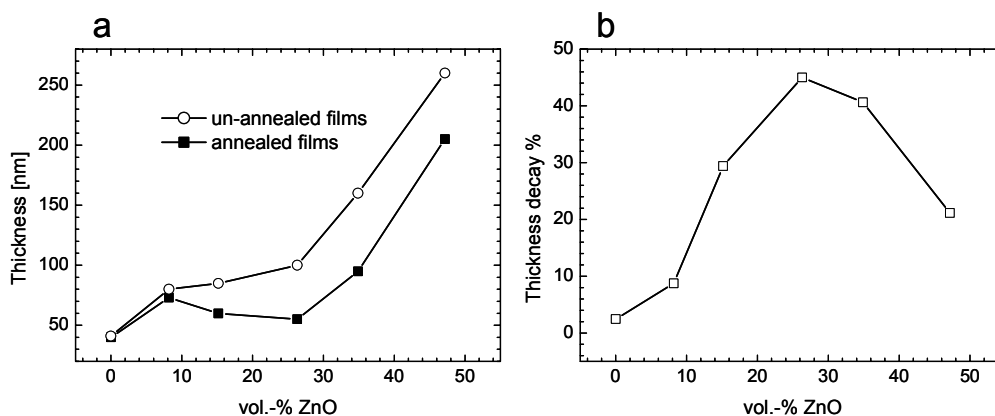
Table 6.1 The composition of the solution used for film preparation, as a function of the vol.-% ZnO in the film. The MDMO-PPV concentration was 3 mg mL⁻¹.

vol.-% ZnO (film)	vol.-% chlorobenzene	vol.-% THF	vol.-% toluene
8	95	3	2
15	91	6	3
26	81	12	7
35	72	18	10
47	53	30	17

These mixtures have been spin cast in air and aged for 15 minutes in N₂ at a relative humidity of 40%. Condensation into ZnO (annealing) has been performed for 30 minutes at 110 °C in N₂ with a relative humidity of 40%. Annealing of blends with MDMO-PPV at 110 °C showed conversion into ZnO within 30 minutes.

6.4.1 Effect of annealing on the film thickness of *prec*-ZnO:MDMO-PPV blends

The film thickness of *prec*-ZnO:MDMO-PPV blends as a function of the volume percent of ZnO is shown in figure 6.3.

**Figure 6.3** a) Film thickness as function of the ZnO vol.-% in the *prec*-ZnO:MDMO-PPV blend, showing the effect of annealing. b) Shows the decay of the film thickness after annealing.

The film thickness of the blend increases when the amount of ZnO precursor increases. Upon condensation of Zn(OH)₂ (presumably the majority product formed after hydrolysis) into ZnO, the film shrivels as the more dense crystalline ZnO is formed. The decrease in film thickness upon annealing is the first indication that ZnO is formed. The nonlinear decrease in film thickness (figure 6.3b) reveals that thicker films, with more ZnO precursor, have not been completely converted. Because conversion has been performed at 110°C at a fixed time of 30 minutes it is reasonable to assume that for blends containing more ZnO precursor, longer annealing times are needed. An alternative explanation might be, that in blends which contain large amounts of precursor, already more condensation of the hydroxide has occurred before the anneal step.

6.4.2 Effect of precursor condensation on the optical properties of *prec*-ZnO:MDMO-PPV blends

UV-vis absorption spectra (figure 6.4) and photoluminescence spectra (figure 6.5) show the effect of annealing and the amount of ZnO on the optical properties of the blends.

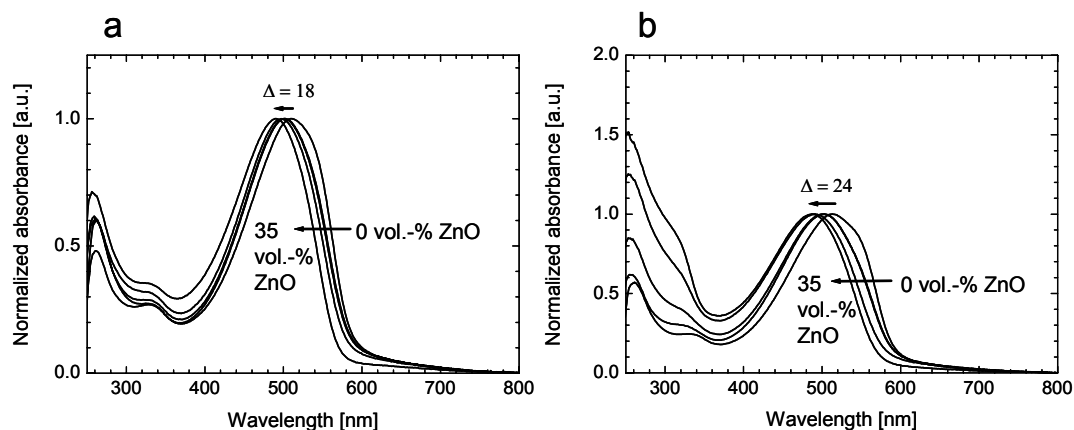


Figure 6.4 UV-vis absorbance spectra: (a) normalized spectra of un-annealed blends and (b) normalized spectra of films annealed at 110 °C.

Mixing in the ZnO precursor and allowing the films to hydrolyze in ambient, results in a blue shift of the absorption onset and absorption maximum of MDMO-PPV by 18 nm (figure 6.4a). In the UV part of the spectrum (figure 6.4a) some contribution of the $\text{Zn}(\text{OH})_2$ (presumably the major product) is observed, but there is no clear indication of ZnO. After conversion at 110 °C (figure 6.4b) the ZnO absorbance is apparent from the absorption onset at approximately 360 nm. The blue shift of the MDMO-PPV absorbance is more pronounced: 24 nm. These spectra do not reveal whether conversion into the ZnO has been completed. The observed blue shift is at least to some extent due to partial degradation of the polymer, since similar blue-shifts have been observed for MDMO-PPV which has been redissolved from a *prec*-ZnO:MDMO-PPV film. Though this degradation is clearly not desirable, it does not preclude well working devices. The difference in blue shift can also partially be due to a difference in stacking of the MDMO-PPV in the blends or due to a different dielectric constant of the surrounding medium.

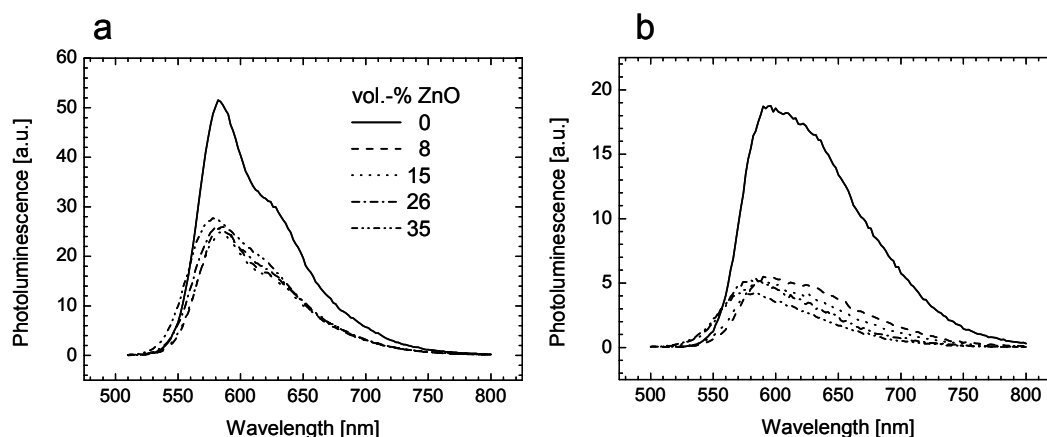


Figure 6.5 Photoluminescence spectra recorded for (a) un-annealed *prec*-ZnO:MDMO-PPV blends and (b) annealed *prec*-ZnO:MDMO-PPV blends. The photoluminescence is corrected for the excitation light intensity and the optical density at the excitation wavelength, set at the maximum of the MDMO-PPV absorption.

The effect on the photoluminescence of MDMO-PPV caused by the amount of ZnO in the blend is shown in figure 6.5a. Before annealing, the photoluminescence of the blends has decreased compared to pristine MDMO-PPV. All blends show an additional decrease of the photoluminescence intensity after annealing, almost irrespective of the amount of ZnO in the blend (see figure 6.5b). The residual photoluminescence is $\sim 20\%$ of the photoluminescence of the pristine but annealed MDMO-PPV film. The observed shift in the UV-vis spectra is also reflected in the photoluminescence spectra. The emission of the blends shifts 5 nm to the blue before annealing and 20 nm after annealing. Quenching of the photoluminescence is a clear indication that photoinduced electron transfer occurs in these blends. The residual photoluminescence indicates that $\sim 20\%$ of the excitons do not reach a junction between the MDMO-PPV and the ZnO.

The effective photogeneration of charges, after annealing, is also supported by the photoinduced absorption spectra (figure 6.6) of the un-annealed and the annealed blends containing 26 vol.-% ZnO.

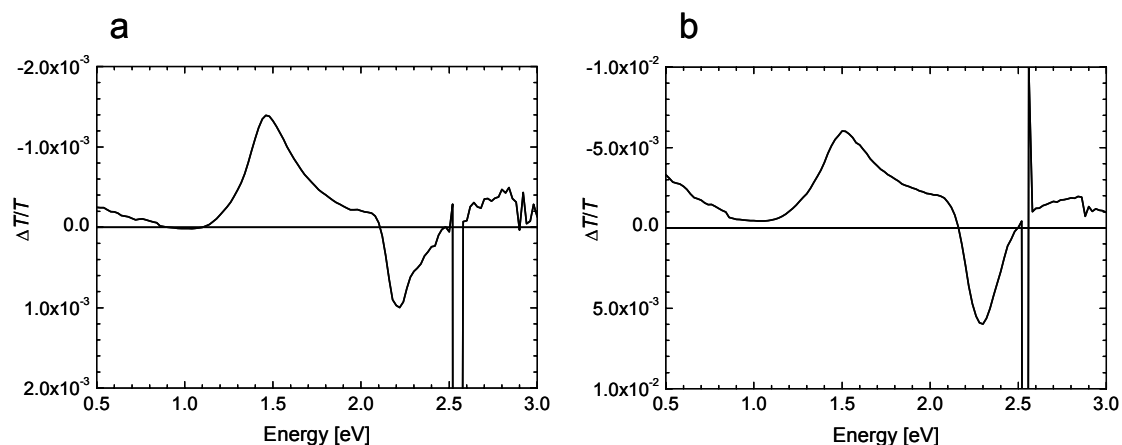


Figure 6.6 Photoinduced absorption spectra recorded by excitation at 488 nm. (a) On an un-annealed *prec*-ZnO:MDMO-PPV blend and (b) an annealed *prec*-ZnO:MDMO-PPV blend containing 26 vol.-% ZnO.

In figure 6.6a the band at 0.5 eV, is attributed to the photogeneration of radical cations on the MDMO-PPV, and probably to injected electrons into ZnO. This band is small compared to the signal at 1.5 eV, which is a combination of the transient absorption from a triplet and the radical cation on the MDMO-PPV. After annealing of the blend, the signals due to radical cations of the MDMO-PPV increase significantly and also relative to the triplet signal. This indicates an increased charge generation after annealing.

6.5 Photovoltaic effect in devices made from ZnO precursors and MDMO-PPV

6.5.1 Characterization of the photovoltaic effect

The presence of crystalline ZnO, combined with the photogeneration of charges, makes the *prec*-ZnO:MDMO-PPV blends interesting for application in solar cells. To test this, solutions containing ZnEt₂ and MDMO-PPV have been spin cast on pre-dried PEDOT:PSS covered structured ITO plates, and the resulting films have been annealed for 30 minutes at 110 °C in N₂ at a relative humidity of 40%. After deposition of an aluminum top electrode the current density-voltage characteristics have been determined in dark and under illumination by a simple tungsten halogen light source of approximately 0.87 Sun intensity¹⁴.

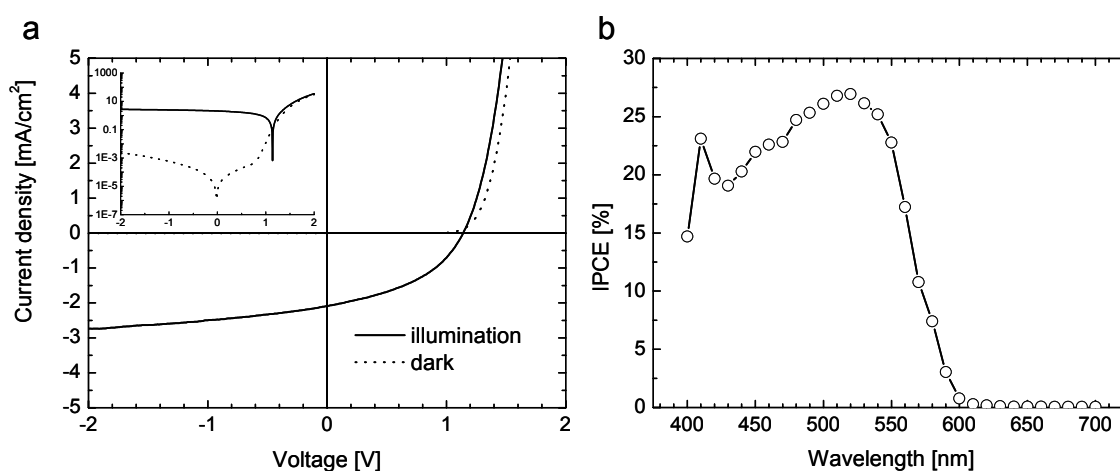


Figure 6.7 (a) Current density – voltage characteristics on *prec*-ZnO:MDMO-PPV blends (15 vol.-% ZnO), the inset shows a semi-logarithmic plot. (b) Incident photon to current efficiencies (IPCE) of the same solar cell.

The *J-V* characteristics for a *prec*-ZnO:MDMO-PPV device containing 15 vol.-% ZnO are shown in figure 6.7a. The thickness of the active layer was 100 nm and the optical density was 0.35 at the absorption maximum. Under illumination, the hybrid device gives a short-circuit current density (J_{SC}) of 2.0 mA cm⁻², an open-circuit voltage (V_{OC}) of 1.14 V, and a fill factor (FF) of 0.42. In the dark a high rectification ratio of over 1.2×10^{-4} (2V/-2V) has been obtained, indicating good diode behavior. Incident photon to current conversion efficiencies (IPCE) reach up to 27% at 520 nm monochromatic illumination. Integrating the IPCE data with the AM1.5 emission spectrum, gives a calculated J_{SC} of 2.3 mA cm⁻² and an estimated AM1.5 efficiency of 1.1%. This efficiency is a factor 5 higher than optimized cells based on TiO₂ precursors³. In contrast, the un-annealed blend shows only a very small photovoltaic effect with an J_{SC} of 0.05 mA cm⁻², a V_{OC} of 1.15 V and a fill factor of 0.18, giving a small maximum power-point (MPP) of 0.01 mW cm⁻². This demonstrates the necessity of annealing for obtaining efficient photovoltaic devices.

The stability of the device has been measured by continuous illumination under 0.87 sun intensity for 18 h, recording the current at 0.7 V (at the maximum power point of this device). The performance decreases to 88% of its original value (figure 6.8), indicating these solar cells are fairly stable¹⁵. In contrast to the solar cells based on ZnO nanoparticles as has been described in chapter 4, these solar cells withstand illumination (by small amounts) of ultraviolet light, *i.e.* no rapid degradation is observed.

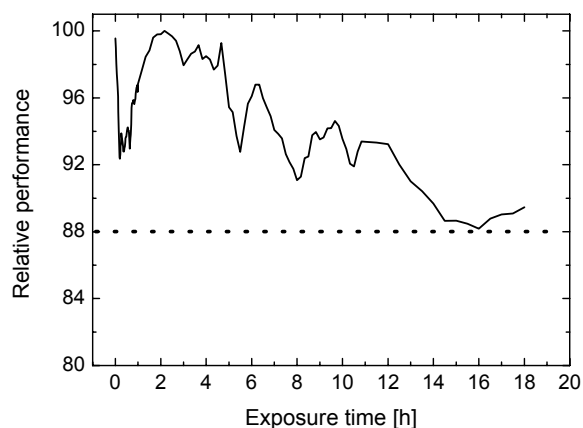


Figure 6.8 Relative decrease of the current at the maximum power point (0.7 V) of the device as characterized in figure 6.7. Illumination was performed continuously at approximately 0.87 sun intensity.

6.5.2 Effect of the processing parameters on the photovoltaic performance¹⁶

The conversion of the precursor into ZnO starts with a hydrolysis step and is likely dependent on the relative humidity. Controlling this relative humidity is of paramount importance. A controlled nitrogen atmosphere prevents degradation of the polymer during spin coating and annealing of the blend. Other relevant processing parameters like the effect of solvent and the amount of ZnO in the blend have also been studied.

Initial studies performed at ECN by Dr. L. Slooff showed that for MDMO-PPV synthesized following a precursor route¹⁷ better results were obtained when dissolving the polymer in toluene and chlorobenzene, compared to *p*-xylene and THF¹⁸. Because the best results were obtained for toluene, the effects of the relative humidity have been explored for toluene as solvent, the solvent after addition of the precursor stock solution contains 12 vol.-% THF. Both in toluene and chlorobenzene the optimal amount of ZnO in the blend appears to be 26 vol.-%, being slightly different from the work shown in section 6.5.1, where the optimal photovoltaic effect appeared at 15 vol.-% ZnO in the *prec*-ZnO:MDMO-PPV blend (using MDMO-PPV made via the Gilch route¹⁹).

The effect of the relative humidity during spin coating, on the performance of cells is shown in figure 6.9. These cells are prepared using toluene as solvent for the polymer and are annealed in nitrogen atmosphere at 100 °C at a relative humidity of 50-60%.

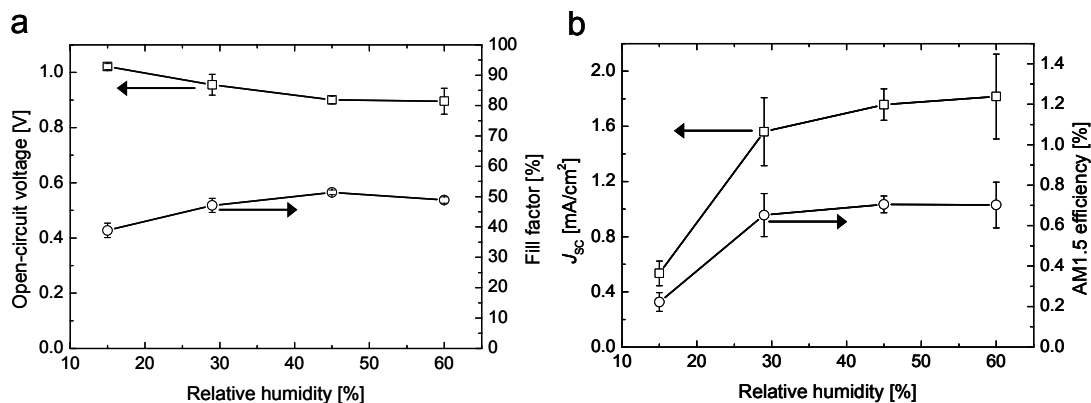


Figure 6.9 Effect on the photovoltaic response, of the relative humidity during the spin coating. (a) Open-circuit voltages (\square) and fill factors (\circ). (b) Short-circuit current density (J_{sc} , \square) and calculated AM1.5 efficiencies (\circ).

The relative humidity has a huge effect on the short-circuit current, only a slight effect on the open-circuit voltage and a small but positive effect on the fill factor. The overall trend is that increasing the humidity leads to an increase in performance. However at high relative humidity reproducibility is poor, due to a fast gelation of the solution during spincoating, *i.e.* leading to less homogeneous films.

6.6 Characterization of the morphology of *prec*-ZnO:MDMO-PPV blends¹⁶

As shown in the previous section, both hydrolysis and annealing conditions are of major importance for the performance of the photovoltaic cells. Tapping-mode AFM has been used to investigate the effects of hydrolysis, annealing, relative humidity, and the amount of ZnO on the morphology of the resulting films.

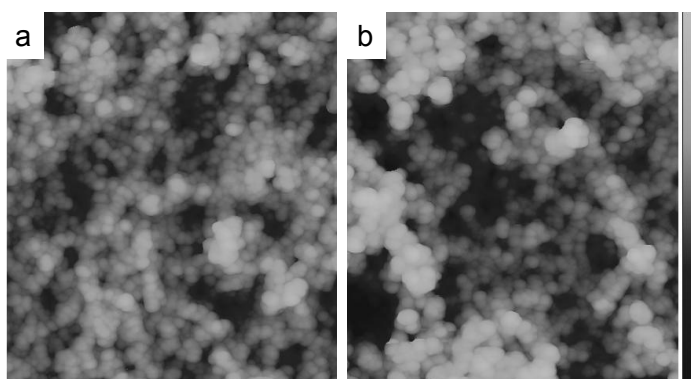


Figure 6.10 AFM tapping mode height images taken from (a) *prec*-ZnO:MDMO-PPV blend after hydrolysis in air and (b) after consecutive annealing at 110 °C also in air. Image size is 500 by 500 nm the height bar indicates 200 nm²⁰.

The morphology as visible with AFM is mainly determined by the hydrolysis step during spin coating (figure 6.10). The annealing mainly has an effect on the roughness of the film, which increases significantly. Spherical aggregates have already been formed during spin coating and do not seem to decrease in size upon condensation into crystalline ZnO. The 100-fold increase of the photovoltaic effect upon annealing cannot be visualized by morphology changes. These samples do not show a reproducible phase contrast when measuring the AFM phase image. No indication of phase separation could be obtained indicating a rather homogeneous mixing of the polymer and the ZnO in these spherical particles. Films spin cast and annealed in nitrogen, appear smoother than those spin cast in air. Hydrolysis in air is likely to be faster, leading to rougher surfaces. Changing the solvent for the polymer from chlorobenzene to toluene, does not affect the AFM images significantly.

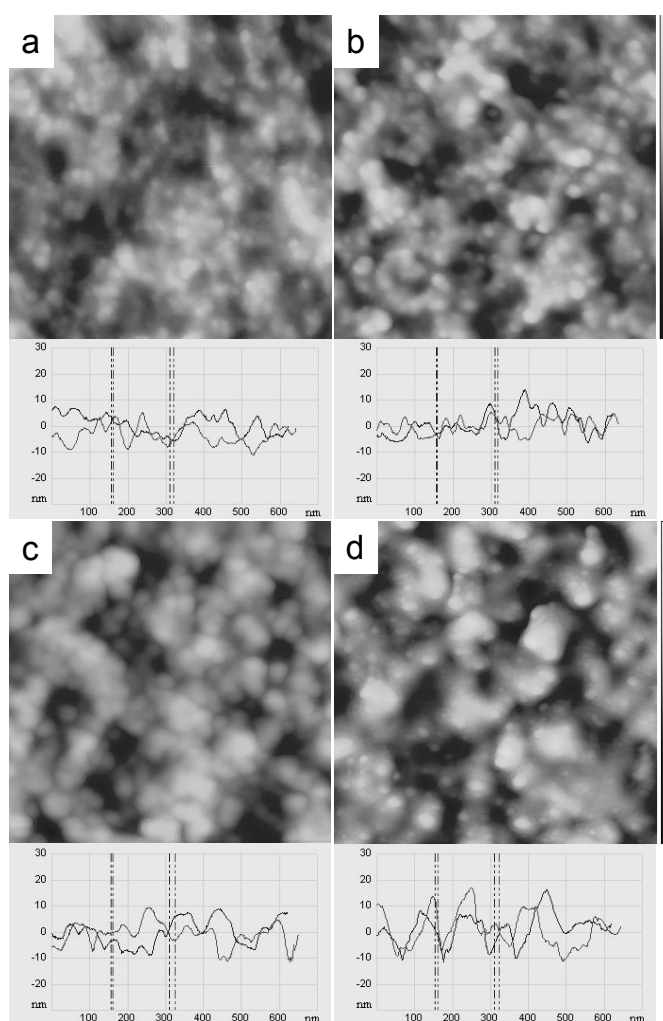


Figure 6.11 AFM tapping mode height images of *prec*-ZnO:MDMO-PPV blends using toluene as solvent for the polymer (precursor route made MDMO-PPV), spin cast in nitrogen at different relative humidity (a = 15 %RH, b = 29% RH, c = 45% RH and d = 60% RH). All films have been annealed in nitrogen at 100 °C (60% RH). Image sizes are 500 nm × 500 nm, the height bar indicates 50 nm. The bottom images are line scans, which indicate the increase in surface roughness.

Increasing the relative humidity has a profound effect on the photovoltaic performance. The main effect apparent from figure 6.11, on the morphology of *prec*-ZnO:MDMO-PPV blends, is an initial increase of the size of the spherical particles (compare figure 6.11 a, b and c). At higher relative humidity the surface roughness increases slightly and the spherical particles agglomerate. The sphere-like structures appear much more aggregated when spin casting is performed at a higher relative humidity, this might explain the higher currents observed when the photovoltaic effects of these blends are compared in a photovoltaic device.

The effect of the addition of more ZnEt₂ to the polymer is more pronounced and leads to clear morphology changes. Figure 6.12 shows AFM height and scanning electron microscopy (SEM) images of *prec*-ZnO:MDMO-PPV blends with different amounts of ZnO.

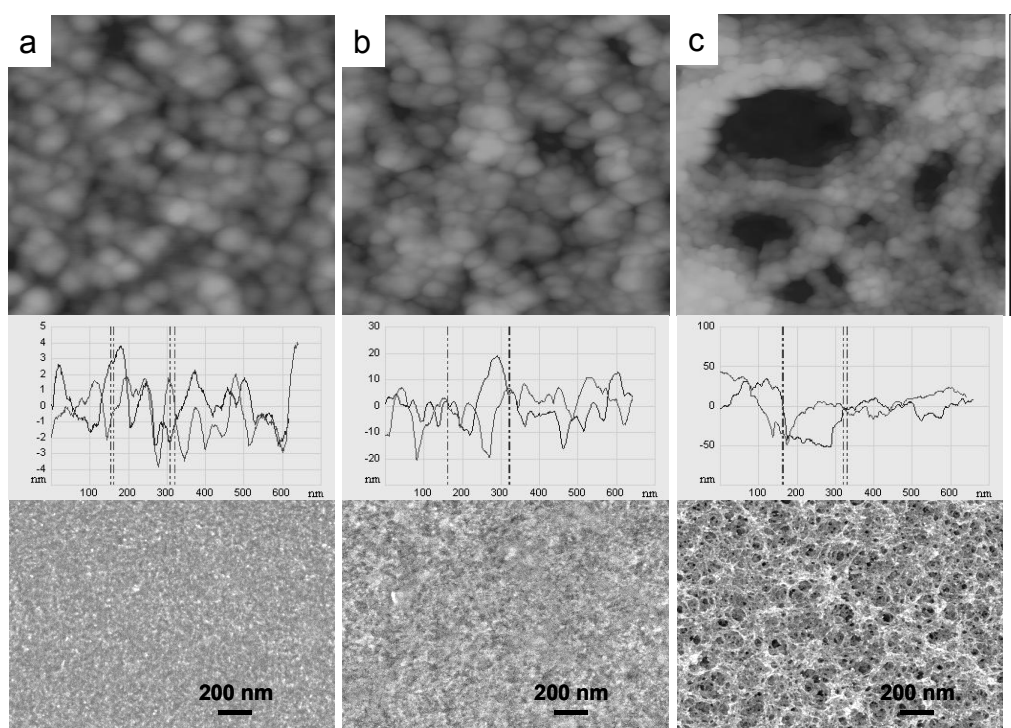


Figure 6.12 AFM tapping mode images (top), image size is 500 by 500 nm: a = 8 vol.-% ZnO (height scale = 25 nm), b = 26 vol.-% ZnO (height scale = 100 nm), c = 47 vol.-% ZnO (height scale = 150 nm), using Gilch type MDMO-PPV. AFM line-scan depth profiles (middle) and SEM images (bottom): a = 15 vol.-% ZnO, b = 26 vol.-% ZnO and c = 35 vol.-% ZnO, using precursor route MDMO-PPV.

Upon addition of more ZnO, the roughness of the films increases and the spherical structures seem to conglomerate into bigger aggregates. The roughening is also visible from the SEM pictures, already at a low ZnO-volume percentage of 35% the surface appears rough and cavities have been created. In blends containing low amounts of ZnO the ‘spheres’ appear only slightly interconnected, *i.e.* do not seem to be aggregated enough for efficient electron transfer. Increasing the amount of ZnO over 26 vol.-% leads to too rough films, with pinholes, and is also not likely the best morphology for solar

cells. Well performing photovoltaic cells have been constructed from blends with in between 15 and 26 vol.-% ZnO: from the intermediate region with a morphology as shown in picture 6.13b. Aggregates of the spherical structures are formed, but still rather smooth films are obtained.

The resemblance with the TM-AFM images of the *nc*-ZnO:MDMO-PPV blends shown in chapter 5 is striking. Apparently independently from the used route, blending conjugated polymers and ZnO leads to the same spherical structures.

6.7 Conclusions

Using simple sol-gel chemistry, ZnO precursors as ZnEt₂ and ZnMe₂ can be mixed with conjugated polymers leading to smooth non-scattering films. These ZnO precursors are easily converted into crystalline ZnO at 110 °C. Photoluminescence and photoinduced absorption spectroscopy reveal that after conversion of *prec*-ZnO:MDMO-PPV blends at 110°C, a significant amount of photogenerated charges is formed. Solar cells from these blends reach an estimated AM1.5 efficiency of > 1% and give external quantum efficiencies up to 27%. As such, these cells represent a significant improvement compared to cells made from precursor TiO₂^{3,4,5}.

Important parameters for optimization of this photovoltaic effect have been identified. Chlorobenzene and toluene appear the best choice of solvent. A nitrogen atmosphere prevents complete degradation of the polymer during the spin coating and the annealing steps. Controlling the humidity during spin coating appears of major importance for optimization of the photovoltaic effect. Trends in the *J-V* characteristics of solar cells indicate that a humidity of 40% during spincoating leads to the highest photovoltaic effect. AFM tapping mode demonstrates that the morphology can be tuned by choosing the right combination of the amount of ZnO precursor and the relative humidity. Increasing the amount of ZnO leads to bigger aggregates but also to rougher surfaces. The size of the spherical particles observed in the AFM images increases with increasing the relative humidity. Ultimately this also leads to bigger aggregates of the spherical particles.

Several parameters have been left virtually unexplored: it is likely that the condensation does not require (high) amounts of water (if hydrolysis is completed), but so far no attempts have been made to vary the relative humidity or the temperature in a controlled way during annealing. Not only the relative humidity has a huge effect on the speed of hydrolysis, but also the amount of THF added to the ZnO precursor is likely to be important, and needs further investigation. These novel polymer:ZnO bulk heterojunction solar cells require further study and analysis. The fact that an estimated AM1.5 efficiency of > 1% has been obtained after the first tests, raises the expectations of this new type of solar cell.

6.8 Experimental

Materials: The materials used were poly[2-methoxy-5-(3',7'-dimethyloctyloxy)-1,4-phenylenevinylene] (MDMO-PPV) synthesized via the Gilch-route and the Vanderzande route (precursor route MDMO-PPV)¹⁷, poly(3,4-ethylenedioxythiophene):poly(styrenesulfonate) (PEDOT:PSS) from Bayer AG (Baytron P VPAI 4083), aluminum wire (99.999%) from Engelhard-Clal. Diethylzinc (ZnEt₂) (1.1 M solution in toluene, Aldrich), and dimethylzinc (ZnMe₂) (2 M solution in toluene, Aldrich) were stored in a glovebox prior to use. Blends from MDMO-PPV and ZnEt₂ in chlorobenzene were prepared by dissolving the polymer (3 mg) in chlorobenzene (0.5 mL). A precursor stock solution was prepared by adding a ZnEt₂ solution (1.1 M in toluene, 1.8 mL) under argon atmosphere to dry THF (3.2 mL). Assuming full conversion, the amount of equivalents ZnO in this stock solution was calculated to be 32.2 mg mL⁻¹. The exact amount of stock solution needed to reach the desired amounts of ZnO in the blends was determined using this ZnO concentration in the precursor stock solution. Before addition of this stock solution, the correct amount of chlorobenzene was added to adjust the final volume to 1 mL.

Photovoltaic cell: Glass plates covered with patterned ITO resulting in 4 different device areas (0.095, 0.1167, 0.37, 1.02 cm²) were used for device preparation. Photovoltaic devices were fabricated by spin casting a solution of the *prec*-ZnO:MDMO-PPV mixture onto a pre-dried (30 minutes at 110 °C) poly(3,4-ethylenedioxythiophene):poly(styrenesulfonate) (PEDOT:PSS, Bayer AG) film on a UV-ozone cleaned indium tin oxide (ITO) coated glass substrate. For experiments determining the effect of the relative humidity on the photovoltaic performance, blends were spin cast in a controlled environment, allowing control of the medium (air or nitrogen) and the relative humidity. The back electrode, consisting of 100 nm Al, was evaporated in high vacuum. The photovoltaic device as characterized in section 6.5.1, was spin cast in air (RH = 35%) from a 3 mg mL⁻¹ MDMO-PPV and 3 mg mL⁻¹ ZnO (15 vol.-% ZnO) solution in chlorobenzene (containing 6 vol.-% THF and 3 vol.-% toluene). The blend was aged for 15 minutes in nitrogen with a relative humidity of 40% and was annealed for 30 min. at 110 °C in nitrogen at 40% relative humidity.

Current-voltage measurements: *J-V* measurements were performed in a N₂ atmosphere at room temperature. In forward bias the ITO electrode was positively biased. The devices were illuminated at the transparent ITO anode. *J-V* characteristics were measured with a computer-controlled Keithley 2400 Source Meter in the dark or under an estimated 0.87 sun equivalents (~87 mW cm⁻²) illumination from a 100 W tungsten-halogen lamp filtered by Schott KG01 and GG420 filters.

Incident photon to current conversion efficiencies (IPCE): Measurements were performed on a homebuilt set-up, utilizing a xenon lamp and a Spex minimate monochromator. The monochromatic light was focused on a diaphragm (2 mm in diameter) to create a small light spot for solar cell illumination. Light power intensity at 500 nm was 0.8 mW cm^{-2} as determined with a calibrated Melles-Griot silicon diode. Currents were recorded using a Keithley 2400 source meter.

Near steady-state photoinduced absorption (PIA): Spectra were recorded between 0.25 and 3 eV by exciting an *nc*-ZnO:MDMO-PPV film on quartz in an Oxford Optistat continuous flow cryostat at 80 K with a mechanically modulated (275 Hz) Ar-ion laser (Spectra Physics 2025) pump beam tuned to 488 nm (25 mW, beam diameter of 2 mm) and monitoring the resulting change in transmission (ΔT) of a tungsten-halogen white-light probe beam after dispersion by a triple grating monochromator, using Si, InGaAs, and (cooled) InSb detectors.

Other characterization techniques: X-ray powder diffraction measurements (XRD) were performed on a Rigaku Geigerflex with a Cu $K\alpha$ X-ray source operating at a tube voltage of 40 kV and a current of 30 mA. Absorption spectra were recorded on a Perkin-Elmer Lambda 900 spectrophotometer. Photoluminescence spectra were recorded on an Edinburgh Instruments FS920 double-monochromator spectrometer with a Peltier-cooled red-sensitive photomultiplier. AFM tapping mode measurements were performed on a Veeco MultiMode with a NanoScope IV controller, using tapping-mode etched silicon probes. The film thickness was measured on a Tencor P-10 profilometer. SEM measurements were performed on a JEOL JSM-6330F field emission scanning electron microscope with an accelerating voltage of 5 kV.

- 1 Huynh, W. U.; Dittmer, J. J.; Alivisatos, A. P. *Science* **2002**, *295*, 2425.
- 2 Kwong, C. Y.; Djurišić, A. B.; Chui, P. C.; Cheng, K. W.; Chan, W. K. *Chem. Phys. Lett.* **2004**, *384*, 372.
- 3 Van Hal, P. A.; Wienk, M. M.; Kroon, J. M.; Verhees, W. J. H.; Slooff, L. H.; Van Gennip, W. J. H.; Jonkheijm, P.; Janssen, R. A. J. *Adv. Mater.* **2003**, *15*, 118.
- 4 Slooff, L. H.; Wienk, M. M.; Kroon, J. M. *Thin Solid Films* **2004**, *451-452*, 634.
- 5 Slooff, L. H.; Kroon, J. M.; Loos, J.; Koetse, M. M.; Sweelssen, J. *Adv. Funct. Mater.* In press.
- 6 Okuya, M.; Nakade, K.; Kaneko, S. *Sol. Energy Mater. Sol. Cell* **2002**, *70*, 425.
- 7 Meulenkamp, E. A. J. *Phys. Chem. B.* **1998**, *102*, 5566.
- 8 Kim, H. W.; Kim, K. S.; Lee, C. J. *J. Mater. Sci. Lett.* **2003**, *22*, 1117.
- 9 O'Brien, P.; Malik, M. A.; Chunggaze, M.; Trindade, T.; Walsh, J. R.; Jones, A. C. *J. Cryst. Growth* **1997**, *170*, 23.
- 10 Smith, S. M.; Schlegel, H. B. *Chem. Mater.* **2003**, *15*, 162.
- 11 The correct positions (in 2θ) for the peaks are: 31.8° (100), 34.5° (002), 36.3° (101), 47.5° (102), 56.6° (110), and 62.9° for the (103) diffraction line. Calculated using the ICSD database <http://www.cmbi.kun.nl/icsd> Albertsson, J.; Abrahams, S. C.; Kvik, A. *Acta Cryst. B.* **1983**, *45*, 34.
- 12 $D = 0.9\lambda/(\beta\cos\theta)$, $\lambda = 1.54 \text{ \AA}$, $\beta = \text{FWHM}$ (in radians), $\theta = \text{diffraction angle}$, the diameter is averaged on all diffraction peaks.
- 13 Bulle-Lieuwma, C. W. T.; Van Gennip, W. J. H.; Van Duren, J. K. J.; Honkheijm, P.; Janssen, R. A. J.; Niemantsverdriet, J. W. *Appl. Surf. Sci.* **2003**, *203-204*, 547.
- 14 The intensity was determined by comparing the measured J_{SC} with the J_{SC} at 1 sun intensity, which was obtained from the convolution of the spectral response with the solar AM1.5 spectrum.
- 15 The fluctuations in the current are most likely due to fluctuations in the light source intensity.
- 16 This work has been performed in collaboration with Dr. Lenneke H. Slooff at ECN Solar Energy, Petten, The Netherlands. Studies on the effect of the relative humidity on the photovoltaic response have been performed in a controlled atmosphere.
- 17 Work performed at ECN was on MDMO-PPV made by TNO Industry Eindhoven, synthesis as described in : Louwet, F.; Vanderzande, D.; Gelan, J.; Mullens, J. *Macromolecules* **1995**, *28*, 1330.
- 18 These solutions all contain THF and toluene from the stock precursor solution, as mentioned in the experimental section.
- 19 Martens, H. C. F.; Blom, P. W. M.; Schoo, H. F. M., *Phys. Rev. B.* **2000**, *61*, 7489.
- 20 Initial experiments led to rough surfaces, and annealing in air increased the roughness, only very moderate photovoltaic effects were observed.

Samenvatting

Duurzame bronnen voor energie zijn nodig om nu en in de toekomst te kunnen voldoen aan de toenemende vraag naar energie. Zonne-energie is een vorm van duurzame energie mits duurzame materialen voor de constructie van zonnecellen worden gebruikt. De huidige generatie zonnecellen wordt gemaakt van silicium. Dit materiaal is volop beschikbaar, maar het maken van perfect kristallijn silicium is gezien de hoge energetische kosten verre van duurzaam. Alternatieven zoals semi-kristallijn en amorf silicium leveren energie tegen enigszins gereduceerde kosten.

De constructie van zonnecellen uit goedkope en gemakkelijk te verwerken materialen lijkt de toekomst te hebben. Polymeren zijn relatief gemakkelijk te maken, zijn lichtgewicht en goed te verwerken. Halfgeleidende geconjugeerde polymeren hebben de eigenschap dat ze licht absorberen en ladingen kunnen transporteren, en zijn dan ook veelbelovende materialen voor toepassing in zonnecellen. Helaas zijn de rendementen van zonnecellen op basis van polymeren nog te laag om er op grote schaal economisch rendabele toepassingen van te kunnen maken.

Zonnecellen die een serieus alternatief voor de silicium cellen vormen zijn de zogenaamde kleurstof zonnecellen. Een kleurstof monolaag op een ruw titaan dioxide (TiO_2) elektrode absorbeert het zonlicht en het titaan dioxide zorgt voor het transport van elektronen. De elektrolyt dat dient voor het transport van gaten zorgt echter voor problemen, vervanging daarvan is dan ook nodig om te komen tot stabiele zonnecellen. Het is in theorie goed mogelijk om zowel de elektrolyt als de kleurstof te vervangen door een halfgeleidend polymeer.

Dit proefschrift heeft als doel alternatieven voor silicium zonnecellen te onderzoeken en daarbij gebruik te maken van hybride materialen die een combinatie zijn van anorganische halfgeleiders en halfgeleidende polymeren. De voordelen van de kleurstof zonnecel, o.a. het effectieve transport van elektronen door de anorganische halfgeleider, kunnen op deze manier gecombineerd worden met de gemakkelijke verwerkbaarheid van polymeren.

De interactie tussen TiO_2 nanodeeltjes en geconjugeerde oligomeren is onderzocht in hoofdstuk 2. Deze oligomeren dienen als een modelsysteem voor de halfgeleidende polymeren die in combinatie met halfgeleidende anorganische materialen zoals TiO_2 gebruikt kunnen worden in zonnecellen. TiO_2 nanodeeltjes worden oplosbaar gemaakt worden door hun oppervlak te bedekken met zeepachtige moleculen. Heterosupermoleculen (moleculaire hybride materialen) kunnen worden gemaakt door in oplossing deze TiO_2 nanodeeltjes en de oligomeren aan elkaar te binden. Na foto-excitatie van het oligomeer vindt elektronoverdracht plaats naar het TiO_2 nanodeeltje, vergelijkbaar met het proces dat plaatsvindt in een werkende zonnecel. Door gebruik te maken van verzadigde $(\text{CH}_2)_n$ bruggen zijn de

oligomeren op verschillende afstanden van het oppervlak van het nanodeeltje te plaatsen. Op deze manier kan de relatie tussen de snelheid van elektronoverdracht en de te overbruggen afstand bestudeerd worden.

ZnO nanodeeltjes van ongeveer 5 nm in diameter, die oplosbaar zijn in organische oplosmiddelen, kunnen eenvoudig worden gemaakt via een nat chemische procedure (hoofdstuk 3). Bij deze nanodeeltjes is het niet nodig het oppervlak te modificeren om oplosbaarheid in organische oplosmiddelen te verkrijgen. Het blijkt mogelijk om op een fotofysische en elektrische manier deze nanodeeltjes met elektronen te laden. Met technieken zoals fotogeïnduceerde absorptie spectroscopie, fluorescentie en infrarood spectroscopie wordt aangetoond dat het elektron in de geleidingsband van het ZnO nanodeeltje een lange levensduur heeft, maar door toediening van zuurstof kan worden verwijderd.

Mengsels van deze nanodeeltjes en geconjugeerde polymeren worden gebruikt als de actieve laag in een zonnecel (hoofdstuk 4). Zonnecellen op basis van ZnO nanodeeltjes (*nc-ZnO*) en het geconjugeerde polymeer poly[2-methoxy-5-(3',7'-dimethyloctyloxy)-1,4-phenylenevinylene] (MDMO-PPV) werken optimaal als de hoeveelheid ZnO tussen de 26 en 35 volumepercent ligt en de dikte van de actieve laag ongeveer 100 nm is. Een geoptimaliseerde cel heeft een geschat rendement van 1.6%. Dit is ongeveer even hoog als het rendement van de tot nu toe beste zonnecel op basis van CdSe en geconjugeerde polymeren. De hoge externe kwantumefficiëntie van deze cellen onder monochromatische belichting, toont aan dat als er licht met een golflengte van 520 nm opvalt, 40% van de opvallende fotonen leidt tot elektrische stroom. Aangezien bij die golflengte ongeveer 80% van de fotonen in de zonnecel geabsorbeerd wordt, geeft dit aan dat 50% van de ladingen verloren gaan gedurende het hele proces vanaf de vorming van het exciton tot de collectie van elektronen en gaten aan de elektrodes. De hoge mobiliteiten die in het vooruitzicht gesteld werden door de veelbelovende mobiliteiten gemeten in bulk ZnO, zijn niet waar te nemen in de *nc-ZnO*:polymeer mengsels. In tegenstelling tot wat geldt voor bulk kristallijn materiaal, is voor een efficiënt transport van elektronen in deze mengsels een sprongsgewijs transport tussen nanodeeltjes nodig, dit vertraagt het transport van elektronen. De gevonden nul-veld elektronmobiliteit van $\sim 8 \times 10^{-10} \text{ m}^2 \text{ V}^{-1} \text{ s}^{-1}$ is maar een factor 10 hoger dan de gaten mobiliteit van puur MDMO-PPV.

In hoofdstuk 5 worden de fotofysische en optische eigenschappen van de mengsels gecombineerd met de AFM (atomic force microscopy) en TEM (transmissie elektronenmicroscopie) studies naar de morfologie, en gebruikt om meer inzicht te krijgen in de werking van deze zonnecellen. Fotoluminescentie experimenten tonen aan dat een deel van de MDMO-PPV fasegescheiden is van de *nc-ZnO*. Enkele MDMO-PPV domeinen zijn zo groot dat een deel van de excitonen niet meer binnen hun levensduur naar een ZnO nanodeeltje kunnen diffunderen en ca. 15% van de geabsorbeerde fotonen leidt niet tot ladingsscheiding. Op basis van de TEM waarnemingen kunnen we concluderen dat de ZnO nanodeeltjes en de MDMO-PPV redelijk homogeen mengen. Zoals verwacht op basis van

de fotoluminescentie experimenten kunnen ook kleine pure MDMO-PPV domeinen worden waargenomen: er is sprake van fasescheiding op nano-schaal. AFM experimenten aan *nc*-ZnO:MDMO-PPV mengsels laten deze fasescheiding niet duidelijk zien. Aan het oppervlak van de film valt wel een dunne laag puur MDMO-PPV waar te nemen. Bij lage concentraties *nc*-ZnO in de mengsels lijkt onder deze oppervlaktelaag een redelijk homogene blend van *nc*-ZnO en MDMO-PPV te zitten. Na verhoging van de *nc*-ZnO concentratie is de vorming van sferische structuren waar te nemen. Bij een verdere verhoging van de *nc*-ZnO concentratie nemen deze structuren in grootte toe en verruwt het oppervlak van de film. Door de combinatie van deze verschillende technieken is een beeld te vormen van de werking van de zonnecel en de relatie tot de hoeveelheid *nc*-ZnO in de zonnecel.

In hoofdstuk 4 is aangetoond dat de combinatie van ZnO en geconjugeerde polymeren succesvol is in hybride polymere zonnecellen. Het maken van goed gedefinieerd kristallijn ZnO bij lage temperaturen is mogelijk en om die reden wordt in hoofdstuk 6 gekeken naar de vorming van kristallijn ZnO in de polymeer film, uitgaande van een ZnO precursor. Het beoogde effect is een betere menging van de materialen, dan die tussen geconjugeerde polymeren en van tevoren gemaakte anorganische nanodeeltjes. De precursor voor ZnO wordt daartoe toegevoegd aan een oplossing van MDMO-PPV in chloorbenzeen. Na spin coaten van deze oplossing wordt een strakke film gevormd. Kristallijn ZnO ontstaat na verwarmen van de verkregen film op 110 °C. Dit simpele proces levert redelijk efficiënte zonnecellen op met een rendement van ongeveer 1%. Dit rendement is een verbetering met een factor 5 t.o.v. de beste cellen gemaakt vanuit een TiO₂ precursor. De morfologie van deze cellen is bestudeerd als functie van de hoeveelheid ZnO en de luchtvochtigheid tijdens het spin coaten. De luchtvochtigheid blijkt een grote rol te spelen, er is een duidelijk effect waarneembaar op de werking van de zonnecel en op de morfologie van de films.

Zonnecellen op basis van hybride materialen zijn veelbelovend. Een breed scala aan anorganische materialen is al toegepast, voorbeelden zijn: CdSe, TiO₂, CuInS₂ en CuInSe₂. Dit proefschrift voegt ZnO als succesvol voorbeeld daar aan toe. De voordelen van ZnO zijn de non-toxiciteit en de lage temperatuur synthese van kristallijn materiaal. De nadelen zijn ook evident: ZnO zelf absorbeert geen zonlicht in tegenstelling tot bijvoorbeeld CdSe. Er valt nog veel te verbeteren aan de hybride zonnecellen. Die verbeteringen lijken vooral gezocht te moeten worden in het type polymeer en de structurering van de anorganische fase. Een hogere gaten en elektronen mobiliteit, maar bovenal een verbeterde overlap van de absorptie van het polymeer met het zonnenspectrum zullen nodig zijn om het rendement van dit type cellen te verhogen. De enorme vooruitgang die de laatste jaren wordt geboekt met hybride en volledig polymere zonnecellen geeft vertrouwen in hun toekomst.

Summary

To be able to satisfy the increasing demands for energy, it is necessary to use sustainable energy resources. Solar energy is a form of sustainable energy, provided that durable materials for the construction of solar cells are used. The current generation of solar cells is made of silicon. This material is available in abundance but given the high energetic costs of making perfectly crystalline silicon, this material is far from sustainable. Alternatives such as semi-crystalline and amorphous silicon provide energy against slightly reduced costs.

The construction of solar cells from materials that are cheap and easy to process seems promising for the future. Polymers are relatively easy to make, to process and are lightweight. Semiconducting conjugated polymers absorb light and transport charges, and therefore might be a promising material for application in solar cells. Unfortunately, the performance of solar cells based on polymeric materials is still too low for economically profitable large-scale applications.

Solar cells that constitute a realistic alternative for silicon based solar cells are the so-called dye sensitized solar cells. A monolayer of dye molecules on a high surface area titanium dioxide (TiO_2) electrode absorbs sunlight, and the titanium dioxide ensures the transport of electrons. The electrolyte that serves for the transport of holes however introduces serious problems, and replacement is necessary to reach stable solar cells. In theory, it is well possible to replace both the electrolyte and the dye with a conjugated polymer.

This thesis aims to explore alternatives for silicon solar cells, using hybrid materials, which are a combination of inorganic semiconductors and conjugated polymers. In this way, the advantages of the dye sensitized solar cell, e.g. the effective transport of electrons by the inorganic semiconductor, can be combined with the ease of processing of polymeric materials.

The interaction between TiO_2 nanoparticles and conjugated oligomers has been examined in chapter 2. These oligomers serve as a model system for the semiconducting polymers that, combined with semiconducting inorganic materials such as TiO_2 , can be used in solar cells. TiO_2 nanoparticles can be dissolved in organic solvents by surface modification with surfactants. TiO_2 nanoparticles and the oligomers are connected to each other, leading to the formation of soluble heterosupramolecules (a molecular hybrid material). After photoexcitation of the oligomer, electron transfer to the TiO_2 nanoparticle takes place, similar to the process that occurs in an operational solar cell. Using saturated $(\text{CH}_2)_n$ bridges the oligomers can be placed at a number of different distances from the surface of the nanoparticle. This allows investigating the relation between the speed of the electron transfer and the distance the electron has to bridge.

ZnO nanoparticles of approximately 5 nm in diameter are well soluble in organic solvents and are made using a facile wet chemical procedure (see chapter 3). These nanoparticles do not require a surface modification in order to obtain solubility in organic solvents. It is possible to charge these nanoparticles with electrons, either by electronic or photophysical electron injection. With techniques such as photoinduced absorption spectroscopy, fluorescence and infrared spectroscopy it is shown that this electron has a long lifetime, and is removed from the conduction band of the ZnO nanoparticle by exposure to oxygen.

Mixtures of these nanoparticles and conjugated polymers are used as the active layer in solar cells (chapter 4). Solar cells based on ZnO nanoparticles (*nc*-ZnO) and a conjugated polymer poly[2-methoxy-5-(3',7'-dimethyloctyloxy)-1,4-phenylenevinylene] (MDMO-PPV) show an optimal performance when the volume percent of ZnO is in between 26 and 35%, and the thickness of the active layer is approximately 100 nm. An optimized cell has a power efficiency of 1.6%. This efficiency is comparable to the so far best solar cells based on hybrid materials: a combination of CdSe and conjugated polymers. The high external quantum-efficiency of these solar cells under monochromatic illumination reveals that when illuminated at a wavelength of 520 nm, 40% of the incoming photons leads to charge separation. Since at that wavelength approximately 80% of the photons is absorbed in the solar cell, this indicates that the complete process starting with the creation of an exciton up to collection of the charges at the electrodes still allows the collection of 50% of the charges. The high mobilities that are expected based on the promising mobilities that have been measured in bulk ZnO, cannot be observed in the *nc*-ZnO:polymer mixtures. In contrast to bulk crystalline materials, electron transport between nanoparticles occurs via a slow hopping process. The found zero-field electron mobility of $\sim 8 \times 10^{-10} \text{ m}^2 \text{ V}^{-1} \text{ s}^{-1}$ is only a factor 10 higher than the hole mobility of pure MDMO-PPV.

In chapter 5 the photophysical and optical properties of the mixtures are combined with the atomic force microscopy (AFM) and transmission electron microscopy (TEM) experiments to study the morphology and to gain more insight in the performance of these solar cells. Photoluminescence experiments show that a part of the MDMO-PPV is phase-separated from the *nc*-ZnO. MDMO-PPV domains appear that are so large that, within their lifetime, a part of the excitons cannot reach an interface with a ZnO nanoparticle. TEM studies reveal that the ZnO nanoparticles and the MDMO-PPV are rather homogeneously mixed. As could be expected based on the photoluminescence experiments, phase separation on a nano-scale occurs because with TEM small, pure MDMO-PPV domains are observed. AFM experiments performed on *nc*-ZnO:MDMO-PPV blends do not clearly show this phase separation. At the surface of the blend a thin film of pure MDMO-PPV can be observed. When the concentration of *nc*-ZnO in the blend is low, a rather homogeneous blend of MDMO-PPV and *nc*-ZnO can be observed just below this surface layer. Spherical structures appear when the ZnO nanoparticle concentration is increased. After a further increase of the *nc*-ZnO

concentration these spherical structures increase in size and the surface-roughness of the film increases. Using this combination of different techniques, insight in the performance of these solar cells and its relation to the amount of *nc*-ZnO in the blend has been obtained.

In previous chapters it has been shown that the combination of ZnO and conjugated polymers appears very successful for application in hybrid polymer solar cells. The synthesis of well-defined crystalline ZnO is possible at low temperatures. For this reason is the in-situ formation of crystalline ZnO inside the polymer film explored in chapter 6. The desired effect is a better mixing of the materials using a ZnO precursor to overcome the mixing problems often encountered with blends from pre-synthesized nanoparticles and conjugated polymers. The precursor for ZnO is added to a solution of MDMO-PPV in chlorobenzene. After spin coating of this solution a smooth film is obtained. In a second step, crystalline ZnO is formed after heat treatment of the film at 110 °C. This simple process produces fairly efficient solar cells with a power conversion efficiency of approximately 1%. This efficiency is an improvement by a factor 5 with respect to the best efficiencies obtained from blends made from a TiO₂ precursor. The morphology of these cells has been studied as a function of the amount of ZnO and relative humidity of the surrounding atmosphere during spin coating. The humidity appears to have a huge impact, a clear effect can be observed on the performance of the solar cell and the morphology of the blends.

Solar cells that have been constructed from hybrid materials are very promising. A broad collection of inorganic materials have already been applied, e.g.: CdSe, TiO₂, CuInS₂, and CuInSe₂. This thesis adds ZnO as a successful example to that list. The advantages of ZnO are: the non-toxicity, and the facile low temperature synthesis of crystalline materials. The disadvantages are also obvious: ZnO does not absorb sunlight in contrast to for example CdSe. Hybrid polymer solar cells can be improved further, but many of those improvements should involve the conjugated polymer and the morphology of the inorganic phase. Higher hole and electron mobilities, but above all, an improved overlap of the absorbance of the polymer with the solar emission spectrum will be necessary to increase the efficiency of this type of solar cells. The enormous progress, which has been achieved the last years with hybrid and full-polymer solar cells, gives reasons to believe their future is bright.

Curriculum Vitae

Waldo Beek werd geboren op 11 juli 1977 te Roermond. Na het doorlopen van het VWO aan het Bisschoppelijk College Broekhin in Roermond begon hij in 1995 aan de studie Scheikundige Technologie aan de Technische Universiteit Eindhoven. Het propaedeutisch diploma werd in 1996 behaald. Zijn afstudeeronderwerp werd uitgevoerd in de capaciteitsgroep Anorganische Chemie en Katalyse onder begeleiding van prof. dr. J.W. Niemantsverdriet. Het afsluitend diploma werd in 2000 cum laude behaald. Vanaf oktober 2000



tot oktober 2004 werkte hij in dienst van de Nederlandse Organisatie voor Wetenschappelijk Onderzoek aan zijn promotie onderzoek onder begeleiding van prof. dr. ir. René Janssen in de capaciteitsgroep Macromoleculaire en Organische Chemie. De resultaten van dat promotie onderzoek staan beschreven in dit proefschrift.

Waldo Beek was born in Roermond (The Netherlands) at the 11th of July 1977. After finishing in 1995 his pre-university education at the 'Bisschoppelijk College Broekhin' in Roermond, he went to the Eindhoven University of Technology to start his study in Chemical Engineering. In 2000 he graduated cum laude with a major in Inorganic Chemistry and Catalysis (prof. dr. J.W. Niemantsverdriet). From October 2000 till October 2004 he was employed as a PhD-student by the Netherlands Organization for Scientific Research. He worked under guidance of prof. dr. ir. René Janssen in the Laboratory of Macromolecular and Organic Chemistry, and the results of his PhD-research are described in this thesis.

List of Publications

“Hybrid Solar Cells using a Zinc Oxide Precursor and a Conjugated Polymer”

Waldo J.E. Beek; Lenneke H. Slooff; Martijn M. Wienk; Jan M. Kroon; René A.J. Janssen

Adv. Mater. Submitted

“Spacer Length Dependence of Photoinduced Electron Transfer in Heterosupramolecular Assemblies of TiO₂ Nanoparticles and Terthiophene”

Waldo J.E. Beek; René A.J. Janssen

J. Mater. Chem. **2004**, *14*, 2795.

“Efficient Hybrid Solar Cells from Zinc Oxide Nanoparticles and a Conjugated Polymer”

Waldo J.E. Beek; Martijn M. Wienk; René A.J. Janssen

Adv. Mater. **2004**, *16*, 1009.

“Photoinduced Electron Transfer in Heterosupramolecular Assemblies of TiO₂ Nanoparticles and Terthiophene Carboxylic Acid in Apolar Solvents”

Waldo J.E. Beek; René A. J. Janssen

Adv. Funct. Mater. **2002**, *12*, 519.

Dankwoord

Zo op het eind van het proefschrift is het de hoogste tijd de mensen te bedanken die mij de afgelopen jaren geholpen hebben. Mijn eerste promotor René Janssen, wil ik graag bedanken voor de begeleiding tijdens mijn promotie. René, je laat je promovendi de ruimte die ze nodig hebben om zichzelf te ontwikkelen en hun eigen plannen uit te voeren, dat heb ik als zeer prettig ervaren. Bert Meijer wil ik graag bedanken voor het deelnemen in mijn leescommissie, maar toch vooral voor het mogelijk maken dat ik kon werken binnen SMO. Zonder twijfel is SMO mede dankzij jou een groep waar mensen graag en goed hun werk doen. Professor Michael McGehee, I hope you enjoy your short stay in The Netherlands and I really appreciate you are willing to serve as my second promotor. Professor Paul Blom wil ik ook bedanken voor zijn deelname aan de leescommissie. Paul, ik wil je daarnaast bedanken voor het commentaar op mijn proefschrift en ik ben blij dat Jan Anton Koster, binnen jouw groep nu het werk aan mobiliteitsmetingen aan ‘mijn’ zonnecellen over heeft genomen.

Martijn Wienk wil ik bedanken voor zijn zeer grote betrokkenheid bij mijn onderzoek, voor vragen, opmerkingen en het afreageren van frustraties kon ik altijd bij hem terecht. Martijn, je zult me wel moeilijk geloven, maar je werkt wel degelijk stimulerend ondanks je (vaak terechte) ‘ja maar’ opmerkingen.

Jeroen van Duren heeft door zijn promotieonderzoek eraan bij gedragen dat het maken en karakteriseren van zonnecellen niet opnieuw door mij uitgevonden hoefde te worden, waarvoor mijn dank. Van de ‘René club’ wil ik Stefan Meskers, Edwin Beckers, Paul van Hal en Ton Offermans bedanken voor hun bijdragen, hulp en discussies. Discussies en goede adviezen waren er ook volop tijdens de ‘René groep lunches’. Ik wil ook graag Martijn Kemerink bedanken voor zijn hulp met en uitleg over AFM.

Maarten Smulders, jij was de enige student die ik heb kunnen ‘strikken’ voor een stage plaats. We hebben een tijd leuk samengewerkt aan verrassend slecht-reproduceerbare zonnecellen op basis van ZnO en polythiofeen. Ik heb in die periode veel geleerd en ik hoop jij ook, veel succes verder in je studie en daarna.

Een leuk onderdeel van promoveren is het samenwerken met andere groepen. Ik maakte dan wel formeel geen deel uit van het DPI maar toch zijn er leuke gezamenlijke projecten uit voortgekomen. Tom Savenije en Pieter Quist van het IRI in Delft wil ik bedanken voor de TRMC metingen. Reproduceerbaarheid was ook hier weer het toverwoord, maar ik geloof dat we stukje bij beetje toch meer te weten zijn gekomen over de ZnO polymeer mengsels. Er is een tijd geweest dat ik per se een AM1.5 meting wilde doen aan mijn (beste) zonnecellen. Daarvoor heb ik enkele uitstapjes naar ECN

mogen maken. De metingen waren keer op keer geen succes, maar de daaropvolgende avonden in Amsterdam met Sjoerd Veenstra en Wil Jan Verhees waren dat wel. In het laatste jaar van mijn promotie heb ik samen met Lenneke Slooff van ECN gewerkt aan cellen op basis van het in-situ concept zoals in hoofdstuk 6 staat beschreven. Deze samenwerking heb ik als zeer prettig en succesvol ervaren. I would like to thank Xiaoni Yang for our TEM experiments; it is pleasant to work with someone who really knows how to operate the TEM and shoots better pictures than I can. Er bestond geen officiële samenwerking met TNO, toch waren er tijden dat ik er de (draai)deur plat liep. Gelukkig kon ik via Marc Koetse steeds binnenkomen om filmdiktes te meten en even te babbelen.

Een aantal mensen op de faculteit heeft mij met diverse technieken bijgestaan. Ik wil dan ook Tiny Verhoeven en Peter Thüne bedanken voor hun hulp met XPS. Marco Hendrix wil ik bedanken voor de XRD metingen. Sacha Kodentsov, Joachim Loos en Dick Klepper wil ik graag bedanken voor hun hulp en uitleg bij de TEM.

De capaciteitsgroep SMO-M2N draait mede dankzij de hulp van de secretaresses Ingrid Dirx, Joke Rediker, Carine van der Vaart en Hanneke Veldhoen. Ook wil ik Hans Damen bedanken voor zijn hulp met de chemicaliën en zijn technische assistentie. SMO zonder vlaai of een borrel geregeld door Henk Eding zou ondenkbaar zijn.

Mijn kamer heb ik in die jaren gedeeld met John van Haare, Jeroen van Duren en tijdens mijn schrijfperiode alleen met Bea Langeveld en Frank Verbakel. Bea, je zult wel eens nachtmerries hebben gehad door mijn irritante vragen over correct Engels. Ik deed het puur om je terug te pakken voor alle telefoontjes die ik voor jou aan mocht nemen. Frank, jouw vragen waren een zeer welkome afleiding van het schrijfwerk, zeker tijdens de laatste hoofdstukken.

Naast werk en studie heeft het schermen me veel plezier gebracht, vooral de niet sport gerelateerde activiteiten van Hoc Habet zullen me nog lang bijblijven. Jaap, jou wil ik graag bedanken voor je vriendschap de afgelopen jaren en ik wens je veel succes bij Océ. Harm, de titel Mr. Hoc Habet heb jij zeker al verdiend, ik hoop dat jij binnenkort ook Dr. voor je naam kunt zetten.

Ik wil mijn ouders en mijn broer bedanken voor hun steun en het begrip, ik ben te weinig thuis geweest het afgelopen jaar. Mijn plannen voorspellen echter dat ik dat niet echt goed zal gaan maken in het komende jaar.

Laat ik eindigen met te zeggen dat ik een het mooie tijd heb gevonden en daarvoor iedereen wil bedanken die ik de afgelopen jaren ben tegen gekomen tijdens studie, promotie en privé, op naar andere mooie tijden.